Selected Projects in Gas-Phase Spectroscopy

by

Pina Colarusso

A thesis

presented to the University of Waterloo

in fulfilment of the

thesis requirement for the degree of

Doctor of Philosophy

in

Chemistry

Waterloo, Ontario, Canada, 1997

The University of Waterloo requires the signatures of all persons using or photocopying this thesis. Please sign below, and give address and date.

Abstract

Three projects have been carried out in the area of gas-phase spectroscopy:

i. The infrared emission spectra of the transient molecules HBO and DBO have been obtained with a Fourier transform spectrometer. The rotational-vibrational transitions were recorded at a resolution of 0.01 cm^{-1} over the wavenumber range between 350 and 4000 cm^{-1}. The line positions have been measured and analyzed.

ii. The infrared spectra of gas-phase uracil, thymine, and adenine have been recorded from 100 to 3700 cm^{-1} at a resolution of 1 cm^{-1}. The vibrational band positions and qualitative band intensities are reported and compared to published matrix data and to theoretical calculations. The work suggests that gas-phase emission spectroscopy is a sensitive technique for recording the spectra of organic and biological molecules.

iii. The ionization potentials of neutral osmium and iridium atoms have been obtained by mass-analyzed optical-optical double resonance spectroscopy. Observation of the photoionization thresholds have yielded approximate values of 68058±2 cm^{-1} for Os I and 72324±2 cm^{-1} for Ir I. In addition, high-lying ns and nd Rydberg series have been recorded and fit to a standard expression in order to obtain independent estimates of the ionization potentials. The results are 68058.9±1.6 cm^{-1} for Os I and 72323.9±1.8 cm^{-1} for Ir I.

Acknowledgements

I would like to thank my supervisor, Peter Bernath, for his support and encouragement as well as for his uncanny knack for directing me toward the appropriate references. I have also appreciated the input from the members of my advisory committee at various stages of my time here at Waterloo.

I am grateful to Benoit Simard of the National Research Council of Canada, for providing me with the opportunity to carry out the work described in the the last chapter of this thesis. Marie-Ange Lebeault-Dorget shared her invaluable expertise for the experimental aspects of the project. I would also like to acknowledge Yoshi Kawashima, who has been collaborating with me on the DBO project.

A special note goes to Alexandrina Muntianu, Keqing Zhang, and Zulfikar Morbi, who started off as my co-workers, but who have ended up as my friends. In particular, I will not forget Jeff Waller, whose memory will always remind me that we are descended from the stars.

I am indebted to Chris Mathers, whose initial help and encouragement gave me the confidence to tame the assorted hardware and software creatures in our laboratory menagerie. The last few years would have been much duller without Denise Lacombe, whose good humor and equanimity have enriched my stint in the basement.

It means a great deal to me to acknowledge my high school chemistry teacher, Mrs. Roberta Wood, who encouraged my first putterings in the laboratory.

I would thank my parents, Maria and Luigi, and my sister and brother, Marisa and Robert, for their support over my (endless) years of study. My mother, with her endless curiosity and perseverance, has been a wonderful role model.

My last words of thanks I save for my husband, David, for his love and understanding, and for always believing that this thesis would be written. It is to him that I dedicate this work.

To David

Contents

List of Figures

List of Tables

Introduction

Spectroscopy is the study of the interaction between light and matter at the atomic and molecular levels. It is a window into diverse phenomena, ranging from the mediation of the light response in the human eye to the formation of the northern lights in the upper atmosphere. No matter what the question, however, spectroscopic queries share a common goal: to first measure light, and then to interpret the pattern that appears.

This thesis describes three projects in gas-phase spectroscopy. Although the projects address different questions, the underlying goal was to characterize the energetics of free atoms and molecules. The gas-phase is ideal for such investigations because the interactions between neighboring species are minimized. The results obtained from spectroscopic studies of isolated atoms and molecules not only provide information about fundamental chemical properties, but also may serve as a reference point when examining these species in more complex systems.

The first part of this thesis focuses on two studies in molecular vibrational-rotational spectroscopy. An example of a vibrational spectrum of a molecule is given in Fig. 0.1. The spectrum is the record of infrared photons that were emitted by a molecule as it formed at temperatures in excess of 1400°C. A double-lobed structure is evident which upon closer examination reveals numerous fine lines. This dissertation describes how molecular motion can give rise to such a beautiful pattern. To provide a framework for the interpretation of the experimental results, Chapter 1 presents an overview of vibrational-rotational spectroscopy. The next chapter outlines some of the main aspects of Fourier transform spectroscopy and its
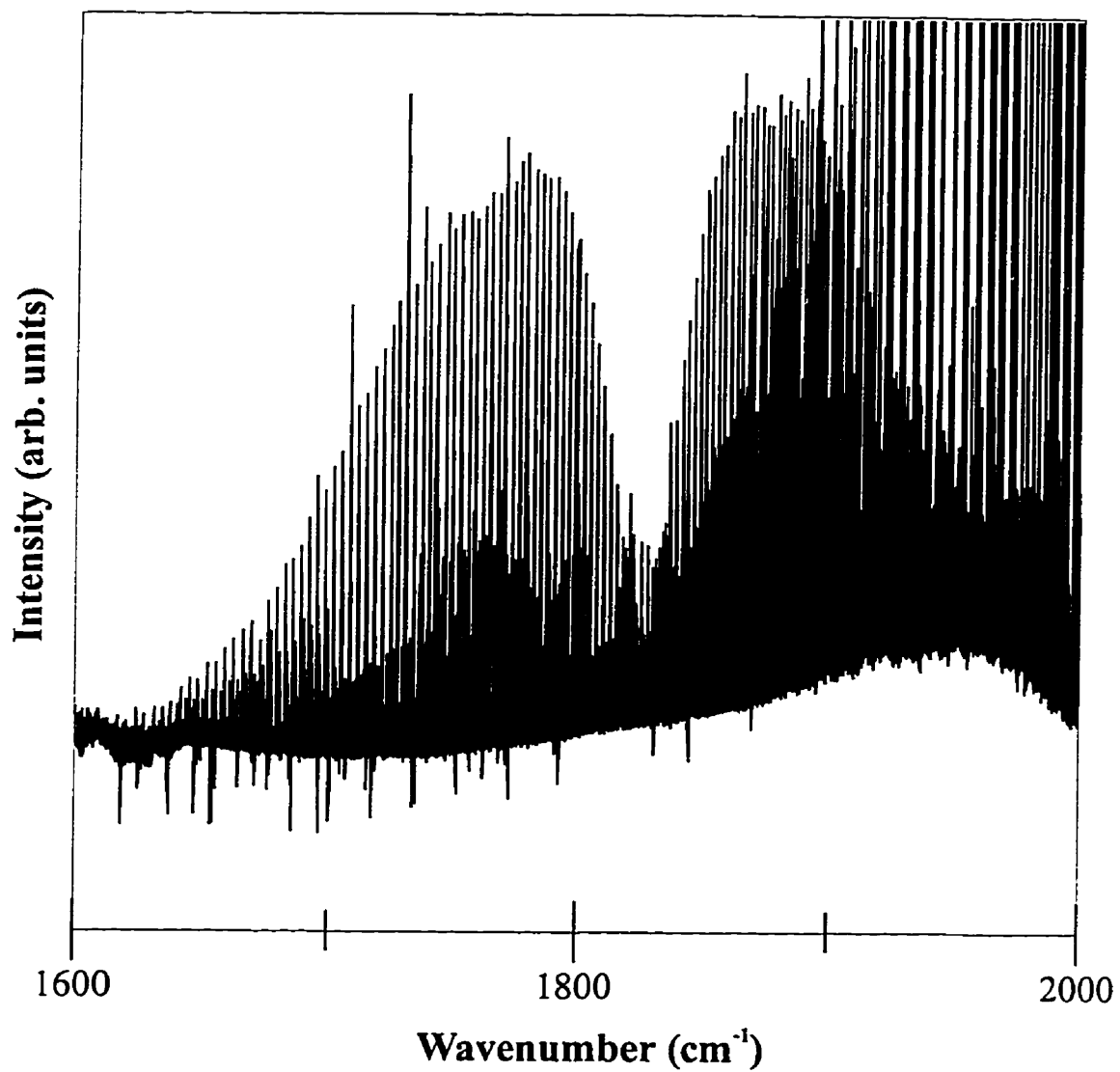
Figure 0.1: A molecular infrared spectrum.

application to the infrared region. The introductory material is followed by a summary of two different investigations in the area of Fourier transform infrared emission spectroscopy. Chapter 4 reports on a detailed analysis of the high-resolution infrared spectra of the transient molecules HBO and DBO. The results are applied toward a better elucidation of the vibrational-rotational motion of both species. The next project, outlined in Chapter 4, explores the feasibility and relevance of gas-phase infrared spectroscopy to the nucleic acid bases, a class of biological molecules.

From the study of molecular motion, the discussion then proceeds to the investigation of atomic ionization potentials. Most first ionization potentials are known to a high degree of accuracy; osmium and iridium, however, were the only two stable atoms without reliable values. Chapter 5 describes the application of mass-analyzed threshold ionization, a technique that combines elements of laser and mass spectroscopy, to the determination of these fundamental physical quantities for both osmium and iridium.

Chapter 1

Molecular Vibration and Rotation

1.1 Overview

Molecular spectroscopy is built on a solid theoretical framework that draws upon both classical and quantum physics. Classical mechanics provides useful models that form the basis for a number of spectroscopic approaches. One example is the normal coordinate; this important concept in vibrational spectroscopy arises from the classical treatment of small oscillations [1,2], as outlined in Section 1.2. Classical mechanics, of course, fails to address the essence of molecular spectroscopy: the quantized nature of molecular motion. Nonetheless, classical techniques often are the springboard to the more rigorous quantum mechanical treatments. As described in Section 1.3, the classical Hamiltonian for molecular motion can be transformed to an operator formalism [1,3,4]. The complicated quantum mechanical expression that results can be greatly simplified through several approximations. The approximate treatment leads to a reasonable interpretation of molecular vibration

and rotation, but the picture must be corrected for higher-order effects that are observed in molecular spectra.

1.2 Classical Treatment of Vibration

The normal coordinate is a central idea in vibrational spectroscopy that is based on the classical theory of small oscillations [1, 2, 5]. In this approach, the molecule is treated as a set of coupled harmonic oscillators that undergo small displacements about their equilibrium positions. The classical Lagrangian is written,

$$\mathcal{L} = T - V, \tag{1.1}$$

where T and V represent the kinetic and potential energies, respectively. The kinetic energy T for molecule that contains N atoms is:

$$T = \frac{1}{2}\sum_{i=1}^{N} m_i \left[\left(\frac{d\Delta x_i}{dt}\right)^2 + \left(\frac{d\Delta y_i}{dt}\right)^2 + \left(\frac{d\Delta z_i}{dt}\right)^2 \right], \tag{1.2}$$

where the m_i are the masses and $\Delta x, \Delta y, \Delta z$ are the displacements of the atoms from equilibrium. It is possible to introduce mass weighted Cartesian displacement coordinates given by

$$
\begin{aligned}
q_{1i} &= \sqrt{m_i}\Delta x_i, \\
q_{2i} &= \sqrt{m_i}\Delta y_i, \\
q_{3i} &= \sqrt{m_i}\Delta z_i,
\end{aligned}
\tag{1.3}
$$

such that the kinetic energy simplifies to

$$T = \frac{1}{2} \sum_{i=1}^{3N} \dot{q}_i^2. \tag{1.4}$$

For the ground electronic state, the potential energy V may be expressed as a power series in the displacements from equilibrium:

$$V = V_e + \sum_{i=1}^{3N} \left(\frac{\partial V}{\partial q_i} \right)_e \cdot q_i + \frac{1}{2} \sum_{i,j=1}^{3N} \left(\frac{\partial^2 V}{\partial q_i \partial q_j} \right)_e \cdot q_i q_j + \ldots \tag{1.5}$$

To simplify the expression, the energy of the equilibrium configuration V_e is set to zero, which also eliminates the first derivative because the energy is minimized at equilibrium. All terms beyond the quadratic are assumed to be negligible. Eq. (1.5) then reduces to:

$$\begin{aligned} V &= \frac{1}{2} \sum_{i,j=1}^{3N} \left(\frac{\partial^2 V}{\partial q_i \partial q_j} \right)_e \cdot q_i q_j \\ &= \frac{1}{2} \sum_{i,j=1}^{3N} f_{ij} \cdot q_i q_j \end{aligned} \tag{1.6}$$

where each second order partial derivative has been associated with a quantity f_{ij}, known as a force constant.

In the next step, the classical Lagrangian is used to solve the equations of motion for each atom:

$$\frac{d}{dt} \left(\frac{\partial T}{\partial \dot{q}_j} \right) + \left(\frac{\partial V}{\partial q_j} \right) = 0, \tag{1.7}$$

which leads to $3N$ simultaneous differential equations,

$$\ddot{q}_j + \sum_{i=1}^{3N} f_{ij} q_i = 0 \qquad j = 1, 2, \ldots 3N. \tag{1.8}$$

These equations are the classical equations of motion for coupled harmonic oscillators, and have a general solution:

$$q_i = A_i \cos(\sqrt{\lambda} t + \phi), \tag{1.9}$$

where A_i, $\sqrt{\lambda}$, and ϕ are constants. Substitution of the solutions into Eq. (1.8) yields $3N$ algebraic equations in the unknown amplitudes A_i,

$$\sum_{i=1}^{3N} (f_{ij} - \delta_{ij}\lambda) A_i = 0 \qquad j = 1, 2, \ldots 3N. \tag{1.10}$$

The non-trivial solutions λ for Eq. (1.10) are found by solving the eigenvalue equation:

$$\mathbf{FL} = \mathbf{L\Lambda}. \tag{1.11}$$

$\mathbf{F}$ is the symmetric matrix composed of the force constants f_{ij} given by:

$$\begin{pmatrix} f_{11} & f_{12} & f_{13} & \cdots & f_{1,3N} \\ f_{21} & f_{22} & f_{23} & \cdots & f_{2,3N} \\ \vdots & \vdots & \vdots & \ddots & \vdots \\ f_{3N,1} & f_{3N,2} & f_{3N,3} & \cdots & f_{3N,3N} \end{pmatrix}, \tag{1.12}$$

and Λ is the diagonal matrix containing the roots, λ. The columns in $\mathbf{L}$ are the

eigenvectors associated with the elements λ in the diagonal matrix Λ. Eq. (1.9) reveals that the q_i associated with each root λ correspond to a set of atomic motions about the equilibrium positions described by the amplitudes A_{ij}, frequency $\frac{\sqrt{\lambda}}{2\pi}$, and phase ϕ. The set of motions associated with each λ is designated a normal mode of vibration Q_k [1, 2, 5].

In general, the solutions of the set of $3N$ equations will lead to six zero roots for nonlinear molecules and five zero roots for linear molecules [1]. The zero roots are obtained for the translational and rotational motions of the molecule, which have no vibrational frequency. The remaining degrees of freedom, $3N$-6 for a nonlinear molecule, and $3N$-5 for a linear species, are the normal modes of vibration.

Since $\mathbf{L}$ is an orthogonal matrix,

$$\tilde{\mathbf{L}}\mathbf{F}\mathbf{L} = \tilde{\mathbf{L}}\mathbf{L}\Lambda = \Lambda. \tag{1.13}$$

The transpose $\tilde{\mathbf{L}}$ transforms the coordinates q_i into the normal modes Q_k via

$$\mathbf{Q} = \tilde{\mathbf{L}}\mathbf{q}. \tag{1.14}$$

The frequencies are obtained from the eigenvalues of the force constant matrix, and the normal modes from $\mathbf{L}$. Thus, the Q_k represent a new set of coordinates that represent the vibrational motion of molecules.

As a simple illustration, the bond stretches in a linear triatomic molecule will be considered [6]. The potential energy is derived within the valence bond approximation, in which only atoms connected by bonds are considered to exert forces on

each other [5–7]. The potential energy then can be expressed as:

$$V = \frac{1}{2} f_{12} \Delta r_{12}{}^2 + \frac{1}{2} f_{23} \Delta r_{23}{}^2 \tag{1.15}$$

where f_{ij} are the force constants and Δr_{ij} are the differences between the displacements, $\Delta x_j - \Delta x_i$. If the potential energy can be written in terms of the mass-weighted coordinates:

$$V = \frac{1}{2} k_1 \left(\frac{q_2}{\sqrt{m_2}} - \frac{q_1}{\sqrt{m_1}} \right)^2 + \frac{1}{2} k_2 \left(\frac{q_3}{\sqrt{m_3}} - \frac{q_2}{\sqrt{m_2}} \right)^2 , \tag{1.16}$$

then the force constant matrix is

$$\mathbf{F} = \begin{pmatrix} \frac{k_1}{m_1} & \frac{-k_1}{\sqrt{m_1 m_2}} & 0 \\ \frac{-k_1}{\sqrt{m_1 m_2}} & \frac{k_1 + k_2}{m_2} & \frac{-k_2}{\sqrt{m_2 m_3}} \\ 0 & \frac{-k_2}{\sqrt{m_2 m_3}} & \frac{k_2}{m_3} \end{pmatrix} . \tag{1.17}$$

For a centrosymmetric triatomic such as CO_2, the roots λ are:

$$\lambda_1 = \frac{k}{m_1}, \quad \lambda_2 = k \left(\frac{2m_1 + m_2}{m_1 m_2} \right), \quad \text{and} \quad \lambda_3 = 0. \tag{1.18}$$

The λ can be substituted in Eq. (1.10) to yield the following:

$$
\begin{array}{lll}
q_1 = -q_3, & q_2 = 0 & \text{for } \lambda_1 = \frac{k}{m_1} \\[2mm]
q_1 = q_3, & q_2 = -2\sqrt{\frac{m_1}{m_2}} q_1 & \text{for } \lambda_2 = k \left(\frac{2m_1 + m_2}{m_1 m_2} \right) \\[2mm]
q_1 = q_3, & q_2 = \sqrt{\frac{m_2}{m_1}} q_1 & \text{for } \lambda_3 = 0 .
\end{array}
\tag{1.19}
$$

The solutions are pictured in Fig. 1.1. For λ_3, the motion corresponds to a pure

translation, while the other two roots represent stretches. These diagrams, of course, are visualizations of the normal modes. A similar procedure can be used to obtain the modes for the bending motions of the molecule [5].

The treatment of molecular motion is greatly simplified by drawing on group theory. Only a few key ideas will be mentioned in this thesis; the chemical applications of group theory are numerous and have been discussed by several authors. One particularly useful (and painless) introduction is a book by Bishop [8]. Molecules may be classified into different point groups according to their symmetries. A point group contains the symmetry operations that leave the molecular geometry unchanged, and is described by a set of irreducible representations. Each of the irreducible representations is labelled by a symmetry species according to a convention developed by Mulliken [8]. In the treatment of molecular vibration, it can be shown that each normal mode corresponds to an irreducible representation of the molecular point group. The CO_2 molecule, as a centrosymmetric linear triatomic, belongs to the $D_{\infty h}$ point group. If the $D_{\infty h}$ operations are applied to the stretches, it is seen that Q_1 transforms as the symmetry species σ_g^+ while Q_2 transforms as σ_u^+. The remaining normal mode is a doubly degenerate bend that transforms as π_u. In the following sections, it will be seen that the labelling scheme is a powerful shorthand, though it may seem like a secret code if the underlying theory is ignored.

1.3   Quantum Mechanical Treatment

A quantum mechanical treatment of molecular vibration and rotation was developed by Wilson and Howard [1], with contributions from Darling and Dennison [9],
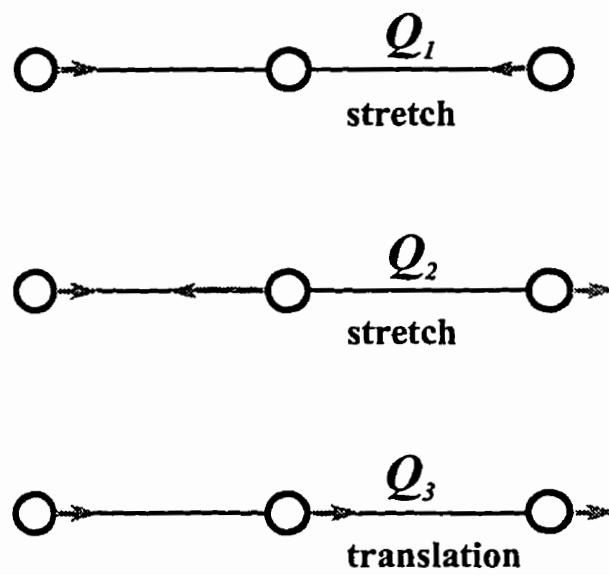
Figure 1.1: The relative displacements corresponding to two normal modes and one pure translation of CO_2 [6].

and later was reformulated elegantly by Watson [10]. All the treatments begin with the classical Hamiltonian for molecular motion, which is transformed to the quantum mechanical operator. The process is quite involved and the resulting Hamiltonian is a complicated expression that does not yield a general analytical solution. The reader is referred to the original papers for complete details. It can be shown, however, that a simple form of the Hamiltonian can be obtained by expressing the total wavefunction as a product of the wavefunctions associated with the various molecular degrees of freedom [3,4]. In many cases, analytical solutions of the simplified Hamiltonian exist, and these expressions form the basis for the interpretation of molecular vibrational-rotational spectra.

The first step toward a simplified Hamiltonian involves the Born-Oppenheimer approximation, which specifies that the total stationary wavefunction can be written as the product of electronic and nuclear wavefunctions [11]:

$$| t \rangle = | e \rangle \, | n \rangle. \qquad (1.20)$$

The justification for the separation of the nuclear and electronic motion is that the nuclei move much more slowly than the electrons, and thus only experience a potential field arising from the average motion of the electrons.

A further approximation can be introduced by considering the degrees of freedom associated with the nuclear wavefunction $| n \rangle$ independently [4]. In this picture, a molecule containing N nuclei possesses $3N$ degrees of freedom that are divided among translational, rotational, and vibrational motion. The molecular translation is described by three centre of mass coordinates X, Y, Z. Three angles

θ, ϕ, χ specify the rotation relative to the centre of mass unless the molecule is linear, when only two angles are required [11]. The remaining degrees of freedom, $3N$-6 for a nonlinear molecule, and $3N$-5 for a linear species, describe the vibrational motion. Thus, the nuclear wavefunction is treated as the product of the translational, vibrational, and rotational wavefunctions [11]:

$$| n \rangle = | t \rangle | v \rangle | r \rangle. \tag{1.21}$$

It then follows that the total molecular energy is given by

$$E_{total} = E_e + E_t + E_v + E_r. \tag{1.22}$$

The translational energy simply adds a constant to the total energy, and it will not be considered further [4].

For a non-linear molecule in the ground electronic state, it can be shown that the separation of the degrees of freedom reduces the Hamiltonian to the sum of the rotational and vibrational operators [4]:

$$
\begin{aligned}
\mathcal{H}_{vr}^0 &= \overbrace{\mathcal{H}_r^0}^{} \quad + \quad \overbrace{\mathcal{H}_v^0}^{} \\
&= \frac{1}{2} \left[\frac{\hat{\mathbf{J}}_x^2}{I_{xx}} + \frac{\hat{\mathbf{J}}_y^2}{I_{yy}} + \frac{\hat{\mathbf{J}}_z^2}{I_{zz}} \right] + \left[\frac{1}{2} \sum_{k=1}^{3N-6} \hat{\mathbf{P}}_k^2 + \hat{\mathbf{V}} \right],
\end{aligned} \tag{1.23}
$$

which is known as the rigid rotor, harmonic oscillator approximation. The $\hat{\mathbf{J}}_{x,y,z}$ are the operators associated with the components of rotational angular momenta along the molecule-fixed axes x, y, z, and the $I_{xx,yy,zz}$ are the principal moments

of inertia about x, y, z. The two remaining terms are the operators for the kinetic and the potential energy of vibration. The $\hat{\mathbf{P}}_k$ correspond to the vibrational linear momenta, and $\hat{\mathbf{V}}$ represents the harmonic oscillator potential.

For a linear molecule, however, the reasoning that leads to Eq. (1.23) is not appropriate because one of the moments of inertia is zero. Watson derived the correct Hamiltonian $\mathcal{H}_{vr}$ and showed that an isomorphic Hamiltonian exists such that [12]:

$$\mathcal{H}_{vr,iso} = \mathcal{U}\mathcal{H}_{vr}\mathcal{U}^{-1}, \tag{1.24}$$

where $\mathcal{U}$ is a unitary matrix. Note that $\mathcal{H}_{vr,iso}$ and $\mathcal{H}_{vr}$ share the same eigenvalues because they are related through a unitary transformation [4, 12]. In analogy to the non-linear case, it is possible to write an approximate Hamiltonian that is the sum of rotational and vibrational contributions [4]:

$$
\begin{aligned}
\mathcal{H}^0_{vr,iso} = \quad & \mathcal{H}^0_{r,iso} \quad + \quad \mathcal{H}^0_{v,iso} \\
= \quad & \overbrace{\left[\frac{\hat{\mathbf{J}}'^2_x + \hat{\mathbf{J}}'^2_y}{2I_{xx}}\right]} \quad + \quad \overbrace{\left[\frac{1}{2}\sum_{k=1}^{3N-5} \hat{\mathbf{P}}^2_k + \hat{\mathbf{V}}\right]},
\end{aligned}
\tag{1.25}
$$

where I_{xx} is the moment of inertia of the linear molecule.

The rigid rotor, harmonic oscillator Hamiltonian and its isomorphic counterpart for linear molecules are useful because they provide simple physical models for molecular motion. In most cases, the solutions of the eigenvalue equations for these Hamiltonians yield closed-form analytical expressions that can be used to predict the appearance of vibrational-rotational spectra in the ground electronic state. To obtain a more accurate model, first order correction operators are defined

that account for interactions omitted from the idealized picture of molecular motion. Indeed, these simplified Hamiltonians lie at the heart of more sophisticated treatments in which the eigenfunctions and eigenvalues are used as the basis for perturbative or variational calculations [1,3,4]. Ref. [4] provides a thorough discussion of vibrational-rotational Hamiltonians and their application to spectroscopy.

1.3.1 Rotation

The determination of the rotational energies begins with the fundamental commutation relations of the angular momentum [13],

$$[\hat{\mathbf{J}}_i, \hat{\mathbf{J}}_j] = i\hbar\varepsilon_{ijk}\hat{\mathbf{J}}_k, \tag{1.26}$$

where ε_{ijk} is the Levi-Cevita symbol that is antisymmetric (-1) under interchange of indices and invariant (+1) under cyclic permutations. To develop a formalism for molecular rotation, the $\hat{\mathbf{J}}_k$ operators are associated with the components of the angular momentum along the space-fixed axes X, Y, Z. From Eq. (1.26), a new operator $\hat{\mathbf{J}}^2$ is defined:

$$\hat{\mathbf{J}}^2 \equiv \hat{\mathbf{J}}_X\hat{\mathbf{J}}_X + \hat{\mathbf{J}}_Y\hat{\mathbf{J}}_Y + \hat{\mathbf{J}}_Z\hat{\mathbf{J}}_Z, \tag{1.27}$$

such that $\hat{\mathbf{J}}^2$ commutes with each $\hat{\mathbf{J}}_k$:

$$[\hat{\mathbf{J}}^2, \hat{\mathbf{J}}_k] = 0 \quad (k = X, Y, Z). \tag{1.28}$$

Since the $\hat{\mathbf{J}}_k$, do not commute with themselves, their eigenvalues can not simultaneously measured. By convention, $\hat{\mathbf{J}}_Z$ is chosen to commute with $\hat{\mathbf{J}}^2$.

A slight complication arises because the molecular coordinate system must also be considered. Both the molecular and space-fixed coordinate systems can be chosen to share the centre of mass as a common origin. The coordinate transformation between the space-fixed and molecular coordinate systems leads to [4]:

$$[\hat{\mathbf{J}}_x, \hat{\mathbf{J}}_y] = -i\hbar\varepsilon_{xyz}\hat{\mathbf{J}}_z. \tag{1.29}$$

Note the anomalous negative sign in Eq. (1.29). In addition, $\hat{\mathbf{J}}^2$ is the angular momentum operator for both coordinate systems:

$$\hat{\mathbf{J}}^2 = \hat{\mathbf{J}}_x\hat{\mathbf{J}}_x + \hat{\mathbf{J}}_y\hat{\mathbf{J}}_y + \hat{\mathbf{J}}_z\hat{\mathbf{J}}_z = \hat{\mathbf{J}}_X\hat{\mathbf{J}}_X + \hat{\mathbf{J}}_Y\hat{\mathbf{J}}_Y + \hat{\mathbf{J}}_Z\hat{\mathbf{J}}_Z. \tag{1.30}$$

Since $\hat{\mathbf{J}}^2$, $\hat{\mathbf{J}}_Z$ and $\hat{\mathbf{J}}_z$ commute with each other, they have a simultaneous set of eigenfunctions, called the symmetric top wavefunctions, which are designated $\mid JKM\rangle$. The eigenvalues of these operators are given by [3, 4]:

$$\hat{\mathbf{J}}^2 \mid JKM\rangle \;=\; \hbar^2 J(J+1) \mid JKM\rangle, \tag{1.31}$$

$$\hat{\mathbf{J}}_z \mid JKM\rangle \;=\; \hbar K \mid JKM\rangle, \quad \text{and} \tag{1.32}$$

$$\hat{\mathbf{J}}_Z \mid JKM\rangle \;=\; \hbar M \mid JKM\rangle, \tag{1.33}$$

where J, K, and M are quantum numbers subject to the conditions:

$$J \;=\; 0, 1, 2, \ldots,$$

$$K \;=\; -J, -J+1, \ldots J-1, J, \quad \text{and}$$

$$M \;=\; -J, -J+1, -J+2, \ldots J.$$

The eigenfunctions $\mid JKM \rangle$ are orthogonal:

$$\langle J'K'M' \mid J''K''M'' \rangle = \delta_{J'J''}\delta_{K'K''}\delta_{M'M''}. \tag{1.34}$$

The Hamiltonian for rotation $\mathcal{H}_r^0$ was defined in terms of the operators $\hat{J}_x$, $\hat{J}_y$, and $\hat{J}_z$ as well as the molecular moments of inertia in Eq.(1.23). Thus, the matrix elements of $\hat{J}^2$ and $\hat{J}_z$ must appear on the diagonal in $\mathcal{H}_r^0$ in the $\mid JKM \rangle$ basis. The $\hat{J}_x$ and $\hat{J}_y$, however, yield matrix elements that connect states with $K \pm 1$ in $\mathcal{H}_r^0$ [4]. The matrix elements in $\mathcal{H}_r^0$ then can be expressed as follows [3,4]:

$$\langle JKM \mid \mathcal{H}_r^0 \mid JKM \rangle = \frac{\hbar^2}{4} \left\{ \left(\frac{1}{I_{xx}^0} + \frac{1}{I_{yy}^0} \right) \left[J(J+1) - K^2 \right] + \frac{2K^2}{I_{zz}^0} \right\}, \tag{1.35}$$

$$\begin{aligned}
\langle JKM \mid \mathcal{H}_r^0 \mid JK \pm 2M \rangle &= \frac{\hbar^2}{8} \left(\frac{1}{I_{xx}^0} - \frac{1}{I_{yy}^0} \right) [J(J+1) - K(K \pm 1)]^{1/2} \\
&\quad \times \; [J(J+1) - (K \pm 1)(K \pm 2)]^{1/2}. \tag{1.36}
\end{aligned}$$

In short, the rigid rotor Hamiltonian matrix contains elements that depend on quantum numbers J and K and on the molecular moments of inertia [3,4].

Molecules can be classified according to the relationships among the moments of inertia, as shown below [14]:

$$\text{Symmetric top} \quad I_{xx} = I_{yy} > I_{zz} \quad \text{or} \quad I_{xx} = I_{yy} < I_{zz}$$

$$\text{Spherical top} \quad I_{xx} = I_{yy} = I_{zz}$$

$$\text{Asymmetric top} \quad I_{xx} \neq I_{yy} \neq I_{zz}$$

$$\text{Linear} \quad I_{xx} = I_{yy}, I_{zz} = 0$$

By inspection, it can be seen that symmetric and spherical rotors are diagonal in $\mathcal{H}_r^0$ and yield closed analytical expressions for all values of J and K. For example, the rotational energy expression for spherical tops is given by the expression [15]:

$$E_r^0 = BJ(J+1), \tag{1.37}$$

where B is related to the moment of inertia through

$$B = \frac{h}{8\pi^2 c I_{xx}}. \tag{1.38}$$

For linear rotors, the isomorphic rotational Hamiltonian $\mathcal{H}_{r,iso}^0$ yields rotational energy eigenvalues given by [4]:

$$E_r^0 = B[J(J+1) - l^2], \tag{1.39}$$

where l is the vibrational angular momentum [4, 15]. Although the motion is vibrational in origin, it is included in Eq. (1.39) because it resembles a rotation [2]. For asymmetric tops, in contrast, general expressions cannot be derived because the $\mathcal{H}_r^0$ contains off-diagonal elements in K. Although ingenious transformations have been devised, numerical techniques are required to diagonalize the matrix for

general J [16].

Thus far only the case of a rigid rotor has been considered. A thorough interpretation of rotational motion, however, must include other contributions. One commonly observed deviation from the simple picture discussed above is that the rotational energy level spacings do not match those predicted by the rigid rotor model. In linear molecules, for example, the pure rotational transitions are spaced by less than the constant $2B$ predicted by Eq. (1.39) [16]. This observation implies that the moment of inertia and hence the internuclear distance changes as the molecule rotates [16]. In a linear molecule, which rotates end-over-end, the centrifugal force is directed along the internuclear axis and causes the bonds to stretch; the elongation grows more pronounced with increasing rotation [2]. The effect of the centrifugal force can be treated as a perturbation $\mathcal{H}_d$ in the Hamiltonian for the rigid molecule [15]:

$$\mathcal{H}_{rot} = \mathcal{H}_{rot}^0 + \mathcal{H}_d. \tag{1.40}$$

The eigenvalues can be expressed as a power series expansion in $J(J+1)$ [17]:

$$E_J = B_0 J(J+1) - D_0 J^2(J+1)^2 + H_0 J^3(J+1)^3 + \ldots. \tag{1.41}$$

The coefficients $D, H \ldots$ are known as centrifugal distortion constants. Since each subsequent coefficient decreases by about a factor of 10^{-4} or more, the series converges rather quickly (especially for low J), and it is rare to observe terms that involve coefficients higher than M [17].

1.3.2   Vibration

In the harmonic oscillator approximation, the molecule is treated as a set of atoms joined by springs. The molecular vibrations in this picture are limited to small displacements about the equilibrium configuration. An additional simplification can be introduced by expressing the basis functions $\mid v\rangle$ as the product of the normal modes of vibration [4,11],

$$\mid v\rangle = \prod_{k=1}^{\substack{3N-5\,or\\3N-6}} \mid Q_k\rangle. \tag{1.42}$$

Thus, the problem is separated into $3N - 6$ (or $3N - 5$ for the linear case) independent equations for each normal mode Q_k. The eigenvalues of the approximate Hamiltonian $\mathcal{H}_v^0$ are obtained from the one-dimensional harmonic oscillator equation:

$$\mathcal{H}_v^0 \mid Q_k\rangle = E_v \mid Q_k\rangle, \tag{1.43}$$

$$\text{such that} \quad E_v = h\nu_k(v_k + \tfrac{1}{2}), \tag{1.44}$$

where $v_k = 0, 1, 2 \ldots$ is the vibrational quantum number. Each harmonic oscillator wavefunction is the product of a Hermite polynomial and a Gaussian [4,11] function.

The total vibrational energy is obtained by summing over all of the normal mode contributions. The ground state vibrational energy is non-zero and can be expressed as [4]:

$$E_v^0 = \frac{1}{2} \sum_{k=1}^{\substack{3N-5\,or\\3N-6}} h\nu_k. \tag{1.45}$$

In molecular spectroscopy, the energy levels are usually expressed in terms of the wavenumber, in units of cm^{-1}. The vibrational energy levels then given by [14]:

$$G(v_1, v_2, \ldots) = \frac{E_0}{hc} = \sum_k \omega_k (v_k + \tfrac{1}{2}), \qquad (1.46)$$

where ω_k is the wavenumber of the kth normal mode of vibration.

It is useful to apply group theory to molecular vibrational motion. In the ground state, the harmonic oscillator wavefunction and hence the vibration, is associated with the totally symmetric irreducible representation of the point group. When the vibration in non-degenerate, the levels with v_k even will always be associated with the totally symmetric irreducible representation, and the odd v_k will belong to the same irreducible representation as the normal coordinate Q_k. The symmetries of the vibrational wavefunctions are used to determine whether a particular transition between vibrational energy levels is allowed, as will be discussed in Section 1.3.4.

The harmonic oscillator model treats each vibration independently, and does not account for interactions among the different normal modes. In a higher level of approximation, the harmonic oscillator treatment is modified to include contributions that arise from cubic and higher terms in the potential energy (Eq. (1.6)). It is possible to use a perturbative approach to obtain an energy expression that includes anharmonic effects summed over the normal modes of vibration [17, 18]:

$$\begin{aligned} G(v_1, v_2 \ldots) &= \sum_{i=1} \omega_i (v_i + \tfrac{d_i}{2}) + \sum_{i=1} \sum_{k \geq i} x_{ik} (v_i + \tfrac{d_i}{2})(v_k + \tfrac{d_k}{2}) \\ &+ \sum_i \sum_{k \geq i} g_{ik} l_i l_k + \ldots \end{aligned} \qquad (1.47)$$

In Eq. (1.47) the $d_{i,k}$ equal 1 for nondegenerate or 2 for degenerate modes. The l are associated with the vibrational angular momentum. The x_{ik} and g_{ik} terms depend on the cubic and quartic potential energy constants as well as on the fundamental vibration frequencies ω_i and the moments of inertia. For small molecules, it is sometimes possible to determine the coefficients experimentally [19].

1.3.3 Rotation-Vibration Interactions

Another important phenomenon that is neglected in the lowest order picture is the interaction of rotation with vibration. One effect of the interaction is the variation of the rotational constants with the vibrational state. On an intuitive level, this might be anticipated because the molecular motion is a superposition of both the rotational and vibrational motion. Thus, the rotational constants would be expected to depend in a complicated way on the vibrational state. This imposes a limit on the constants derived from experimental data, since it is only possible to determine effective rotational constants in a given vibrational state.

For a linear molecule, the effective rotational constant may be expressed as:

$$B_v = B_e - \sum_{i=1}^{3N-5} \alpha_i(v + \tfrac{d_i}{2}) + \ldots \tag{1.48}$$

If the rotational constants are known for the ground state and the appropriate excited vibrational states, then α and B_e, the rotational constant for the equilibrium position, can be determined. The α terms depend on harmonic and anharmonic contributions from the potential energy as well on the Coriolis force, which is neglected in the rigid rotor, harmonic oscillator picture. An object that moves relative

to a rotating coordinate system will experience a Coriolis force given by [3]:

$$\vec{F}_{Cor} = 2m(\vec{\omega} \times \vec{v}_a) = 2mv_a\omega\sin\vec{\phi}, \tag{1.49}$$

where m is the mass of the particle, ω is the angular frequency of the coordinate system, v_a is the velocity of the object, and ϕ is the angle between the axis of rotation and the direction of the velocity v_a. Eq. (1.49) reveals that the Coriolis force is perpendicular to the plane that contains the axis of rotation and the direction of v_a. Thus, in a rotating molecule, the atoms will be pushed in the direction perpendicular to the vibration. In some cases, the Coriolis force will cause the nuclei to move in the same direction as one of the other modes of vibration, but with the frequency of the original vibration.

Fig. 1.2 illustrates the effect of the Coriolis force on an XYZ molecule. The Coriolis force acting on the ν_1 stretch will excite the ν_2 mode but at the frequency of ν_1; the converse is also true. If frequencies of ν_1 and ν_2 are similar then both of the modes will be excited. For the ν_3 stretch, the result is a rotation rather than another vibration. Using group theory, it can be shown that two modes will couple through a Coriolis interaction if the direct product of their irreducible representations contains one of the representations of the rotations [14].

The Coriolis interaction is small when two frequencies are widely different. The effect can be treated as a perturbation on the rigid rotor harmonic oscillator Hamiltonian, and is absorbed in the parameter α [18]. When the two interacting frequencies lie close in energy, however, perturbative approaches break down [20]. The treatment of these strong types of Coriolis interactions are described in Chapter 3.
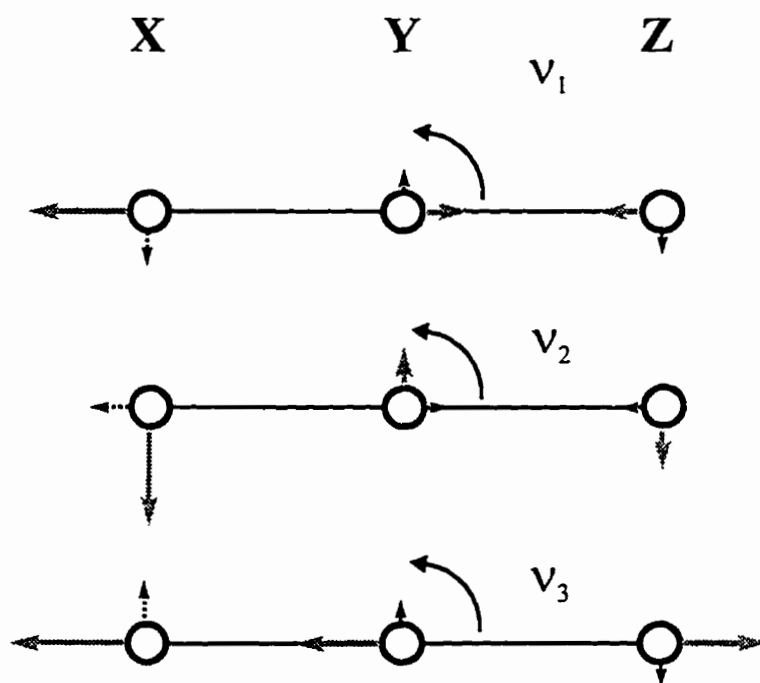
Figure 1.2: The effect of the Coriolis force on the normal modes of an XYZ linear molecule. The grey arrows denote the normal modes of vibration while the black arrows indicate the Coriolis forces on each atom (not to scale) [14].

1.3.4 Selection Rules

To interpret molecular vibrational-rotational spectra, the selection rules that govern the absorption and emission of photons between different energy levels must be considered. Within the rigid rotor, harmonic oscillator model, a transition will occur as long as the following condition is met [4, 11]:

$$\langle v'r' \mid \hat{\mathbf{d}}_Z \mid v''r'' \rangle \neq 0, \tag{1.50}$$

where $\hat{\mathbf{d}}_Z$ is the electric dipole moment operator along the space-fixed axis Z. After some manipulation, the dipole moment operator can be formulated in terms of the molecule-fixed axes x, y, z [11]:

$$\langle v'r' \mid \hat{\mathbf{d}}_{\mathbf{Z}} \mid v''r'' \rangle = \sum_{\alpha=x,y,z} \langle v' \mid \hat{d}_\alpha \mid v'' \rangle \langle \cos(ZO\alpha)r' \mid r'' \rangle . \tag{1.51}$$

The cosine argument $(ZO\alpha)$ is the angle formed between the unit vectors along the space-fixed axis Z and the molecule-fixed axis x, y, or z with the shared centre of mass origin.

It is possible to expand the dipole moment operator $\hat{d}_\alpha$ in a Taylor series about the normal coordinate equilibrium positions [11]:

$$\begin{aligned}
\hat{d}_\alpha(Q_1, ... Q_{3N-6}) &= d_{\alpha,e} + \sum_{k=1}^{3N-6} \left(\frac{\partial d_\alpha}{\partial Q_k} \right)_e Q_k \\
&+ \frac{1}{2} \sum_{j=1}^{3N-6} \sum_{k=1}^{3N-6} \left(\frac{\partial^2 d_\alpha}{\partial Q_j \partial Q_k} \right)_e Q_j Q_k + \dots . \tag{1.52}
\end{aligned}$$

The linear terms can be substituted in Eq. (1.51) to yield [11]:

$$\langle v' \mid \hat{d}_Z \mid v'' \rangle \;=\; \langle v' \mid v'' \rangle \sum_{\alpha=x,y,z} d_{\alpha,e} \langle \cos(ZO\alpha)r' \mid r'' \rangle \quad + \tag{1.53}$$

$$\sum_{k=1}^{3N-6} \langle v' \mid Q_k \mid v'' \rangle \sum_{\alpha=x,y,z} \left(\frac{\partial d_\alpha}{\partial Q_k} \right)_e \langle \cos(ZO\alpha)r' \mid r'' \rangle \,.$$

Since the $\mid v \rangle$ are orthogonal, the first term in Eq. (1.53) will disappear unless $v' = v''$. Thus, the first term corresponds to rotational transitions within the same vibrational state. These pure rotational transitions are forbidden unless the molecule possesses a permanent electric dipole in its equilibrium configuration. The pure rotational selection rules for the rotational quantum numbers J and K arise from the direction cosine terms, and differ according to whether the molecule is a symmetric, linear, or asymmetric top [15].

The selection rules for a vibrational transition are controlled by the second part of Eq. (1.53). The basis functions $\mid v \rangle$ can be written as the product of the individual normal modes, as shown in Section 1.3.2. From the properties of the Hermite polynomials, the condition arises that $\Delta v_k = \pm 1$ while all the other modes remain in their initial levels [11]. This means that one normal mode at a time can absorb or emit one quantum of radiation during the transition. The second term also depends on the derivative of the dipole moment with respect to the coordinate Q_k, and thus a change in the dipole moment must occur for a normal mode to be infrared active. A particular transition is designated parallel, perpendicular, or hybrid depending on the orientation of the changes in the dipole moment with respect to the molecular z axis. Moreover, the second term in Eq. (1.53) reveals

that rotational transitions will accompany a vibrational transition; the selection rules arise from the direction cosine terms, as for the pure rotational transitions. Thus any vibrational transition will be accompanied by rotational fine structure.

Group theory provides an expression of the vibrational selection rule in terms of the irreducible representations Γ. The integral $\langle Q'_k \mid \hat{d}_\alpha(Q_k) \mid Q''_k \rangle$ must be even to be non-vanishing. The infrared selection rule may be expressed in terms of group theory because each Q_k transforms according to an irreducible representation. For a vibrational transition to be infrared-allowed, the direct product $\Gamma(Q'_k) \times \Gamma(\hat{d}_\alpha(Q_k)) \times \Gamma(Q''_k)$ must contain the totally symmetric representation in order to be non-zero. This alternate formulation leads to a simple rule: a fundamental transition is allowed if the excited vibrational level $v_k = 1$ belongs to the same irreducible representation as one of the components of the dipole moment operator $\hat{d}$. The irreducible representations of $\hat{d}_{x,y,z}$ belong to the same irreducible representation as the translations, x, y, z that are obtained from the appropriate character table by inspection.

The rotational-vibrational selection rules are derived within the rigid rotor, harmonic oscillator framework. The procedure is similar for linear molecules as long as the approximate isomorphic Hamiltonian given in Eq. (1.25) is considered. Both of these treatments, however, neglect the cubic and higher-order terms. The higher-order anharmonic terms relax the selection rules and allow overtone and combination to appear. Overtone bands occur when a transition has $\Delta v = \pm 2, \pm 3, \pm 4 \ldots$, and combination bands are observed when more than one vibrational quantum number changes during a transition. A hot band is observed when a transition

occurs between two excited vibrational levels. For overtone and combination bands the irreducible representation for the upper vibrational level is obtained by taking the direct product of the symmetry species. The procedure is straightforward unless degenerate modes are involved, in which case recursion relations can be used [21]. For hot bands, the irreducible representation lower level of the transition must be obtained as well.

The intensities of electric-dipole allowed transitions are proportional to the square of the magnitude of the dipole moment integral:

$$I \propto |\langle v'J' \mid \hat{d}_z \mid v''J'' \rangle|^2 \tag{1.54}$$

Since not all vibrational transitions involve the ground state, the intensities also depend on the population of the levels relative to the zero-point level, which are given by the appropriate rotational and vibrational Boltzmann factors [7]. Thus, the intensities of the observed rotational energy transitions depend on line strength factors scaled by the appropriate rotational and vibrational Boltzmann factors.

1.4 Infrared Spectroscopy

The previous sections have outlined a treatment for molecular vibration and rotation, and now the discussion proceeds to the spectroscopic observations themselves. From the vibrational selection rules, it is found that all molecules except homonuclear diatomics possess at least one transition that is infrared allowed. An infrared spectrum appears as one or more bands centered at the wavenumbers of

the vibrational transitions, which usually lie between 200 and 5000 cm^{-1} for the fundamentals. The relative intensities of the bands are determined by the square of the transition dipole given in Eq. (1.53).

Infrared spectroscopy is a powerful tool in chemical analysis because vibrational spectra contain information that can be used to elucidate the structure and bonding in molecules. Both quantitative and qualitative approaches have been developed to treat the wide diversity of chemical systems. Quantitative structural information can be obtained from infrared measurements that resolve the rotational fine structure accompanying vibrational transitions. With a few exceptions, rotational structure is observed only in the gas phase [11]. The observed line positions, which correspond to differences between energy levels, can be fit to the models described in Section 1.3.1. The analysis yields molecular parameters, such as rotational distortion constants, that can be used in the elucidation of molecular structure. An illustration of the high-resolution analysis of infrared spectra is described in Chapter 3.

Perhaps the most ubiquitous application of infrared spectroscopy is as a qualitative tool for chemical analysis. To chemists, it is well known that numerous vibrational bands can be associated with certain structural units within a molecule. For example, the OH group in a large number of molecules vibrates between 2900 and 3900 cm^{-1}. It is evident that the simple picture of a molecule as a set of harmonic oscillators is not that far-fetched! This correlation of functional groups with specific wavenumber regions are useful probes of molecular structure. In addition, the region between 800-1400 cm^{-1} contains vibrations that involve the molecule as

a whole; since the pattern of bands is unique to a particular molecule, this spectral range is aptly known as the fingerprint region. Chapter 4 illustrates the qualitative approach in infrared spectroscopy to the investigation of the nucleic acid bases, a class of biological molecules.

Chapter 2

Fourier Transform Spectroscopy

2.1 Overview

The origin of Fourier transform spectroscopy can be traced to the invention of the two-beam interferometer by Michelson in the latter part of the nineteenth century [22]. A schematic of the Michelson interferometer is shown in Figure 2.1 [23]. The key optical components are a beamsplitter, two perpendicular mirrors, and a detector. Radiation from a source (S) encounters a beamsplitter (O) that reflects part of the light to a fixed mirror (F), and transmits part of the light to a movable mirror (M). The mirrors reflect the beams back to the beamsplitter, where they undergo interference. The intensity of the interference pattern depends on 2(OM-OS), the optical path difference between the two beams. The recombined beams then are partially reflected to the detector and partially transmitted back to the source. The detector measures the intensity of the interference pattern as a function of 2(OM-OS) as the movable mirror travels over its length; the recorded

signal is known as the interferogram. Michelson was the first to realize that the interferogram and the spectrum of the incident light are related through a Fourier transformation [22]. In 1887, he reported the earliest application of the technique: the calculation of a spectrum of the sodium D lines [22].

To begin a description of Fourier transform spectroscopy, it is helpful to consider how the Michelson interferometer affects the input from a monochromatic source. If the beamsplitter divides the radiation into two beams of equal amplitude I', the intensity of the recombined radiation that is measured by the detector is given by [24, 25]:

$$I(y) = 0.5I'(\overline{\nu})\{1 + \cos 2\pi\overline{\nu}y\}, \tag{2.1}$$

where the argument of the cosine function depends on the wavenumber of the incident radiation $\overline{\nu}$, and the optical path difference y. The interferogram is defined as the modulated component of the intensity [24, 25],

$$I(y) = 0.5I'(\overline{\nu})\cos(2\pi\overline{\nu}y). \tag{2.2}$$

In practice, the intensity $I'(y)$ depends not only on the radiation source, but on a number of additional factors such as the detector response and the efficiency of the optical components. Thus it is more appropriate to rewrite Eq. (2.2) as [24],

$$\begin{aligned} I(y) &= 0.5H(\overline{\nu})I'(\overline{\nu})\cos 2\pi\overline{\nu}y \\ &\equiv B(\overline{\nu})\cos 2\pi\overline{\nu}y, \end{aligned} \tag{2.3}$$

where $H(\overline{\nu})$ is an instrumental correction term. The quantity $0.5H(\overline{\nu})I'(\overline{\nu})$, des-
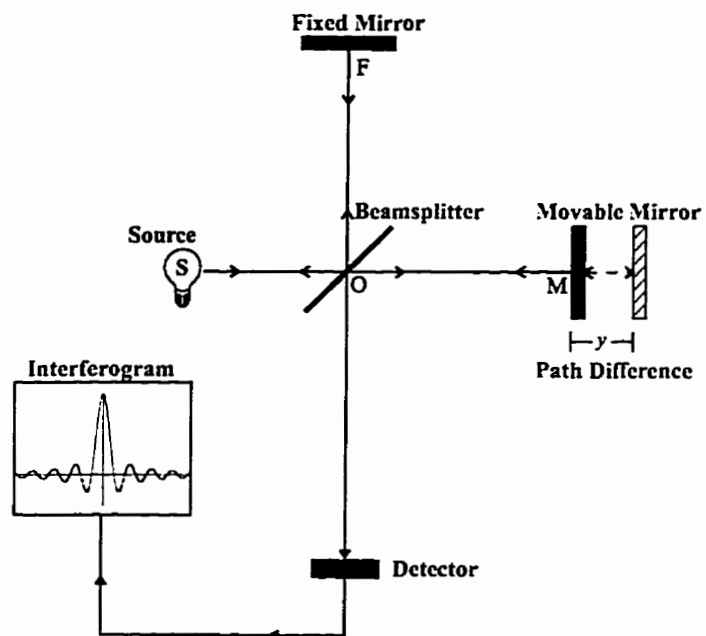
Figure 2.1: A schematic of the Michelson interferometer [23].

ignated $B(\overline{\nu})$, corresponds to the intensity of the source when the instrumental characteristics are considered. Since $I(y)$ and $B(\overline{\nu})$ are related through a cosine Fourier transform, the spectrum of the source can be calculated from the interferogram.

The intensity variation in the interferogram for a continuous source is more complex than for a monochromatic one. Each wavenumber element in the interferometer produces its own characteristic interference pattern as the movable mirror is displaced. The interferogram of a polychromatic source can be represented by [24, 25]:

$$I(y) = \int_{-\infty}^{\infty} B(\overline{\nu}) \cos 2\pi \overline{\nu} y d\overline{\nu}. \tag{2.4}$$

The cosine Fourier transform of Eq. (2.4) yields the spectral intensity:

$$
\begin{aligned}
B(\overline{\nu}) &= \int_{-\infty}^{\infty} I(y) \cos 2\pi \overline{\nu} y dy \\
&= 2 \int_{0}^{\infty} I(y) \cos 2\pi \overline{\nu} y dy.
\end{aligned}
\tag{2.5}
$$

Thus, the interferogram, the plot of intensity versus optical path difference, can be transformed to the spectrum, the plot of intensity versus wavenumber. Fourier transform spectroscopy, in essence, converts information from the distance to the wavenumber domain [24, 25].

The calculation of the conventional Fourier transform of an interferogram is a formidable task: for a transform that contains N points, $2N^2$ operations must be carried out [25]. Although Michelson invented an analog computer for his calculations [22], it is clear why he was not able to progress beyond simple line spectra.

Indeed, the Fourier transform technique required the advent of digital computers to become feasible. With the development of novel algorithms such as the fast Fourier transform in 1966 [24], as well as continuous improvements in computing power, the practical realization of Fourier spectroscopy has became commonplace.

2.2   Implementing the Fourier Transform

The Fourier transform pair given in Eqs. (2.4) and (2.5) do not account for experimental constraints. One example is that the intensity can not be measured over an infinite path difference, as the integration limits demand. The restriction to finite path difference results in the truncation of the interferogram, which can be expressed as the multiplication of the interferogram by a box function, $D(y)$. If the maximum path difference is labelled Φ, then the spectrum that is realized in practice is given by [24]:

$$\tilde{B}(\overline{\nu}) = 2 \int_0^\infty I(y)D(y) \cos 2\pi\overline{\nu}y \, dy, \tag{2.6}$$

$$\text{where} \quad D(y) = \begin{cases} 1 & \text{if } y \in [-\Phi, \Phi] \\ 0 & \text{otherwise.} \end{cases}$$

$\tilde{B}(\overline{\nu})$ is the integral of a product of two functions; the convolution theorem allows Eq. (2.6) to be written in terms of the individual Fourier transforms of $I(y)$ and $D(y)$ [23,24]:

$$\tilde{B}(\overline{\nu}) = 2 \int_0^\infty B(\overline{\nu}')f(\overline{\nu} - \overline{\nu}')d\overline{\nu}', \tag{2.7}$$

where the Fourier transform of the box function is given by [23, 24]:

$$
\begin{aligned}
f(\bar{\nu}) &= \frac{2\Phi \sin(2\pi\bar{\nu}\Phi)}{2\pi\bar{\nu}\Phi} \\
&= \operatorname{sinc}(2\pi\bar{\nu}\Phi).
\end{aligned}
\tag{2.8}
$$

Thus, the truncation of the interferogram leads to an experimental spectrum that can be represented as the convolution of the ideal spectrum with a sinc function.

The sinc function is usually designated the instrumental lineshape function because it modifies the appearance of the ideal spectrum $B(\bar{\nu})$ [24]. To illustrate, consider the convolution of the sinc function with a monochromatic frequency element of the input beam [24, 25],

$$
\tilde{B}(\bar{\nu}) = B(\bar{\nu}_o)2\Phi \operatorname{sinc}\left[2\pi(\bar{\nu}_o - \bar{\nu})\Phi\right].
\tag{2.9}
$$

Fig. 2.2 depicts the convolution of the two functions. The ideal spectrum $B(\bar{\nu}_o)$ is represented by two δ functions at $\pm\bar{\nu}_o$. In contrast, the sinc function has a height 2Φ and a full width at half height of $0.605\Phi^{-1}$; it also exhibits oscillating side-lobes that pass through zero on the abscissa. The convolution of both Fourier transforms yields two sinc functions localized at $\pm\nu_o$, which is the observed spectrum $B(\bar{\nu}_o)$. The side-lobes at the baseline are usually damped through the application of a weighting function to the interferogram, a process known as apodization [22, 24].

The resolution limit of the spectrometer depends on the maximum optical path difference Φ. Since the first zero of the sinc function occurs at $\nu_o \pm .5\Phi^{-1}$, two adjacent lines are said to be completely resolved if they are separated at least by

Φ^{-1} [24]. The resolution limit of the spectrometer then can be expressed as [24]:

$$\Delta\bar{\nu} = (\Phi_{\max})^{-1}. \tag{2.10}$$

It should be noted that the Eq. (2.10) represents an upper limit, but often the resolution will be somewhat higher because partially overlapping lines may still be resolved if they exhibit a dip of at least 20% between them [24].

The continuous nature of Eqs. (2.4) and (2.5) is another property of the Fourier transform pair that is never realized in the laboratory. Clearly, the signal at the detector can not be sampled at infinitely small intervals. Instead, the signal is digitized by sampling it at regular intervals of the optical path difference. Yet it can be shown that no loss of information will occur as long as one condition is met. As proved by Nyquist, a sinusoidal function of time or distance can be regenerated as long as it is sampled at a frequency greater than or equal to twice per cycle [25]. For an interferogram, the sampling rate Δx must fulfill the condition:

$$\Delta x = \frac{1}{2\bar{\nu}_{max}}, \tag{2.11}$$

where $\bar{\nu}_{max}$ is the highest wavenumber in the source. It is vital to ensure that the range of observed frequencies is within the limit given in Eq. (2.11); otherwise, spectral features will appear at incorrect wavenumbers, a phenomenon known as aliasing or folding [24].

Another practical consideration in Fourier transform spectroscopy is the imperfect collimation of the input radiation [24, 25]. Since the beam divergence causes a
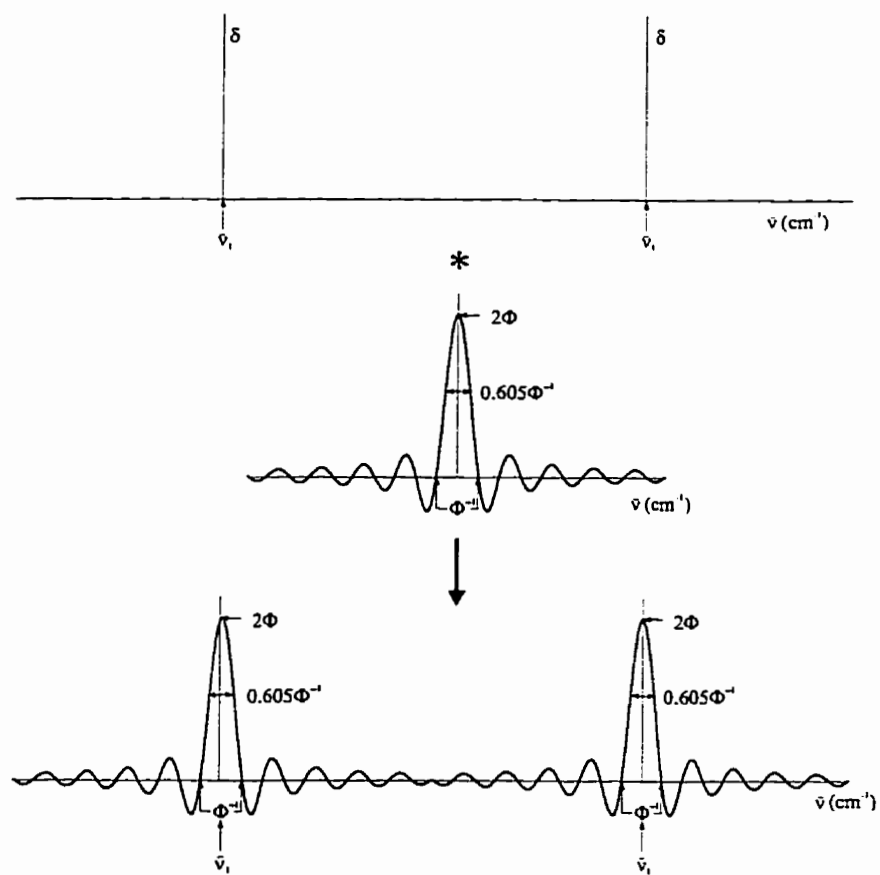
Figure 2.2: The sinc or instrumental lineshape function arises from the truncation of the interferogram. Φ is the maximum optical path difference in the spectrometer. The function modifies the shape of the peaks in the experimental spectrum, leading to finite widths and heights as well as to ringing at the baseline [23, 24].

spread in the path differences, this will lead to destructive interference unless the input radiation is limited by an aperture. The resolution of the spectrometer can be expressed in terms of the aperture diameter d and the maximum path length Φ [24, 25]:

$$\frac{\Delta \bar{\nu}}{\bar{\nu}_{max}} = \frac{d^2}{8\Phi^2} \tag{2.12}$$

The aperture limits the resolution that can be achieved with a particular Fourier transform spectrometer. Thus, the requirement for higher resolution must be balanced with the loss of signal associated with a smaller aperture.

2.3 Advantages and Disadvantages

When compared to dispersive instruments, Fourier transform spectrometers have two intrinsic advantages in sensitivity that can be exploited by careful experimental design. The first is known as the throughput or Jacquinot advantage [22,26]. Most dispersive instrument such as a monochromator requires narrow entrance and exit slits while a Fourier transform instrument has a circular entrance aperture. For a given maximum path difference and resolution, a greater portion of the input radiation hits the detector in a Fourier transform instrument; typically, there is a 10 to 250-fold increase in sensitivity over dispersive techniques in the infrared [24]. However, if the throughput is limited by another optical component such as the detector, the advantage may be reduced [23, 24].

A second advantage of a Fourier transform spectrometer over classical dispersive instruments is known as the multiplex or Felgett advantage [25]. During a

given measurement time T, a dispersive instrument scans sequentially through M spectral elements while a Fourier transform spectrometer detects all of the input radiation simultaneously for the full scan time. For instruments of comparable optical efficiency, it follows that an interferometer has a signal-to-noise advantage [26]:

$$\frac{(S/N)_i}{(S/N)_d} = \sqrt{M}, \qquad (2.13)$$

if the primary noise source is the detector. The Felgett advantage is greatest in the infrared where the dominant noise source is often the detector. Though still significant, the multiplex advantage tends to lose some of its importance as IR detectors are improved. In addition, the multiplex advantage becomes a disadvantage when the noise is source-limited because the Fourier transform instrument detects noise over all the spectral elements. Under such conditions, the overall sensitivity is reduced by a factor of $1/\sqrt{M}$ when compared to a dispersive instrument [25].

A particularly convenient feature of modern Fourier transform instruments is that the wavenumber measurement is very reproducible. This is achieved by passing the output from a visible laser through spectrometer along the same optical path as the input radiation. A separate detector measures the laser interference pattern. The zeroes in the laser signal, which occur at half-integral multiples of the laser wavelength, are used to trigger data acquisition. Although the precision is high, it is still necessary to calibrate the spectrum because even a slight misalignment of the laser beam with respect to the optical axis will cause a shift in the observed wavenumbers [24].

A drawback of commercial Fourier transform spectrometers is that they operate

as single beam instruments. Thus, the background spectrum, which contains the instrumental and the environmental contributions, is measured at a different time than the sample spectrum. Ideally the instrumental and environmental changes are eliminated by ratioing the sample spectrum to the background spectrum. Slight changes in the experimental conditions, however, can lead to spectral artifacts such as water vapor or carbon dioxide peaks. Dispersive instruments often are double beam and the measurements compensate for environmental changes in real time.

2.4 The Bruker IFS 120HR Fourier Transform Spectrometer

The Fourier transform experiments that are described in Chapters 3 and 4 have been carried out using a Bruker IFS 120HR Fourier transform spectrometer, which is based on the two-beam Michelson design. A schematic of the instrument is shown in Fig. 2.3. The instrumental design is flexible and allows for a wide selection of optical components, sources, and detectors that cover the spectral range from the far infrared to the near ultraviolet. The maximum optical path difference is 4.8 m, which corresponds to a maximum possible resolution of 0.0018 cm^{-1}. The divergence of the input beam is limited by a circular input aperture that can be modified in size from 0.5 to 12.5 mm. The modulated beam of radiation leaves the interferometer and passes through a filter that reduces the spectral range measured by a detector. Data acquisition is controlled with a single-mode He-Ne reference laser. The optical functions and the data handling, including the Fourier transform
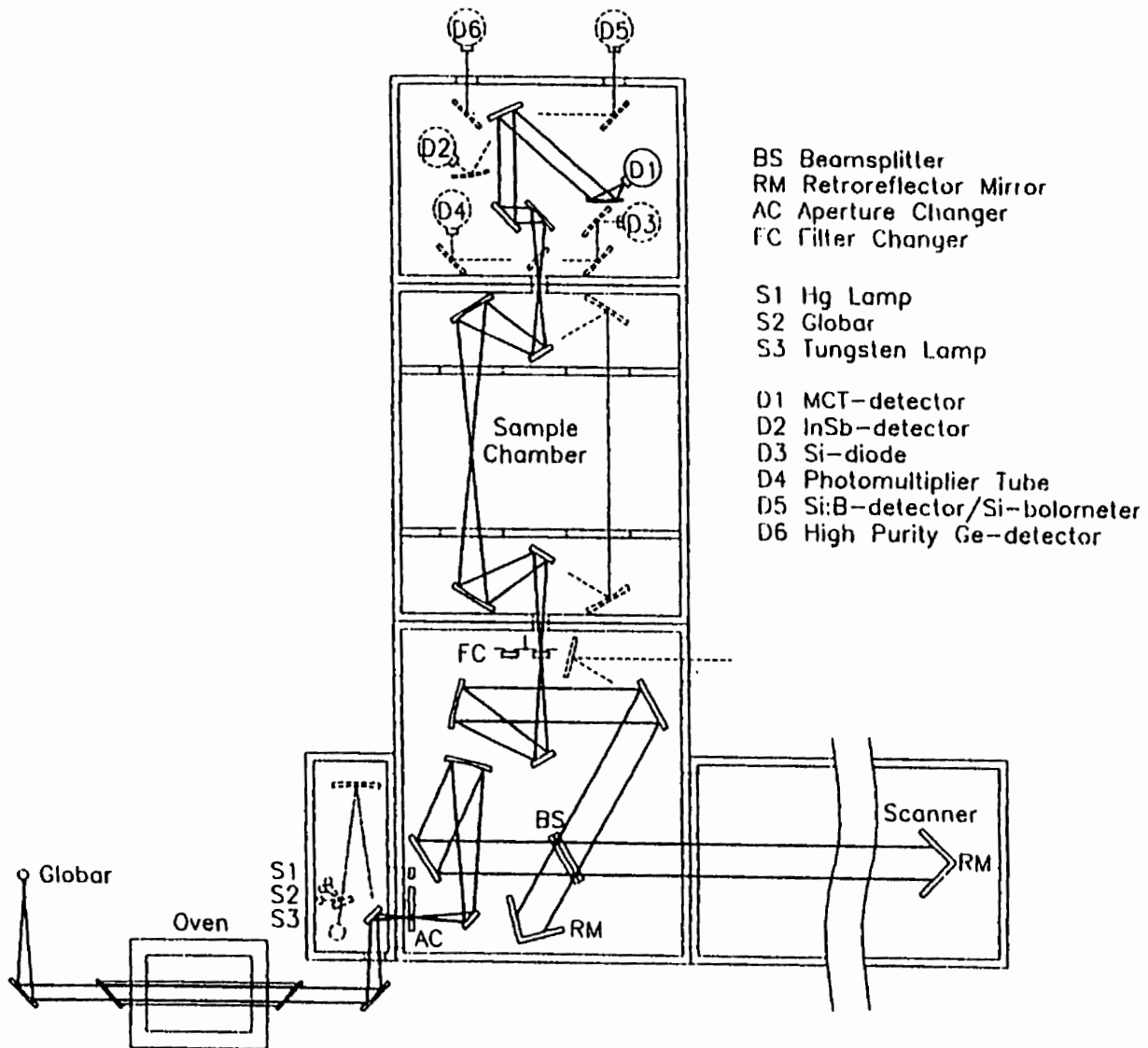
Figure 2.3: A schematic of the Bruker IFS 120HR spectrometer.

BS Beamsplitter
RM Retroreflector Mirror
AC Aperture Changer
FC Filter Changer

S1 Hg Lamp
S2 Globar
S3 Tungsten Lamp

D1 MCT-detector
D2 InSb-detector
D3 Si-diode
D4 Photomultiplier Tube
D5 Si:B-detector/Si-bolometer
D6 High Purity Ge-detector

of the interferogram, is carried out with the Bruker software package, OPUS 2.0.

2.5 Fourier Transform Infrared Spectroscopy

Infrared spectroscopy has become a standard tool in chemical analysis because all molecules, except for homonuclear diatomics, possess at least one infrared active vibrational mode. Working in the infrared, however, presents several challenges to the experimentalist. A fundamental limitation is that the transition dipole moments are approximately 0.1 debye in the infrared, which is an order of magnitude smaller than typical rotational and electronic transitions [27]. In addition, degradation of the signal-to-noise ratio occurs because ambient blackbody radiation peaks at about 1000 cm^{-1} [27, 28]. Another difficulty is that the infrared detectors and optical components are not as efficient as their visible or microwave counterparts [27, 28].

Despite the impediments, a number of techniques have been developed to work in the infrared region. The most sensitive infrared instruments are diode laser spectrometers, but a drawback is that the diode lasers have limited tunability and spectral coverage. With technological advances in non-linear techniques, such as in optical-parametric oscillators, the analog of the broadly tunable visible lasers may be become a reality. Other recent advances such as infrared array detectors have also led to improved sensitivities for dispersive techniques [28]. Fourier transform spectrometers, however, have been the most widely used instruments for the infrared since their commercialization in the early 1970's both for their convenience and ease of operation and because this region benefits most from the throughput and multiplex advantages.

Although typical infrared experiments are performed in absorption, it is also possible to carry out emission measurements in the infrared. Usually, emission spectroscopy is carried out in the visible or the ultraviolet because these regions contain little interference from ambient radiation. Indeed, techniques such as laser-induced fluorescence can be optimized until they are limited only by photonic shot noise in the optical detectors. Since the infrared region contains ambient black-body radiation, a temperature difference must exist between the sample and the background [27,28]. Although it is possible to record spectra with the sample temperature below room temperature, it is more common to heat the sample. Elevated temperatures enable higher signal-to-noise ratios, but in many cases only moderate temperatures can be used before thermal decomposition occurs.

Until recently, emission experiments were carried out with Fourier transform instruments because the losses with dispersive instruments were too high. Recent improvements in infrared detectors such as in array technology have achieved the required sensitivity to carry out emission experiments. In certain cases, dispersive instruments can show over a hundredfold improvement in sensitivity over Fourier transform spectrometers [28]. Nonetheless, such instrumentation is relatively new and costly, so the Fourier transform technique remains the practical choice for emission spectroscopy, at least for now.

Fourier transform infrared emission has proven to be a sensitive technique for remote sensing and astronomical measurements. For example, emission spectra from smokestack plumes have been recorded with a ground-based mobile Fourier transform spectrometer [29]. Infrared emission has also been used to monitor forest fires

from an airbone remote sensing platform [30]. Remote atmospheric observations of infrared emission have led to the observation of numerous atmospheric species that may play an important role in ozone depletion [31], and astronomical observations of infrared emission have also been achieved with the ISO satellite. These are only a few illustrations of the many applications of the infrared emission technique in the field. The data from these environmental measurements are used to develop models for the chemical composition and temperature profiles of the systems of interest.

In the laboratory, infrared emission measurements provide fundamental molecular data, which can also be used in remote sensing and astronomical measurements. One interesting application has been the investigation of transient species at high resolution. Though present in low concentrations, on the order of a fraction of a Torr, the spectra of certain transient metal hydrides have yielded a signal-to-noise ratio of more than 100 to 1 [32]. The interpretation of spectra leads to basic chemical information that has been used in the identification of species in the astronomical or high-energy applications. In Chapter 3, the infrared emission spectra of two high-temperature transient molecules, HBO and DBO, are described and analyzed at high resolution.

Infrared emission spectroscopy is also a sensitive technique in the mid- and far-infrared regions for the detection of large molecules. As has been shown for the polycyclic aromatic hydrocarbons, it is possible to acquire infrared spectra in emission at moderate temperatures [33]. The infrared emission spectra of the nucleic acid bases is discussed in Chapter 4.

Chapter 3

The Infrared Emission Spectra of HBO and DBO

3.1 Overview

Transient molecules are characterized by their high chemical reactivities and short lifetimes, and play an important role in the chemistry of high-energy systems, ranging from stellar atmospheres to industrial plasmas. The first observations of this elusive class of molecules were made in the 1920's, when fragments such as OH, CN, and CH were identified from their emission spectra in discharges and flames [18, 34]. Since the early observations, the investigation of transient species has been a dominant theme in molecular spectroscopy. Compilations of the spectroscopic literature in this area are available for both diatomic [35] and polyatomic [36] species.

Laboratory investigations provide the opportunity to study transient molecules

in controlled environments. Transient molecules require energetic conditions for their formation, and typical experiments draw on flame, discharge, flash photolysis, and high-temperature techniques. Since transient molecules are extremely reactive, it is convenient to study them in isolated environments. The gas phase is ideal because the interactions among neighboring molecules are minimized at low pressures. The matrix technique simulates the isolated conditions of gas-phase experiments: the transient species are diluted with an excess of rare gas and deposited onto a cold window that freezes the mixture [34]. Once trapped, most molecules will not rotate; the vibrational bands are extremely well-resolved, but contain little rotational structure. Often a matrix experiment provides the first identification of a transient species, which is then studied in greater detail in the gas phase. Both matrix and gas-phase data have lead to the characterization of numerous transient species [36].

High-resolution spectra (< 0.1 cm^{-1}) of gas-phase molecules are particularly useful because rotational line positions are used to characterize the vibrational-rotational motion as well as the molecular structure. Moreover, the data provide atlases that lead to the unambiguous identification of chemical species in different surroundings. High-resolution work can yield other types of quantitative data, including line widths and intensities, that can be used to model chemical systems.

This chapter describes a high-resolution study of the infrared spectra of two transient species, boron-oxyhydride, HBO, and its deuterated analog, DBO. These two linear molecules were first identified by Lory and Porter in a matrix experiment twenty-five years ago [37]. The gas-phase investigations reported here have led to

a detailed characterization of the vibrational-rotational motion of these species.

HBO is a linear closed shell molecule that contains ten valence electrons. Its electronic orbital configuration may be written as:

$$(1\sigma)^2(2\sigma)^2(3\sigma)^2(4\sigma)^2(5\sigma)^2(1\pi)^4 \quad \Sigma^+. \tag{3.1}$$

Recently, Yamaguchi *et al.* have examined the bonding in HBO using *ab initio* calculations at the self-consistent field level [38]. The results indicate that the 3σ orbital is primarily associated with the BO bond, the 4σ with the BH bond, and the 5σ with a lone pair on the O. The 1π is dominated by BO bonding, which suggests that a triple bond exists between the boron and the oxygen, at variance with the simple H-B=O valence bond structure.

While the other Group 13 elements (Al, In, Tl) form linear hydroxides [39, 40], boron occupies the central position in HBO. The species BOH has never been observed experimentally, which is consistent with theoretical calculations indicating that HBO lies 160 to 200 kJ/mol lower in energy than BOH [38, 41, 42]. An interesting note is that the isomerization of HBO to BOH may involve a transition from a linear to bent (or quasilinear) geometry [38, 41–43]. Once formed, BOH may be relatively easy to detect because the infrared bands are predicted to be significantly more intense than those of HBO [38, 41, 42].

HBO belongs to the family of simple transient boron-containing molecules that includes species such as BH, HBS, ClBS, BOB, and HOBO. It is probable that these unstable molecules are relevant to high-temperature boron chemistry. In particular, there has been a longstanding interest in using boron compounds as fuels because

these processes are very exothermic [44]. A review of the thermochemistry and kinetics of boron oxidation has appeared in the past year [44]. Some experimental evidence suggests that the trimerization of HBO may be an intermediate step in such processes because boroxine, $H_3B_3O_3$, has been observed as an end-product [45]. In addition, it has been suggested that HBO may be a bottleneck in the complete oxidation of boron [46].

3.2 Previous Spectroscopic Work

The vibrational motion of an unsymmetric linear XYZ molecule such as HBO is described in terms of $3(3) - 5 = 4$ normal modes of vibration. Using the classical approach outlined in Section 1.2, it can be shown that two of the normal modes are stretches (ν_1 and ν_3) while the other two are degenerate bends (ν_2). A more detailed characterization of the vibrational-rotational behavior of linear triatomics is given in Section 3.5.

HBO was first identified by Lory and Porter in 1972 [37]. $H_2B_2O_3$ was deposited in an argon matrix and photolyzed with 148.0 nm radiation from a xenon lamp or 184.9 nm radiation from a mercury lamp. The infrared absorption spectra revealed several vibrational bands that were consistent with the small linear species HBO. The ν_2 and ν_3 fundamental transitions were assigned for $H^{11}BO$ and $H^{10}BO$. In a similar procedure, DBO was generated from $D_2B_2O_3$; all of the fundamental bands were assigned for both deuterated isotopomers.

Subsequent experiments have further examined the infrared spectrum of HBO in matrix environments. Ault demonstrated that a mixture of diborane, B_2H_6,

and an oxidant could be irradiated with an excimer laser output at 193 nm to produce HBO [45]. The other major product was $H_3B_3O_3$; BH_3 was also tentatively identified. The previously assigned fundamental vibrational bands for HBO were observed as well as the corresponding bands for $HB^{18}O$ in an isotopically-enriched sample. In another infrared matrix experiment, Andrews and Burkholder used laser ablation to vaporize boron atoms, which were then reacted with $H_2^{16,18}O$ and $D_2^{16}O$ [47]. The reaction products were condensed with excess argon at cryogenic temperatures [47]. The spectra revealed that major products were HBO and BO with minor amounts of other transient boron species such as BOB and OBOB.

In the gas-phase, HBO has been generated in discharges of B_2H_6 and O_2 mixtures by Kawashima and co-workers [48–50]. They were able to characterize the pure rotational spectra of six HBO isotopomers, and also recorded the infrared spectrum of the ν_3 band of $H^{11}BO$ using an infrared diode laser spectrometer.

3.3 Experiment

The original purpose of the investigation was to record the infrared spectrum of boron monochloride. BF had been generated in a previous experiment by reacting boron powder and calcium fluoride at 1000°C [51], and it was thought that BCl could be produced in a similar reaction with the chloride salt. Two carbon boats were filled with approximately 5 g of amorphous boron (Aldrich) and 30 g of $CaCl_2$ (Aldrich), and were placed in a 120 cm long mullite ($3Al_2O_3 \cdot SiO_2$) tube. The 50 cm middle portion containing the reactants was housed in a high-temperature furnace (CM Rapid-Temp). Windows (KRS-5, >350 cm^{-1}) mounted on stainless

steel fittings were used to seal both ends of the tube, which was then evacuated through a pumping port. The furnace was heated at a rate of 5°C per minute up to 1400°C using a digital controller. Although mullite can withstand temperatures upward of 1500°C, the tube was heated slowly to prevent the formation of cracks. In addition, two jacks were used to support the tube at each end because mullite tends to soften at high temperatures.

The infrared radiation emitted from one end of the tube was directed into a Fourier transform spectrometer with an off-axis parabolic mirror. The region between the tube and the spectrometer was purged with dry nitrogen in order to reduce the contamination from atmospheric water and carbon dioxide. Survey scans at a resolution of 0.02 cm^{-1} were recorded as the tube was heated. The spectral range between 350 and 4000 cm^{-1} was monitored with a helium-cooled Si:B detector (350 -1500 cm^{-1}) as well as with nitrogen-cooled HgCdTe (denoted MCT) (800-1850 cm^{-1}) and InSb (1850-4000) cm^{-1} detectors. At 1000°C, spectral features near 700 cm^{-1} were observed that did not correspond to BCl, nor to any frequently observed molecules such as H_2O or CO_2. After a search of the VEEL4 database [36], the features were tentatively assigned to HBO.

The infrared emission from HBO was recorded over the interval between 350 and 4000 cm^{-1} at a resolution of 0.01 cm^{-1}. A Ge-coated KBr beamsplitter (350-4800 cm^{-1}) was used in all of the runs, and the wavenumber range measured by the detectors was narrowed with bandpass and redpass filters, depending on the wavenumber region of interest. The Fourier transform of each interferogram, each representing 50 averaged scans, was obtained with the Bruker Opus 2.0 software
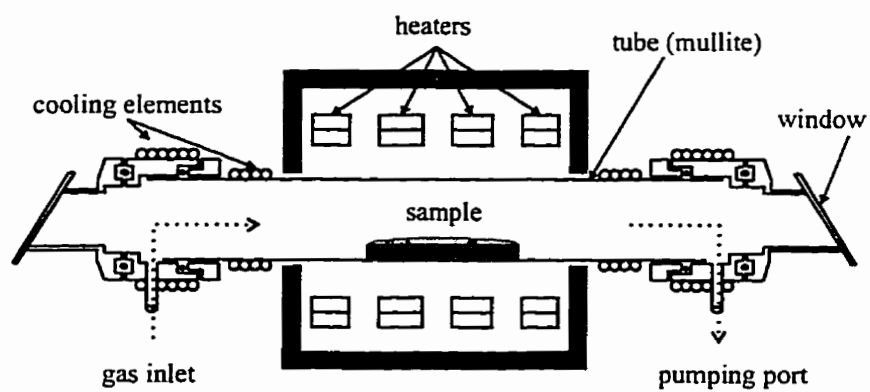
Figure 3.1: The ceramic tube furnace. Infrared emission from the hot molecules was directed from one end of the tube into the Fourier transform spectrometer.

Table 3.1: Some technical specifications for the spectra of HBO and DBO recorded in these experiments.

Scan	Range (cm^{-1})	Detector	Calibration factor (cm^{-1})
HBO	350–730	Si:B	1.000006257
	350–730	Si:B	1.000006257
	760–1300	Si:B	1.000004003
	1200–2100	MCT	1.000002738
	1800–4000	InSb	1.000001734
DBO	350–730	Si:B	1.000007214
	1800–4000	InSb	1.000002062

package. Spectra were collected at various temperatures, ranging from 1000 to 1400°C, and were calibrated with CO in the regions above 1400 cm^{-1} [52], and HCl in the regions below 700 cm^{-1} [53]. The region between 750 and 1200 cm^{-1} was calibrated against the corrected higher wavenumber region with the SiO lines that appeared in each spectrum. Technical specifications of the spectra are listed in Table 3.1.

Some examples of HBO infrared emission spectra are given in Figs. 3.2 to 3.6. All of the depicted HBO spectra were recorded at a temperature of 1400°C. The primary focus of the experiment was a thorough characterization of the vibrational-rotational properties of HBO, but the spectra revealed a rich chemistry that deserves further investigation. Several transient molecules besides HBO, including AlCl at 500 cm^{-1} and SiO at 1200 cm^{-1}, were identified in emission. SiO was

observed to form at temperatures greater than 1200°C, while AlCl formed between 1050-1300°C. The semistable molecule $HBCl_2$ and the stable molecule BCl_3 were also observed, but in absorption. HCl and CO were also present in both emission and absorption. Furthermore, several unidentified emission features were observed at 804, 1400 and 2900 cm^{-1}.

A number of experiments were carried out to determine the chemistry of HBO formation as well as the synthesis of other transient species. As a first step, the conditions of the first run were reproduced. HBO emission was observed starting at about 830-850°C, and $HBCl_2$ was detected at about the same temperatures. The diatomic molecules, SiO and AlCl, as well as the unidentified emission features were not detected except in the initial experiment. After each run, the contents of the tube were examined, and there was no observable depletion or discoloration of the boron sample.

To explore the chemistry of the HBO formation, attempts were made to react boron with water, but the signal from HBO was extremely weak. After the run, the contents of the tube revealed a thin glassy film, which may have been B_2O_3. A similar reaction of solid boron and D_2O showed no evidence of DBO formation. In some final experiments, HBO was generated by simply heating boron in the mullite tube. It was also found that the deuterated species, DBO, could be produced by introducing deuterium into the tube once HBO was observed. The DBO spectra were recorded at 1200°C over two spectral intervals, including 350 to 700 cm^{-1} and 1400 to 2600 cm^{-1}, and are given in Figs. 3.7 and 3.8.
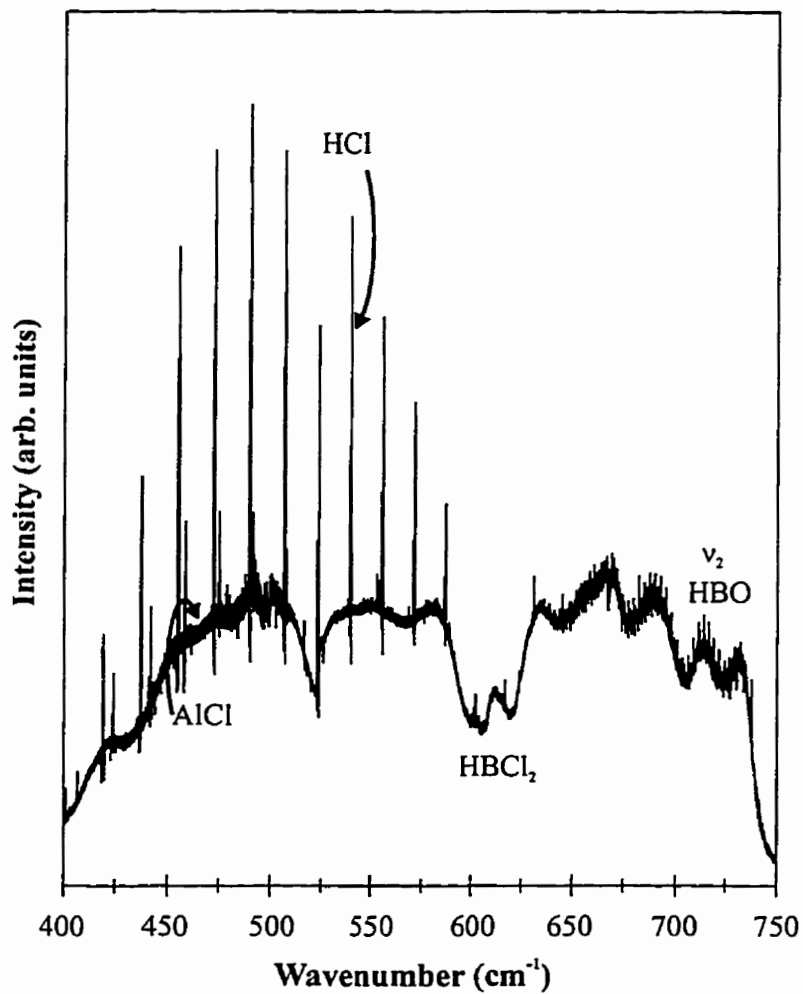
Figure 3.2: The spectrum obtained with a helium-cooled Si:B detector (filter 1: 350-750 cm^{-1}). The HBO spectrum begins at about 600 cm^{-1}. Emission from impurities, HCl and AlCl are visible. An absorption band of HBCl$_2$ is present as well.
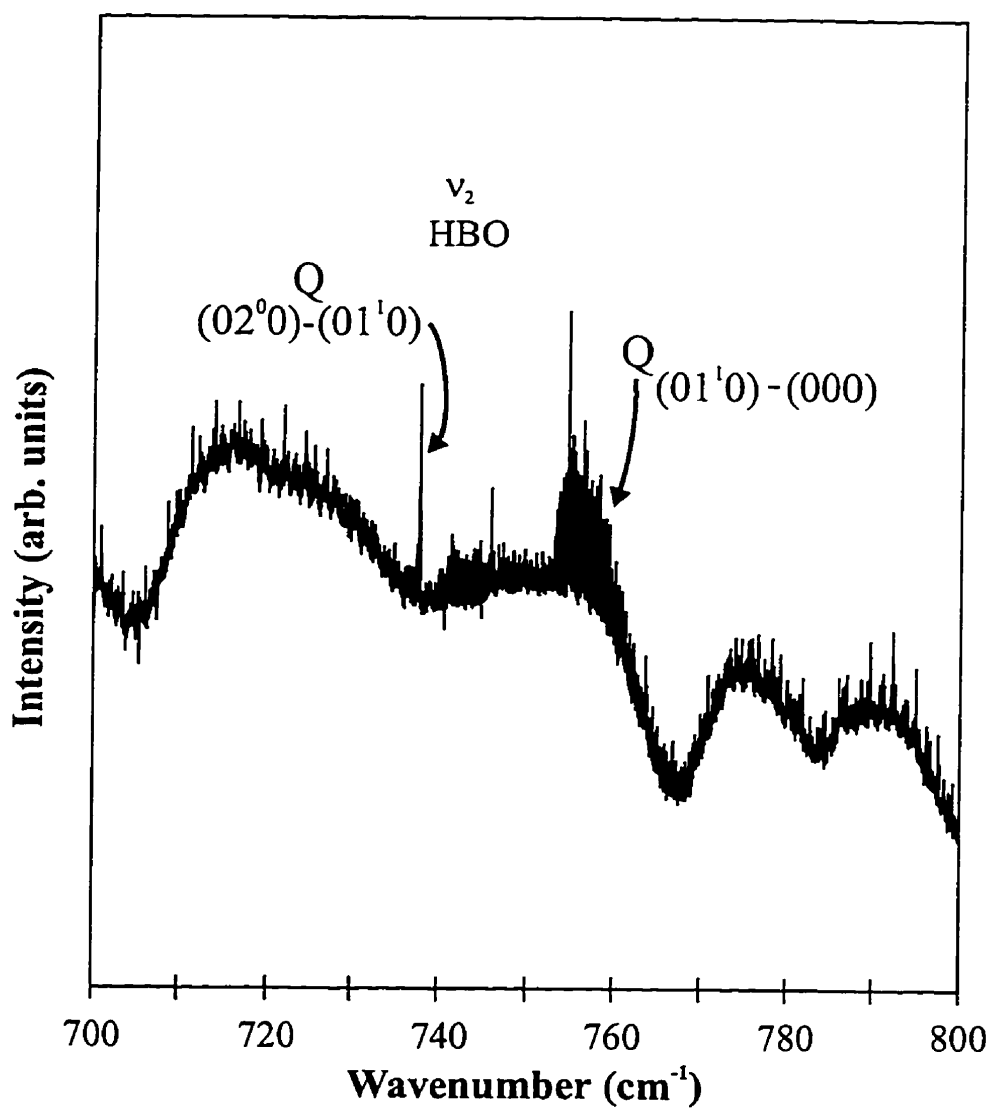
Figure 3.3: A detail of the HBO emission spectrum between 700-800 cm^{-1} obtained with a helium-cooled Si:B detector (filter 2: 400-750 cm^{-1}).
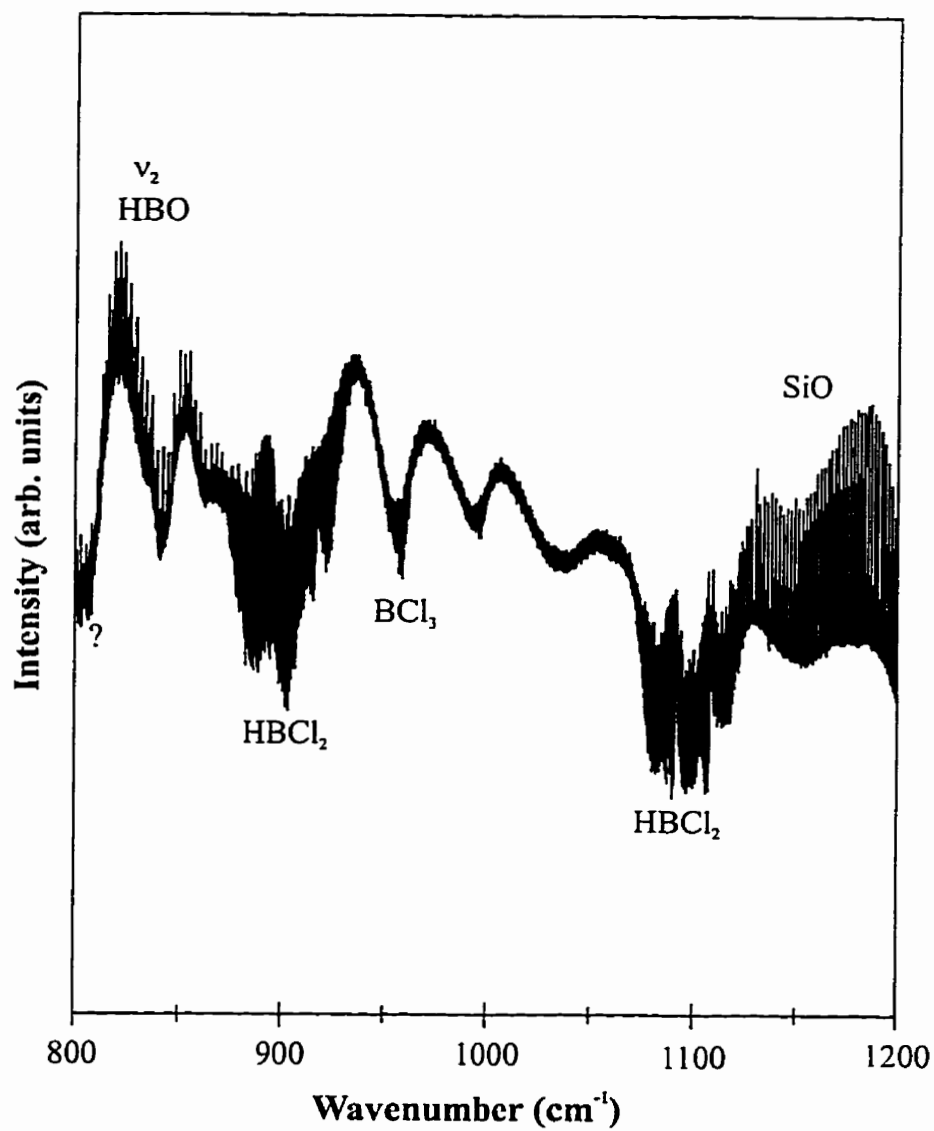
Figure 3.4: The spectrum obtained with a helium-cooled Si:B detector (filter 3: 800-1200 cm^{-1}). The HBO spectrum is obscured above approximately 850 cm^{-1} by an absorption band of HBCl$_2$. The emission spectrum of SiO is seen above 1100 cm^{-1}. An unidentified band occurs near 800 cm^{-1}.
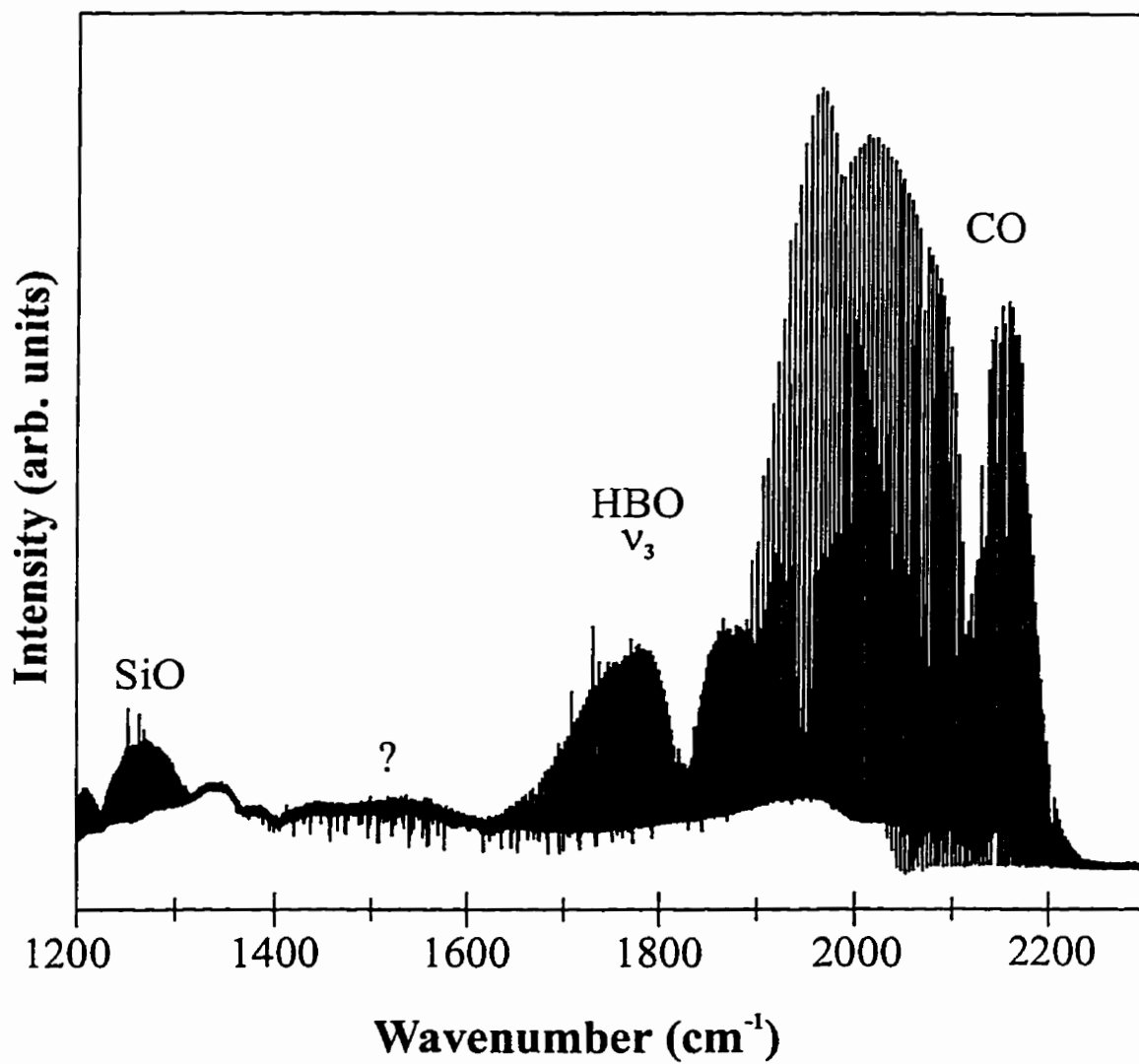
Figure 3.5: The spectrum obtained with a nitrogen-cooled MCT detector. HBO emission is observed between 1600 and 2000 cm^{-1}. Emission spectra of SiO and CO are also visible. An unidentified feature occurs near 1500 cm^{-1}.
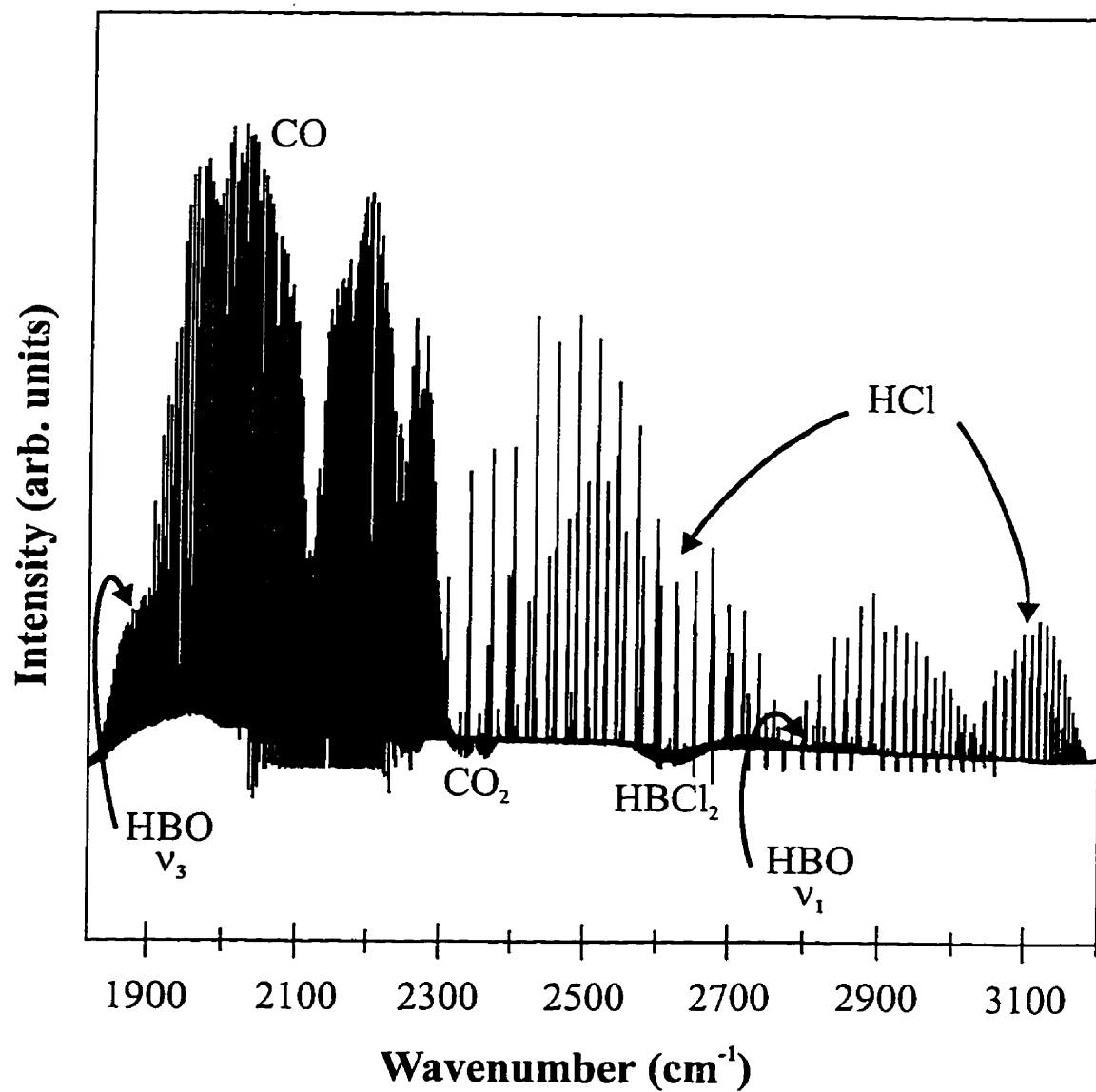
Figure 3.6: The spectrum obtained with a nitrogen-cooled InSb detector. HBO emission is observed between 1900 and 2000 cm^{-1} as well as between 2650 and 2900 cm^{-1}. CO, HCl, CO_2, and $HBCl_2$ are also visible.
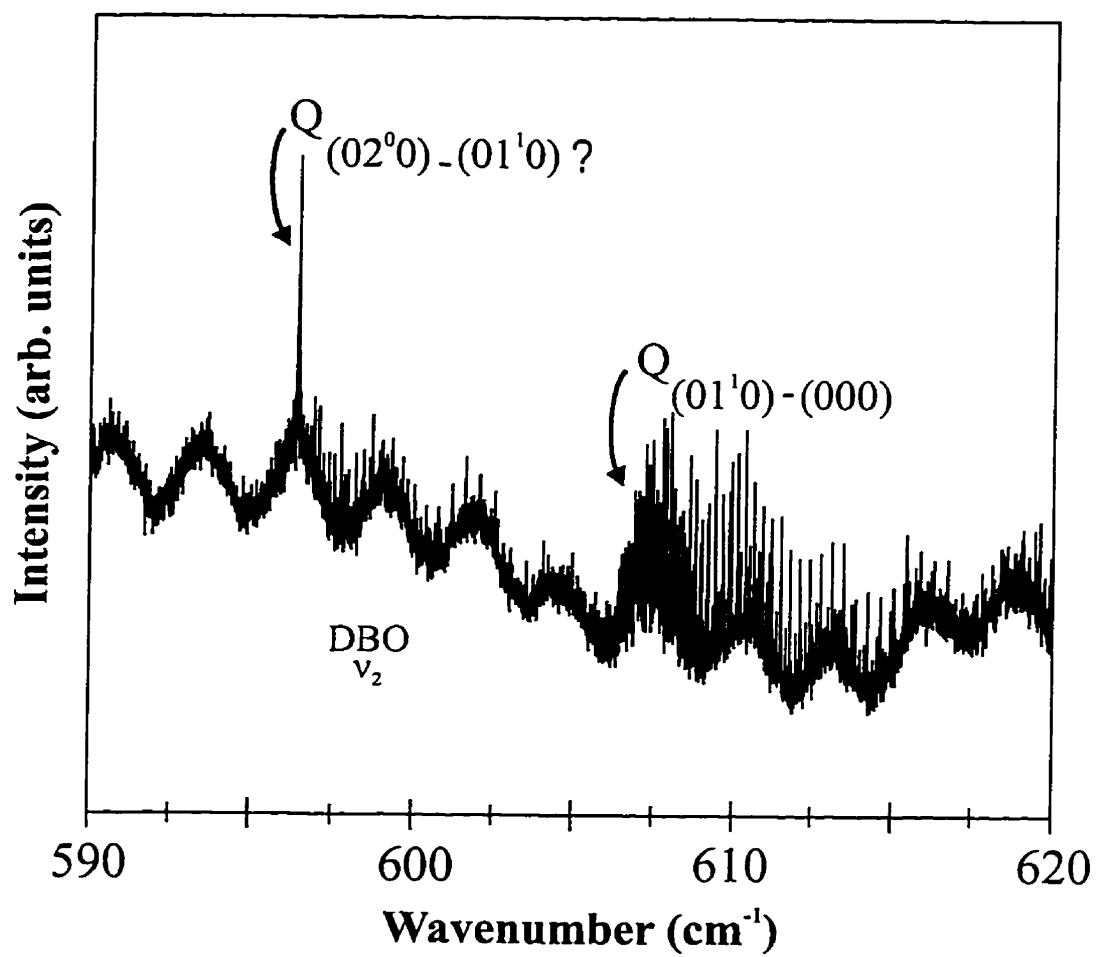
Figure 3.7: DBO spectrum between 590-620 cm^{-1} obtained with a helium-cooled Si:B detector (filter 1: 350-750 cm^{-1}).
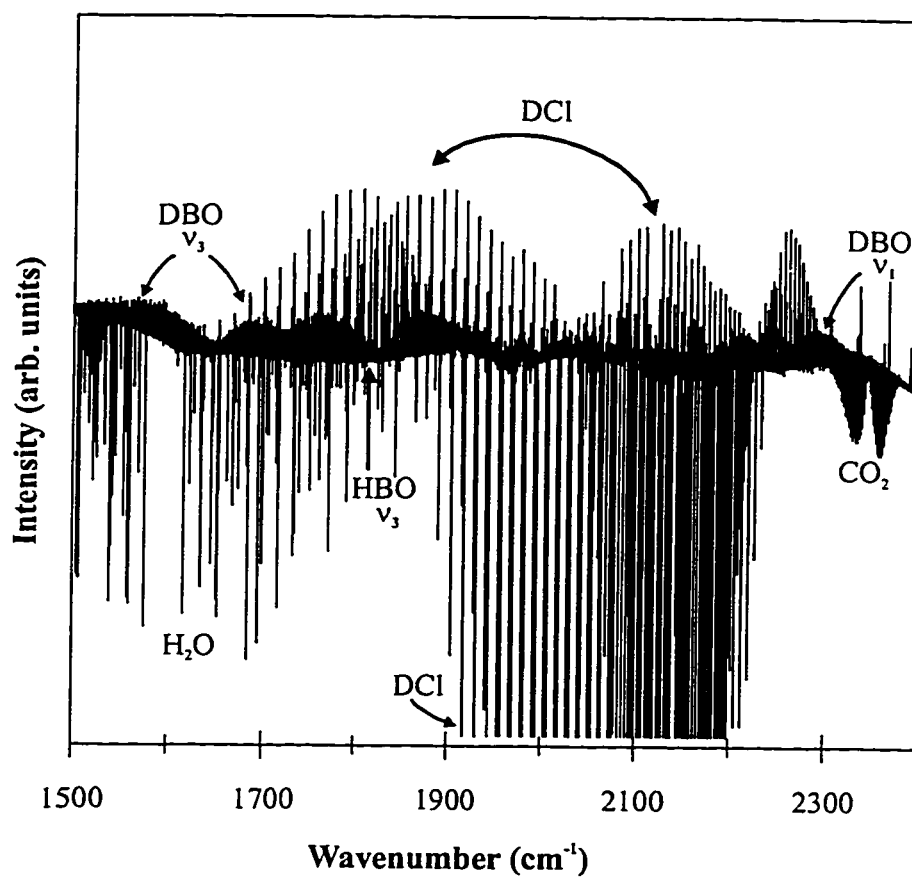
Figure 3.8: The spectrum obtained with a nitrogen-cooled InSb detector. DBO emission is observed between 1900 and 2000 cm^{-1} as well as between 2100 and 2350 cm^{-1}. HBO can also be seen between 1750 and 2000 cm^{-1}. H_2O, DCl, and CO_2 are also visible.

3.4 Chemistry

The origin of HBO in our experiment remains an open question. These experiments, at the very least, have led to informed speculation. It is unlikely that HBO is produced in the gas phase because the vaporization of boron is extremely endothermic, and requires temperatures in excess of 2700 °C in vacuum [54]. A likely scenario is that trace water in the system reacted with the surface of the hot boron metal to produce HBO. The process would parallel a similar reaction between boron and H_2S at 1000°C [55–57].

$$H_2O + B \rightarrow HBO?$$
$$H_2S + B \rightarrow HBS$$
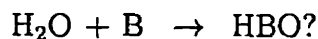
However, it is puzzling that when water was introduced into the tube, HBO was not produced in any significant quantity. It is possible that a large excess of water produces B_2O_3 instead. In addition, any trace of a chlorine-containing compound in the system reacted with the boron to yield BCl_3.

An interesting result is that no evidence of BO was observed in any of the experiments. This is in direct contrast with crossed-beam reactions between boron and water that are known to produce BO [44,58]. Furthermore, one matrix experiment mentioned in the last section showed evidence of both BO and HBO when boron was vaporized and then reacted with water [47]. The production of HBO in the high-temperature furnace, however, may reflect the differences between solid-phase and gas-phase reaction pathways. Factors such as the formation of oxide shells

around boron granules as well as the particle size and distribution in the solid are known to influence boron chemistry [44], and may favor the production of HBO over BO.

The spectra in Fig. 3.6 and 3.5 reveal CO in both emission and absorption. The CO signal is unusually strong in these spectra because the carbon boats used to hold the sample were oxidized to CO. The spectrum reveals that the CO was distributed throughout the tube. At the extreme ranges of the vibrational bands the rotational lines appear in emission, but they are seen in absorption for lower J. The high J lines arise from the hot molecules in the centre of the furnace while the cooler molecules at the ends of the tubes, which have lower J values, absorb the radiation emitted from the hot centre.

The impurities observed in the spectra also reveal that the ceramic tube is not an inert container, but may participate in the high-temperature chemistry. The SiO and AlCl observed in the first run originated from the walls of the mullite ($3Al_2O_3 \cdot SiO_2$) tube. In addition, the unidentified band at 804 cm^{-1} appeared at the same temperature as SiO and, like SiO, was not detected after the initial run. The features were partially resolved and resemble the vibrational-rotational band of a small polyatomic. It is interesting that a matrix experiment has reported an infrared band of Si_2O_2 at 805 cm^{-1} [47].

3.5 Spectroscopic Characterization of HBO

3.5.1 Outline of Vibrational-Rotational Motion

Since it is a closed-shell molecule, HBO does not possess electronic angular momentum, and the interpretation of the vibrational-rotational spectrum is based entirely on the nuclear degrees of freedom. The vibrational motion of HBO may be described by four normal modes, each of which corresponds to an irreducible representation in the point group $C_{\infty v}$. Two normal modes ν_1 and ν_3, transform as the symmetry species σ^+; these vibrations are essentially localized BH and BO stretches, respectively. The remaining ν_2 modes are degenerate bends in orthogonal planes and transform as π. The normal modes are illustrated in Fig. 3.9.

The vibrational levels for a linear triatomic molecules are denoted by (v_1, v_2, v_3). The fundamental vibrational transitions are given by:

$$
\begin{array}{ccc}
upper\ level & - & ground\ state \\
(\nu_1\nu_2\nu_3) & - & (\nu_1\nu_2\nu_3) \\
(100) & - & (000) \\
(010) & - & (000) \\
(001) & - & (000).
\end{array}
\tag{3.2}
$$

In Section 1.3.2, it was seen that a fundamental transition is allowed if it is described by the same irreducible representation as x, y or z. The z coordinate transforms as σ^+ and x, y transform as π in the $C_{\infty v}$ point group. Thus, all four fundamental
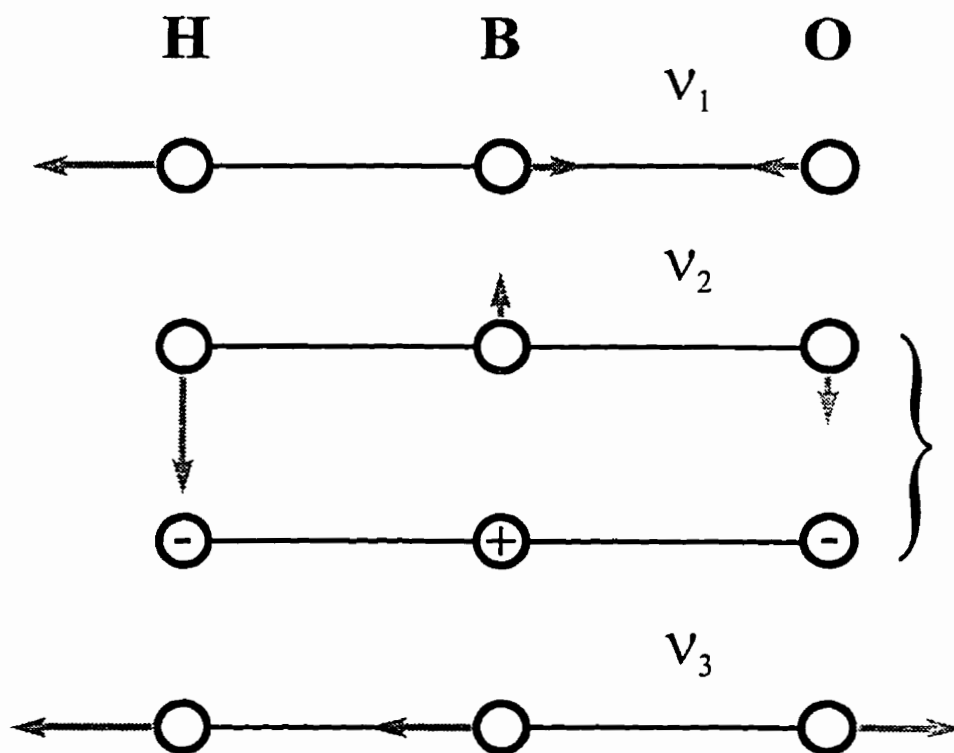
Figure 3.9: The normal modes of vibration of HBO. The + and - designate out of plane motions.

modes in HBO are predicted to be infrared active. Since the transition dipole moments of the two σ^+ fundamental vibrations have non-zero components along the z axis, they are known as parallel $\Sigma - \Sigma$ transitions. The rotational selection rules for a parallel transition in a linear molecule are $\Delta J = \pm 1$. An energy level diagram depicting the allowed rotational transitions is given in Fig. 3.10. The spectrum consists of two groups of vibrational-rotational lines, known as the P and R branches, that correspond to $\Delta J = -1$ and $\Delta J = 1$ transitions.

When the fundamental bending motion is excited, the transition dipole is oriented at right angles to the z axis, and the absorption or emission of a photon between the upper and lower levels is known as a perpendicular $\Pi - \Sigma$ transition. The rotational selection rules for a perpendicular transition are $\Delta J = 0, \pm 1$. The energy level diagram in Fig. 3.11 reveals that the spectrum will consist of P and R branches as well as a Q branch for the $\Delta J = 0$ transitions.

Overtone, combination, and hot bands may also appear in vibrational spectra. A particular band is electric-dipole allowed if the direct product of the symmetries of the upper and lower vibrational levels, $\Gamma(v') \otimes \Gamma(\hat{d}) \otimes \Gamma(v'')$, contains the totally symmetric representation of the point group (Section 1.3.4). The procedure is usually straightforward unless one or both of the levels are degenerate. In such cases, the symmetries of vth levels for degenerate modes can be evaluated using recursion relations [21]. The results for the π mode in the $C_{\infty v}$ point group are:

$$
\begin{aligned}
v \text{ even} \quad (\Pi)^v &= \Sigma^+ \oplus \Delta \oplus \Gamma \oplus \ldots \\
v \text{ odd} \quad (\Pi)^v &= \Pi \oplus \Phi \oplus \ldots
\end{aligned} \tag{3.3}
$$
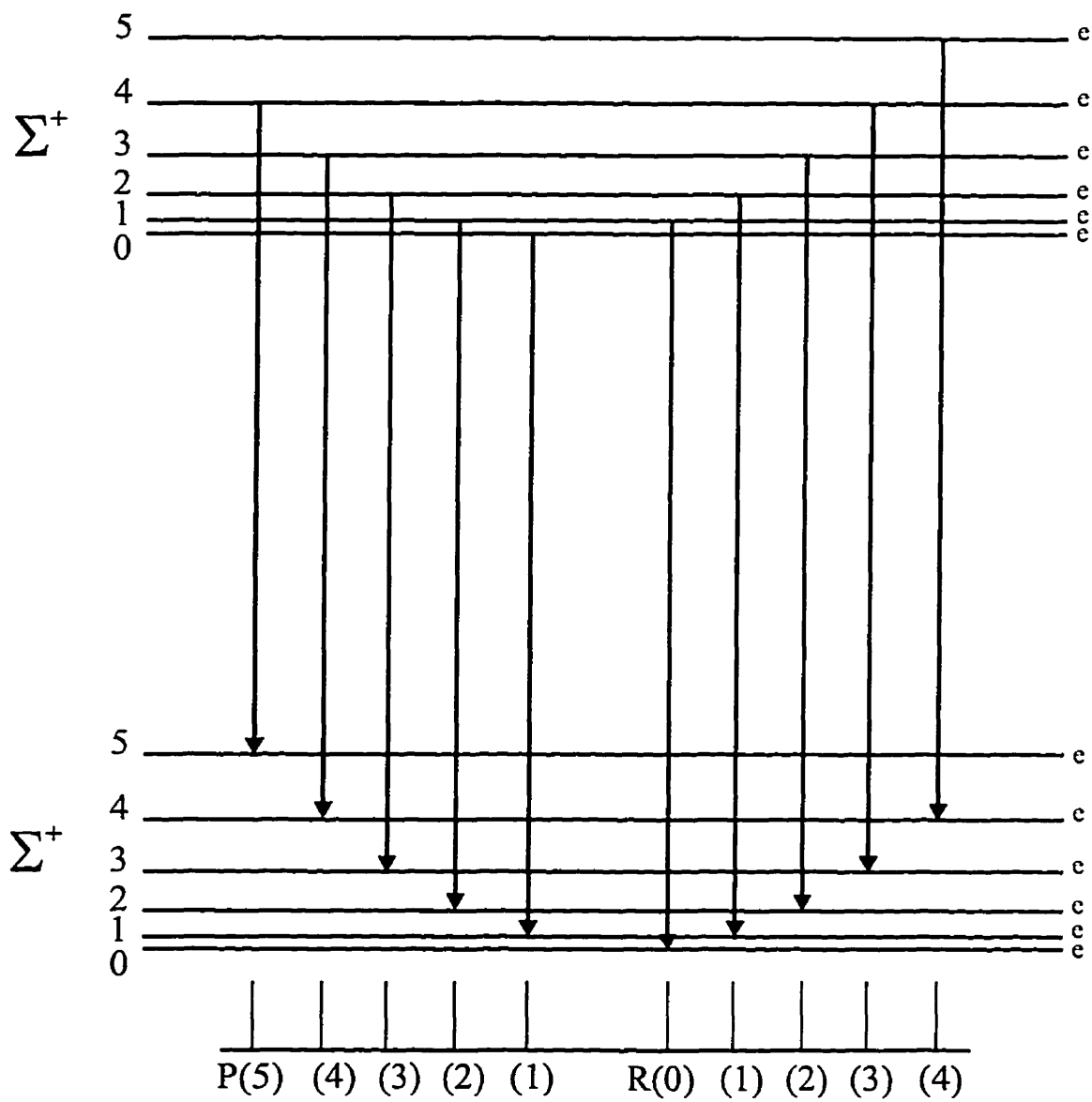
Figure 3.10: A parallel Σ^+—Σ^+ transition in a linear molecule [7].

Figure 3.11: A perpendicular Π—Σ transition in a linear molecule [7].

The Pauli exclusion principle forbids certain symmetries (in this case a Σ^- for even v) from appearing [32]. The vibrational energy levels associated with the bending motion in a linear triatomic are shown in Fig. 3.12.

The excitation of a degenerate vibrational mode leads to an angular momentum l about the molecular axis because the superposition of the motions resembles a rotation [2]. The angular momentum components for a level v are given by [15]:

$$l_i = v_i, v_i - 2, v_i - 4, ... - v_i \tag{3.4}$$

with $|l| = 0, 1, 2...$ designated $\Sigma, \Pi, \Delta....$ Levels with $v_2 \geq 1$, therefore, contain several vibrational sub-levels. Although the levels are degenerate within the harmonic approximation, anharmonicity causes the levels to lie slightly apart in energy [16]. Note that $J \geq |l|$ because the total angular momentum cannot be less than the projection of the angular momentum about the molecular axis.

Another property of the molecular wavefunction, the parity, must be introduced at this point because it places a further restriction on the selection rules for rotational-vibrational transitions. The total molecular wavefunction can be expressed as the product of the electronic, nuclear, and rotational contributions. Under inversion of the space-fixed coordinates, the entire Hamiltonian will remain unchanged except for a possible change in sign. The effect of the inversion operation $\hat{E}^*$ is represented by [32]:

$$\hat{E}^* \mid X_i, Y_i, Z_i \rangle = \pm \mid X_i, Y_i, Z_i \rangle. \tag{3.5}$$
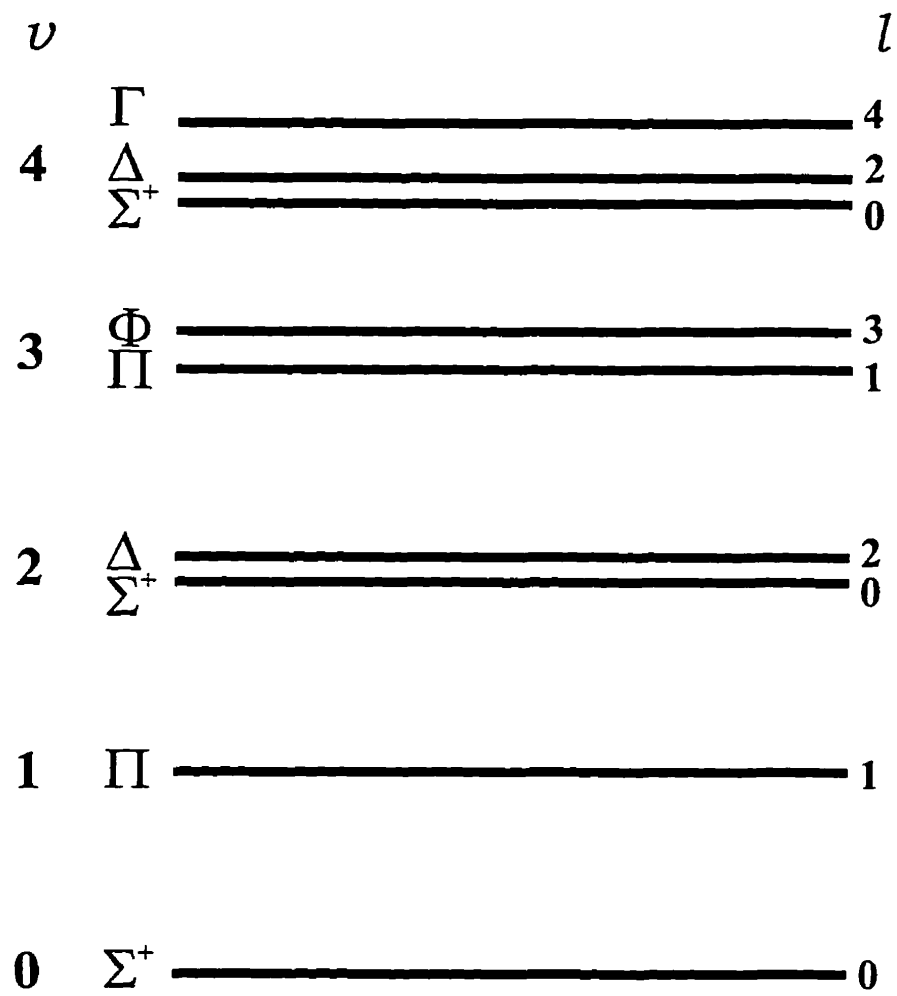
Figure 3.12: The energy levels associated with the π degenerate mode in HBO.

The eigenvalue of this equation, designated the parity, equals 1 or -1 (+ or -). Electric dipole transitions obey the selection rule + ↔ -. Furthermore, since the total wavefunction must remain unchanged except for the sign, the rotational, vibrational, and electronic contributions also can be classified according to their parity. The electronic ground state of HBO is totally symmetric. For linear molecules in a $^1\Sigma$ electronic ground state, a convenient labelling scheme exists that is based on the parity of the rotational wavefunction [59]:

$$\tilde{E}^* \mid r\rangle = (-1)^J \mid r\rangle. \tag{3.6}$$

If this alternation with J is removed from the total parity, then the remaining parity is labelled by e or f. The states with $+(-1)^J$ are designated e while those with $-(-1)^J$ are labelled f. The parity selection rule + ↔ - becomes:

$$e \quad \leftrightarrow \quad f \quad \text{for } \Delta J = 0 \text{ (Q branch)}$$
$$e \quad \leftrightarrow \quad e, \ f \leftrightarrow f \quad \text{for } \Delta J = \pm 1 \text{ (P and R branches)} \tag{3.7}$$

In a Σ^+ vibrational level, all of the rotational levels are e. In a doubly degenerate level such as Π, however, each rotational level contains a pair of e and f levels.

When the molecule begins to rotate, the e and f components in a doubly degenerate level within a vibrational multiplet will exhibit a splitting known as l-type doubling. The physical interpretation of this effect is based on the Coriolis interaction [20]. An important example is the l-type doubling exhibited by the e and f components of the Π (01^10) level. The Coriolis force causes a slight change in effec-

tive moment of inertia depending on whether the bending motion is perpendicular or parallel to the axis of rotation. The vibrational-rotational interaction splits the degenerate levels, giving rise to the l-type doubling. It has been shown that the levels within a vibrational multiplet will exhibit l-doubling interaction as long as they are related by $\Delta l = \pm 2$ [60,61], treating l as a signed quantum number. Note that l-type doubling is known as l-type resonance when the two interacting levels belong to different vibrational symmetries. One example of l-type resonance is the interaction between the $\Sigma^+(l = 0)$ and $\Delta(l = \pm 2)$ levels of the $v_2 = 2$ state in a linear molecule.

The influence of l-type doubling and resonance on the vibrational-rotational energy levels can be determined by the solution of a secular determinant of dimension $(v_2 + 1)$ [61]. The diagonal terms correspond to the unperturbed rigid-rotor, harmonic oscillator matrix elements and the off-diagonal elements are the l doubling terms connecting the levels that differ by $\Delta l = \pm 2$. To illustrate, the important example of l-type doubling seen in the Π ($\Delta l = \pm 1$) $(01^1 0)$ level of a linear triatomic will be considered. The energies for the state can be obtained from the secular determinant [61]:

$$\begin{vmatrix} E_\Pi^0 - \epsilon & \frac{1}{2}W_{11} \\ \frac{1}{2}W_{11} & E_\Pi^0 - \epsilon \end{vmatrix} = 0, \qquad (3.8)$$

E_Π^0 is the unperturbed energy of the $(01^1 0)$ state and $W_{11} = q_v J(J+1)$. The solutions are:

$$E_+ = E_\Pi^0 + \left(\frac{q_i}{2}\right) J(J+1)$$

$$E_- = E_\Pi^0 - \left(\frac{q_i}{2}\right) J(J+1) \qquad (3.9)$$

Thus, in the analysis of molecular spectra the energy level expressions for rotational motion must be modified to include this type of interaction. In a similar fashion, it is possible to solve the secular determinants for higher v [60, 62, 63].

Two commonly observed hot bands in linear triatomic hydrides, the $(01^1 1)$—$(01^1 0)$ and $(11^1 0)$—$(01^1 0)$ transitions, demonstrate how the selection rules, parity, and l-type resonance are expressed in molecular spectra. For example, the π bend in linear triatomic hydrides is low in energy and hot bands involving the excited levels of this mode are often observed. The energy level diagram for these Π—Π transitions is given in Fig. 3.13. The spectrum of a transition with $\Delta l = 0$, $l \neq 0$ consists of P, Q, and R branches. The rotational lines are doubled because the degeneracy of the sub-levels is lifted under rotation through l-doubling. For the P and R branches the transitions obey the selection rules $e \leftrightarrow e$ and $f \leftrightarrow f$. The Q branch connects the $f \leftrightarrow e$ and $e \leftrightarrow f$ levels; it is weak for Π—Π transitions because $\Delta l = 0$ [3]. General considerations such as these recur in the molecular vibrational-rotational spectra of linear molecules, as shortly will be seen for the HBO results.

3.5.2 Results and Analysis

Gas-phase HBO had been previously observed in the infrared by Kawashima and co-workers, who used a diode laser spectrometer to measure 6 P and 12 R lines of the (001)-(000) fundamental band [49]. The work reported here extends the infrared data set considerably, to all of the fundamental transitions and to several hot bands for both $H^{11}BO$ and $H^{10}BO$. For DBO, some preliminary diode work was carried
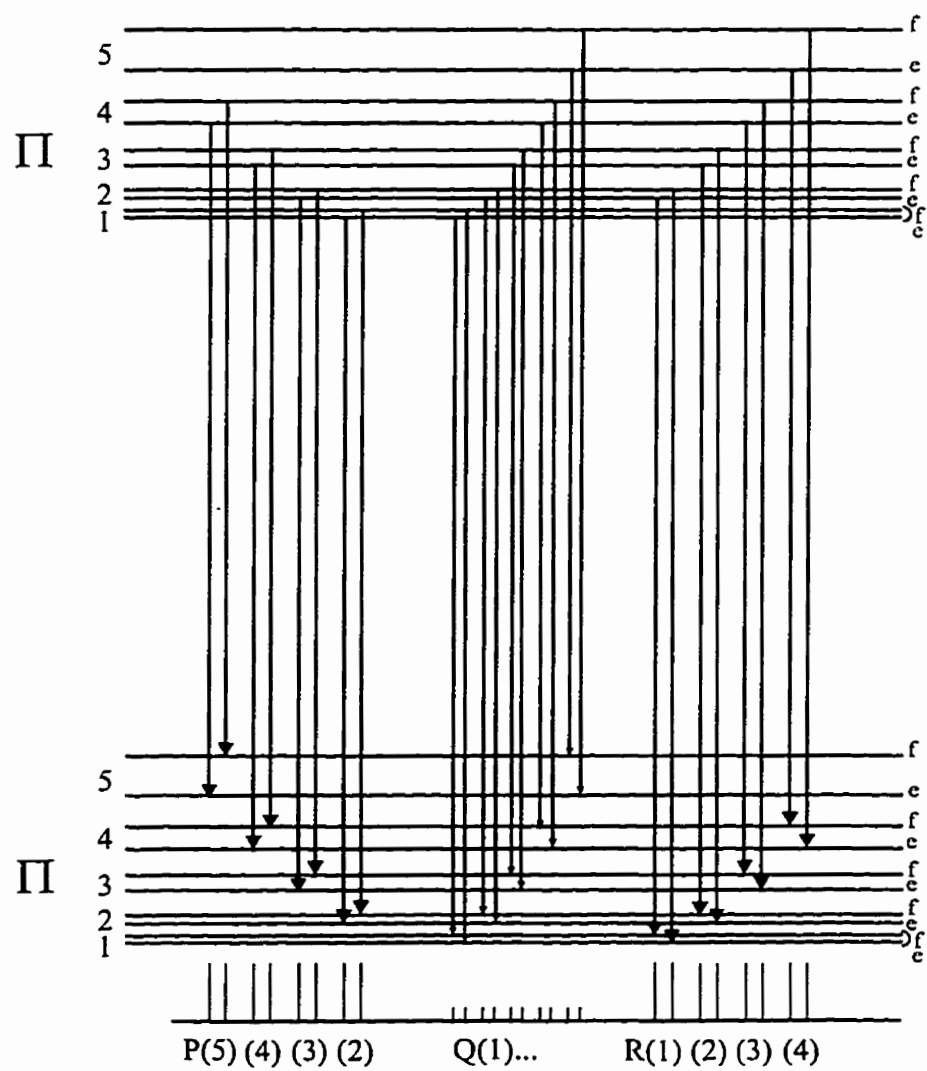
Figure 3.13: A Π—Π transition in a linear molecule [7].

out by Kawashima in 1989 [64], but the results remained unpublished because the assignments were tentative. The present infrared emission measurements have led to the unambiguous identification of all three fundamental bands as well as one hot band for $D^{11}BO$, and the (001)-(000) fundamental for $D^{10}BO$.

Vibrational transitions for the two naturally-occurring boron isotopomers (^{11}B 80.2% and ^{10}B 19.8% [65]) of HBO and DBO were observed. The rotational line widths at half maximum were approximately 0.01 cm^{-1} in both sets of spectra. The line positions were measured using PC-DECOMP, a freely distributed program that was developed by Jim Brault while he was at the National Solar Observatory. The program allows the user to select peaks in a spectrum, which then can be fitted to a spectral lineshape function. For high-temperature species, the spectral lineshape of a rotational line is influenced by both homogeneous and inhomogeneous effects, primarily from pressure and Doppler broadening, respectively. To account for both types of contributions, the line profiles were fit to a Voigt lineshape function, which is a convolution of Gaussian and Lorentzian lineshapes [66].

In the next step, the list of line positions was organized into different series using an in-house program based on the Loomis-Wood technique [18]. The different series were then assigned to the appropriate vibrational transition according to the methods described in the next section.

HBO

The vibrational transitions that were assigned and analyzed for $H^{11}BO$ and $H^{10}BO$ are listed in Tables 3.2 and 3.3.

Table 3.2: Assigned transitions for $H^{11}BO$

(Upper)	—	(Lower)	(Upper)	—	(Lower)
(100)	—	(000)	(02^20)	—	$(01^10)^*$
(01^10)	—	(000)	(01^11)	—	(01^10)
(001)	—	(000)	(11^10)	—	(01^10)
(002)	—	(001)	(01^12)	—	$(01^11)^*$
(02^00)	—	$(01^10)^*$			

*These transitions were not included in the global fit.

Table 3.3: Assigned transitions for $H^{10}BO$

(Upper)	—	(Lower)	(Upper)	—	(Lower)
(100)	—	(000)	(001)	—	(000)
(01^10)	—	(000)	(01^11)	—	(01^10)

Most of the vibrational-rotational bands were analyzed based on the conventional energy expressions for the rotational-vibrational energy levels of linear molecules [15]:

(i) Σ:

$$
\begin{aligned}
E(v, J) &= \nu_0 + B_v[J(J+1) - l^2] - D_v[J(J+1) - l^2]^2 \\
&+ H_v[J(J+1) - l^2]^3 + \ldots,
\end{aligned} \tag{3.10}
$$

(ii) Π:

$$
\begin{aligned}
E(v, J) &= \nu_0 + B_v[J(J+1) - l^2] - D_v[J(J+1) - l^2]^2 \\
&+ H_v[J(J+1) - l^2]^3 + \ldots \\
&\pm \frac{1}{2}[q_v J(J+1) + q_D J^2(J+1)^2 + q_H J^3(J+1)^3 + \ldots]. \quad (3.11)
\end{aligned}
$$

Note that $l=0$ for a Σ state and $l=1$ for a Π state. The q_i in Eq. (3.9) have been replaced by a series expansion in $J(J+1)$ with the coefficients $q_v, q_D, q_H \ldots$. These higher-order corrections to the l-doubling constant sometimes are required for satisfactory agreement of the observed line positions [15].

For the $v_2=2$ multiplet, the analysis was more complicated because the Σ^+ and Δ levels interact through an l-type resonance (see Fig. 3.12). A secular determinant of dimension $v_2 + 1 = 3$ must be solved in a procedure similar to that outlined for the $v_2=1$ Π level. The energy expressions that result are [60, 61]:

$$
\begin{aligned}
E_\Sigma^e &= E_\Sigma^0 + \tfrac{1}{2}\delta + \tfrac{1}{2}\sqrt{\delta^2 + 4q_v^2[J^2(J+1)^2 - 2J(J+1)^2]} \\
E_\Delta^f &= E_\Delta^0 \\
E_\Delta^e &= E_\Delta^0 - \tfrac{1}{2}\delta - \tfrac{1}{2}\sqrt{\delta^2 + 4q_v^2[J^2(J+1)^2 - 2J(J+1)^2]}, \quad (3.12)
\end{aligned}
$$

where δ is the energy separation between the unperturbed levels, $E_\Delta^0 - E_\Sigma^0$. The energy expressions reveal that the two e levels will interact while the f level is unaffected.

In the initial stages of analysis, a tentative band origin was selected and the

J-numbering was based on the method of combination differences:

$$R(J) - P(J) = 4B' \left(J + \tfrac{1}{2} \right) \quad \text{upper levels} \qquad (3.13)$$

$$R(J-1) - P(J+1) = 4B'' \left(J + \tfrac{1}{2} \right) \quad \text{lower levels.} \qquad (3.14)$$

Once a consistent J-numbering was assigned, an in-house program was used to fit the line positions to the energy differences between the upper and lower vibrational levels. The least squares procedure was weighted according to the signal-to-noise ratio; within a given vibrational band, the blended lines were accorded the lowest weight. When the J-numbering was correct, the fits showed a clear minimized variance. Terms higher than $[J(J+1)]^2$ were included when the associated parameters were determined with an error of no more than 30%, as long as their inclusion caused a drop in the variance.

The variation of the B values over the vibrational levels in a linear molecule was also used to check the assignments:

$$B_v = B_e - \alpha_1(v_1 + \tfrac{1}{2}) - \alpha_2(v_2 + 1) - \alpha_3(v_3 + \tfrac{1}{2}) \qquad (3.15)$$

The B_e and α values are shown in Table 3.4 for both isotopomers. For the stretching vibrations, the α's are positive, which implies that the moments of inertia are slightly larger in the excited Σ levels. The negative α value for the bending mode, however, has the opposite behavior. Both these observations are typical for linear triatomic hydrides [14].

Table 3.4: The B_e and α values for $H^{11}BO$ and $H^{10}BO$. All units in are reported in cm^{-1}. The uncertainties in the parentheses correspond to 3σ from the fit.

	B_e	$\alpha_1(100)$	$\alpha_2(01^10)$	$\alpha_3(001)$
$HB^{11}BO$	1.31408(7)	0.00892(6)	-0.00310(9)	0.00867(3)
$HB^{10}BO$	1.35963(4)	0.01001(5)	-0.00334(5)	0.00900(4)

As a final check, the constants for the (000), (100), (01^10), and (001) levels were used to predict microwave line positions that had appeared in the literature for both $H^{11}BO$ and $H^{10}BO$ [49]. The rotational-vibrational lines from the vibrational bands (see Table 3.2) as well as literature microwave lines were then combined in global fits for $H^{11}BO$ and $H^{10}BO$. All of the fitted parameters, including the band origins, as well as the rotational, centrifugal and l-doubling constants are listed in Tables 3.5 and 3.6. The line position tables are reported in Appendix A.

The two fundamental vibrational transitions, (100)—(000) and (001)—(000), primarily correspond to the BH and BO stretches, respectively. Both are $\Sigma - \Sigma$ (parallel) transitions and exhibit a double-lobed PR structure with no Q branch. The assignment of these bands for the main isotopomer $H^{11}BO$ was straightforward because they contained the most intense series of rotational lines in the ν_1 and ν_3 wavenumber regions. The isotopic bands were detected by comparing spectra recorded at different temperatures (T=1000°C and T=1400°C) because the relative

Table 3.5: The effective constants for $H^{11}BO$. All units are reported in cm^{-1}. The uncertainties in the parentheses correspond to 3σ from the fit.

(v_1, v_2, v_3)	ν_0	B_v q_v	$D_v\ 10^6$ q_D	$H_v\ 10^{12}$ $q_H\ 10^8$
(000)		1.308379965(94)	2.67689(44)	2.43(14)
(100)	2794.17977(12)	1.29938022(35)	2.64456(46)	2.3(13)
(01^10)	754.41526(11)	1.311374230(80) -.00607121(16)	2.73138(46) 5.867(56)	3.02(14) -1.3(20)
(001)	1825.560711(49)	1.29973259(11)	2.6714(48)	2.77(16)
(01^11)	2583.46438(14)	1.3026666(29) -.00626404(39)	2.72027(56) 4.972(71)	3.66(17) -1.88(24)
(11^10)	3532.19563(25)	1.3025274(10) -.0060687(12)	2.7032(12) 6.08(18)	3.15(34) -1.94(55)
(002)	3634.94796(16)	1.29108292(56)	2.66307(68)	3.29(20)

Table 3.6: The effective constants for $H^{10}BO$. All units in are reported in cm^{-1}. The uncertainties in the parentheses correspond to 3σ from the fit.

(v_1, v_2, v_3)	ν_0	B_v q_v	$D_v\ 10^6$ $q_D\ 10^8$
(000)		1.35344977(10)	2.84953E-06(91)
(100)	2817.72254(24)	1.3434587(14)	2.81415E-06(89)
(01^10)	763.62569(23)	1.356836111(78) -.00641693(16)	2.9074E-06(19) 5.25E-08(37)
(001)	1864.16206(15)	1.34448601(13)	2.84225E-06(97)
(01^11)	2632.38128(32)	1.34779064(40) -.00666607(55)	2.8919E-06(19) 3.87E-08(39)

intensities between the $H^{11}BO$ and $H^{10}BO$ bands remained the same.

Overviews of the ν_1 and ν_2 regions of the spectrum are given in Figs. 3.5 and 3.6. From a comparison of the ν_3 R branch to the ν_1 fundamental band recorded with the InSb detector (Fig. 3.6), the relative intensity of ν_3:ν_1 is estimated to be about 30:1. An interesting point is that the (100)-(000) infrared transition had never been observed before this work. Although the signal was quite weak when compared to the (001)-(000) band, the emission technique yielded a good signal-to-noise ratio, allowing the detection of the minor isotopomer as well. A detail of the spectrum is depicted in Fig. 3.14. This observation underlines the sensitivity of the Fourier transform emission technique for high-temperature species.

Inspection of the VEEL4 database reveals that there are characteristic BH and
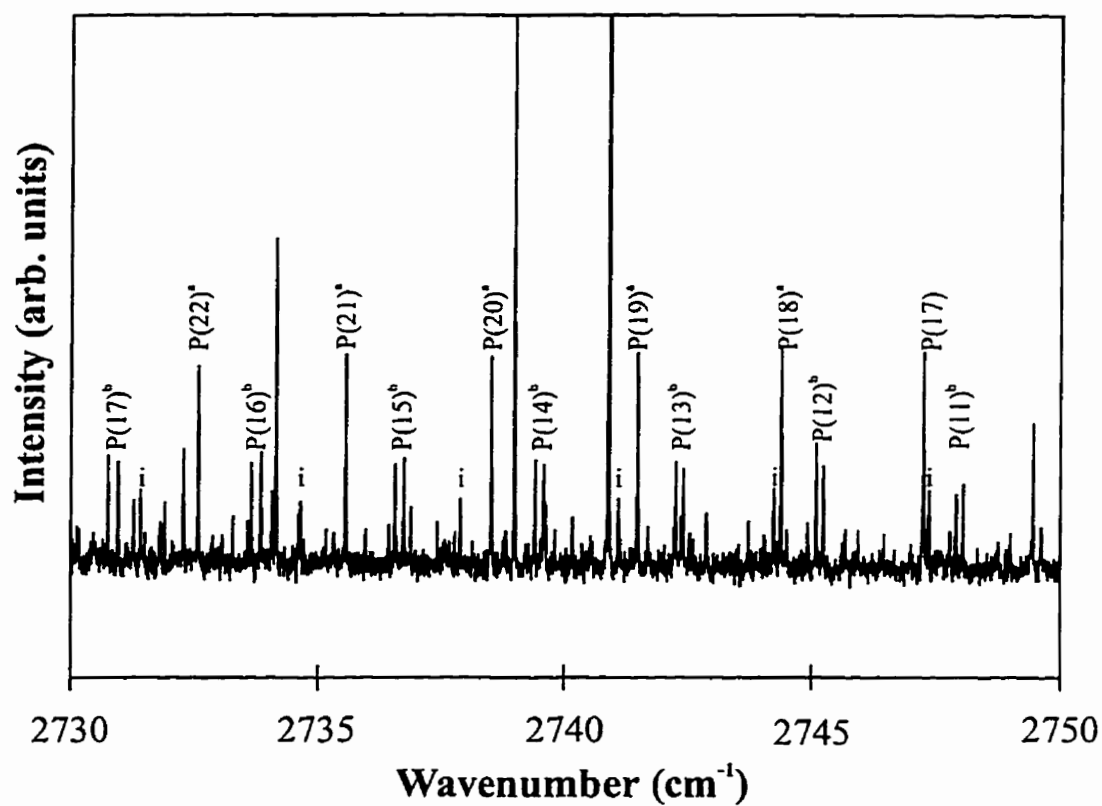
Figure 3.14: A detail of the $H^{11}BO$ spectrum in the ν_1 region. [a]The (100)—(000) series; [b]The e—e and f—f components of the (11^10)-(01^10) transition. The line positions of the (100)—(000) transition of the minor $H^{10}BO$ isotopomer are labelled i.

Table 3.7: BH Stretching Vibrations in Various Polyatomic Transient Molecules [36].

Molecule	BH Stretch (cm^{-1})
HBO	2794
HBS	2736
$HBCl_2$	2617
HBF_2	2621
HBBH	2680
HBCH	2725
H_2CBH_2	2561

BO frequencies for transient molecules [36]. Tables 3.7 and 3.8 list typical examples. The approximate wavenumber ranges are 2500-2800 cm^{-1} for BH and 1900-2100 cm^{-1} for BO. For qualitative assignments, the BH region is useful because it is relatively uncluttered. The BO group, in contrast, lies in the same region as other functional group wavenumbers such as the CH stretch [36].

The (01^10)—(000) fundamental band is associated with a change from a Π to a Σ^+ vibrational level; this type of transition yields a strong Q branch, as was indeed observed. Fig. 3.3 portrays the spectrum in the bending region. The upper π level contains degenerate e and f sub-levels that split with increasing rotation. Since the Σ^+ levels have e parity, the P and R branches correspond to only $e - e$ transitions. For the Q branch, however, the selection rule $e \leftrightarrow f$ allows the transitions from

Table 3.8: BO Stretching Vibrations in Various Polyatomic Transient Molecules [36].

Molecule	BH Stretch (cm^{-1})
HBO	1826
ClBO	1958
$BrBO_3$	1937
$OBSO_2$	2006
FBO_2	2078
HOBO	2023

the f components in the upper level to the e components in the ground level. In general, the rotational and centrifugal constants are not identical for the e and f levels; thus, the reported parameters represent an averaged value of both sub-states.

Several hot bands were observed in the spectra of HBO. An intense series of HBO lines was assigned to the (01^11)—(01^10) Π—Π sequence band. Since the transition occurs between two doubly degenerate levels, l-type doubling occurs for each P and R branch transition. Q branches for Π—Π transitions tend to be weak, and indeed none was observed for this band. The (01^11)—(01^10) transition was also identified for the minor $H^{10}BO$ isotopomer. In the ν_1 stretching region, (11^10)—(01^10) was observed only for the main isotopomer. A detail of the spectrum is shown in Fig. 3.14. Note that the doubled P branch lines associated with the sequence band are clearly visible.

Another hot band, the (01^12)—(01^11) transition, was also tentatively identified, but was not included in the global fit. On the basis of the α parameters, the B_v

Table 3.9: The parameters for the (01^12) level (tentative) obtained from a (01^12)—(01^11) fit. All units are reported in cm^{-1} and the 3σ are reported in parentheses.

ν_0	4396.31814(15)
B'_v	1.293962(39)
D'_v 10^6	2.6917(16)
q'_v	-.0064699(77)
q'_D 10^8	2.80(32)

constant for this state is estimated to be 1.2941 cm^{-1}. The value is close to the B_v rotational constant of 1.293962 cm^{-1} obtained from fitting the band to a (01^12)—(01^11) transition. The fitted parameters are listed in Table 3.9 and the line positions may be found in Appendix A.

Hot bands involving the levels in the $v_2=2$ multiplet were also observed. The analysis of these bands is more complicated because the (020) multiplet contains Σ and Δ levels that interact through an l-type resonance. The $(02^00) - (01^10)$ transition was relatively simple to assign because it exhibited a strong Q branch, which is usually seen for $\Sigma - \Pi$ transitions (see Fig. 3.3). The series was picked out to relatively high J, but when a $\Sigma - \Pi$ fit was attempted with constrained constants for the lower level, the variance was on the order of 10000. The poor fit was not unexpected because the e levels in the Σ state are perturbed by the e levels in the neighboring Δ state. Since the l-type resonance is proportional to the square of the angular momentum $J(J+1)$, the results were examined for a dependence on J. As expected, the fit was relatively good for $J < 20$, with a variance below 5. The D value for the (02^00) state, however, was much higher than for the values obtained for

the $(01^1 0)$ and (000) states. Generally, the value would be expected to be similar to the ground state value, except for a small correction [15]. In the low-J fit, however, the value for D was almost double the ground state value. The anomalously large D value is consistent with a deviation from the predicted energies that worsens with increasing angular momentum, as would be expected for a Coriolis interaction [18].

The search for the $(02^2 0)$—$(01^1 0)$ transition was more challenging. For levels with high l, the low J lines are missing because $J \geq |l|$. Thus, for a Δ—Π transition, the absent $R(0), P(1)$ and $P(2)$ lines lead to a considerable gap between the P and R branches. With the lack of strong Q branches, linking the appropriate P and R branches is somewhat difficult. At this point, the microwave results of Kawashima et $al.$ were used to search for the missing state [49]. The three sets of transitions from the Δ_f, Δ_e, and Σ_e^+ levels to the common lower $(01^1 0)$ Π level were fit separately to Σ—Π transitions in order to obtain effective constants. In turn, these effective constants were used to predict combination differences for the infrared line positions. Although the combination differences matched several candidate series, the published value for the separation between the $(02^2 0)$ and $(02^0 0)$ levels, $\delta = E_\Delta^o - E_\Sigma^o$, was not consistent with any of them. Indeed, a rough estimate for δ suggested that the microwave result might be off by 10 cm^{-1}. When the value was used to predict the microwave line positions listed in the same report, the results were not consistent. The value of δ was iterated, and it was found that the best match to the microwave data was achieved with a value of approximately 20 cm^{-1}.

In next stage of analysis, the most intense band that matched the predicted

combination differences was selected and fit to a $(02^{2,f}0)$ $(\Delta_f—\Pi)$ transition. The f components of the (02^20) level are not affected by l-type resonance, as predicted by Eq. (3.12). The minimized variance as well the α values were consistent with a band origin at about 1513 cm^{-1}, which further indicated that $\delta \approx 20$ cm^{-1} for the the $v_2 = 2$ multiplet. To identify $(02^{2,e}0)—(01^10)$ transition, the effective constants based on the microwave lines as well as the band origin obtained for the $f - f$ fit were used to predict the line positions. One likely series was identified immediately, and exhibited a similar perturbation as the $(02^00)—(01^10)$ transition, which is consistent with solutions of the secular determinant given in Eq. (3.12).

The data for the Σ and Δ states were combined in a nonlinear fit using Eq. (3.12). The constants for the (01^10) Π lower vibrational level were fixed, and the fit was carried out according to the energy expressions given in Eqs. (3.12). The residuals were reasonably random, although a slight systematic effect could still be observed in the Σ^+ level residuals. No model is perfect, and in this case, there could have been a slight contribution from higher-order interactions that connect states that differ by $\Delta l = \pm 4$, as has been observed for HCN [61]. Although the energy expressions were modified to account for $\Delta l = \pm 4$ interactions, following the HCN example, there was no improvement in the quality of the fits. The results of the final fits are given in Table 3.10, and the line positions are found in Appendix A. It is seen that the separation between the Σ^+ and Δ levels is 22.18524(55) cm^{-1}.

Table 3.10: The effective constants for the (02^00) Σ^+ and (02^20) Δ levels. The labels $v1$ and $v2$ refer to the Σ^+ and Δ levels, respectively. All units are reported in cm^{-1} and the 3σ uncertainties are reported in parentheses.

ν_0	1490.81055(44)
δ	22.18524(55)
B_{v1}	1.314148(20)
D_{v1}	2.7788E-06(26)
H_{v1}	3.05E-12(93)
B_{v2}	1.3145064(21)
D_{v2}	2.8103E-06(22)
H_{v2}	6.48E-12(81)
q_v	-.0070481(28)
q_D	-1.754E-07(21)

3.5.3 DBO

For DBO, the (001)-(000) and (01^10)—(000) transitions were identified and fit according to the procedure followed for HBO. It was readily apparent, however, that the (100) level was perturbed in DBO because the (100)—(000) band was much more intense that the corresponding one in HBO (see Fig. 3.6 and Fig. 3.8). Indeed, when a fit of the (100)—(000) transition was attempted, the results showed a perturbation that increased rapidly with J. These observations corroborated the work of Kawashima *et al.*, who attributed the perturbation to a Coriolis interaction between the (100) and (01^11) vibrational levels [64]. The results were confirmed when the (01^11)—(01^10) sequence band also deviated from the conventional energy expression.

Like for *l*-type doubling and *l*-type resonance, the Coriolis interaction is treated

by solving a secular determinant that contains off-diagonal elements connecting the two interacting vibrational states. The matrix elements are [4]:

$$\langle v_s, v_t, l, J \mid H_{\text{cor}} \mid v_s + 1, v_t - 1, l \pm 1, \pm J \rangle$$
$$= -iB_e \zeta_{stl}^y \sqrt{\frac{\omega_t}{\omega_s}} + \frac{1}{2}\sqrt{\left(\frac{\omega_s}{\omega_t}\right)} (v_s + 1)(v_t \pm 1)(J \mp 1)(J \pm l + 1); \quad (3.16)$$

$$\langle v_s, v_t, l, J \mid H_{\text{cor}} \mid v_s - 1, v_t + 1, l \pm 1, \pm J \rangle$$
$$= iB_e \zeta_{stl}^y \sqrt{\frac{\omega_t}{\omega_s}} + \frac{1}{2}\sqrt{\left(\frac{\omega_s}{\omega_t}\right)} v_s(v_t \pm l + 2)(J \mp 1)(J \pm l + 1). \quad (3.17)$$

The ω_t and ω_s are the wavenumbers of each vibration, the B_e is the rotational constant at equilibrium, and ζ_{stl} is the Coriolis coupling constant for the two levels.

The energy expression that describes the Coriolis interaction has the following form:

$$\Delta^2 = \delta^2 + 4J(J + 1)W_{Cor}^2 \quad (3.18)$$

where Δ and δ are the energy separations between the perturbed and unperturbed states, respectively. The W_{Cor} is the Coriolis interaction term, $B_e\zeta_{stl}(\sqrt{\frac{\omega_t}{\omega_s}} + \sqrt{\frac{\omega_s}{\omega_t}})$. A nonlinear least-squares fit was carried out to determine the vibrational energies, the Coriolis interaction term as well as the constants B, D, q_v, and q_D. A Coriolis interaction was also observed in the (100)—(000) band for $D^{10}BO$; since the (01^11)—(000) transition could not be detected, the constants for the (01^10) level were constrained. The results are summarized in Tables 3.11 and 3.12, and the line positions are listed in Appendix C and D.

Table 3.11: The effective constants for $D^{11}BO$. All units are reported in cm^{-1}. The uncertainties in the parentheses correspond to 3σ from the fit. The ζ_{Cor} is the Coriolis coupling coefficient between the (100) and (01^10) levels.

(v_1, v_2, v_3)	ν_0	B_v q_v	D_v 10^6 q_D 10^8	H_v 10^{12}
(000)		1.0488444(17)	1.7167(53)	2.4(16)
(100)	2253.52303(65)	1.039592	1.708(11)	2.9(20)
(01^10)	608.42(14)	1.0520397(14) $-0.0048082(27)$	1.7706(63) $-3.71(30)$	3.6(21)
(001)	1647.6872(62)	1.0435879(17)	1.7107(49)	2.3(15)
(011)	2263.01(14)	1.046723(27) $-0.004939(52)$	1.7579(70) $-3.70(72)$	3.2(19)
ζ_{Cor}	0.1106(16)			

Table 3.12: The effective constants for $D^{10}BO$. The constants for the (01^11) level are assumed. All units are reported in cm^{-1}. The uncertainties in the parentheses correspond to 3σ from the fit. The ζ_{Cor} is the Coriolis coupling coefficient between the (100) and (01^10) levels.

(v_1, v_2, v_3)	ν_0	B_v q_v	D_v 10^6 q_d 10^8	H_v 10^{12}
(000)		$1.0721147(50)$	$1.779(14)$	$-7.4(45)$
(100)	2305.0290	1.0622320	1.5942620	4.4035790
(01^11)	2280^a	1.07023952^a	1.802^a	-0.00493271^a
ζ_{Cor}	$0.14297\,(43)$			

^{a}assumed.

3.6 Conclusion

HBO was generated in a ceramic furnace at temperatures above 800°C. Although the exact chemistry of the reaction has not been elucidated, it is likely that trace water reacted with solid boron to produce HBO, in analogy to the formation of HBS from boron and H_2S. The results indicate that HBO may be an important intermediate in the boron oxidation. It was also shown that DBO could be produced by reacting deuterium with the parent molecule.

The major focus of the project, however, was a characterization of the rotational-vibrational spectra of HBO and DBO. It is seen that Fourier transform infrared emission spectroscopy is a sensitive technique for studying transient molecules. Indeed the weak (100)—(000) fundamental transition in HBO had not been observed

before this work.

In high-resolution spectroscopy, precise models of molecular motion are required to account for the pattern of the rotational-vibrational positions. Small shifts in rotational energies from the predicted energies are noted and explained. Sections 1.3.1 and 1.3.2 introduced several examples of higher-order effects, including centrifugal distortion and the Coriolis force, that have been considered in the analysis of the isotopomers of HBO.

The three fundamental vibrational bands as well as various hot bands have been observed and analyzed for $H^{11}BO$, $H^{10}BO$, and $D^{11}BO$, while the (100)—(000) band was observed for $D^{10}BO$. A strong Coriolis interaction between the (100) and (01^10) vibrational levels in both deuterated species was observed and analyzed.

Chapter 4

The Infrared Emission Spectra of Uracil, Thymine, and Adenine

4.1 Overview

This chapter describes the application of infrared spectroscopy to the study of a class of biological molecules, the nucleic acid bases. What is somewhat unusual is that these molecules were studied in the gas phase, while most biological spectroscopy is carried out in the liquid or solid phases. Gas-phase spectroscopy, however, also has a place in the study of biological species because the results serve as a reference for data obtained in more complex environments. Some recent work suggests, for example, that it may be possible to distinguish between thermal and solvent effects in the optical spectra of the metalloporphyrins [67, 68]. Furthermore, gas-phase data can be used to test the validity of theoretical calculations because most are carried out for isolated molecules. Both of these concerns will be

93

encountered in the discussion that follows.

4.2   Biological Context

DNA and RNA, the molecules of heredity, are biological polymers composed of repeating nucleotide subunits [69, 70]. Each nucleotide contains a nitrogenous base, a pentose sugar, and a phosphate group. Alternating sugars and phosphate groups link together to form long chains; one base is attached to each sugar at the 1' carbon position, as shown in Fig. 4.1.

The nucleic acid bases, which are depicted in Fig. 4.2 are divided into two families: the pyrimidines and the purines. Uracil, thymine, and cytosine, the pyrimidines, are single-ringed while adenine and guanine, the purines, are double-ringed. Cytosine, adenine, and guanine are found in both DNA and RNA. Thymine, in contrast, occurs only in DNA, and is replaced by uracil in RNA. Note that thymine and uracil are identical, except for the moiety bonded to the 5' carbon. The other main difference between the constituents of DNA and RNA is that the pentose sugar is deoxyribose in DNA and ribose in RNA.

A schematic of the DNA double helix is given in Fig. 4.3. The structure is composed of two polynucleotide strands that wrap around each other about a common axis. The sugars and the phosphate groups form the polynucleotide backbone and the nucleic acid bases, which are found inside the helix, connect the two strands through hydrogen bonds. Steric factors require that the bases occur in definite pairs: adenine bonds to thymine (or uracil in RNA) whereas guanine bonds to cytosine. The sequence of A-T(U) and G-C pairs along the polynucleotide strand
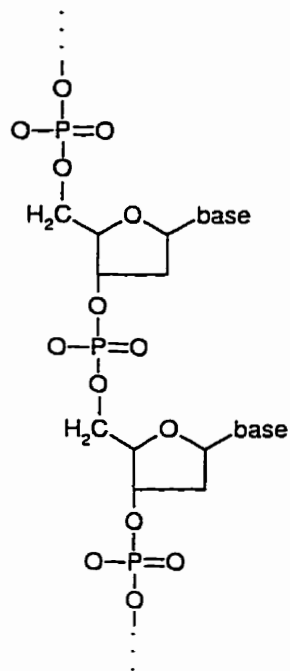
Figure 4.1: DNA and RNA are composed of repeating sub-units known as nucleotides. Each nucleotide contains a sugar, a phosphate group, and a nucleic acid base.
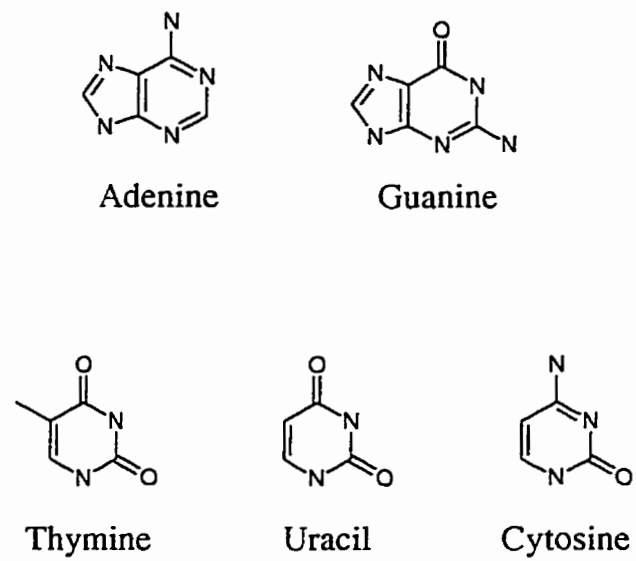
Figure 4.2: The nucleic acid bases. Adenine, guanine, and cytosine are found in both DNA and RNA. Thymine is found in DNA and is replaced by uracil in RNA.
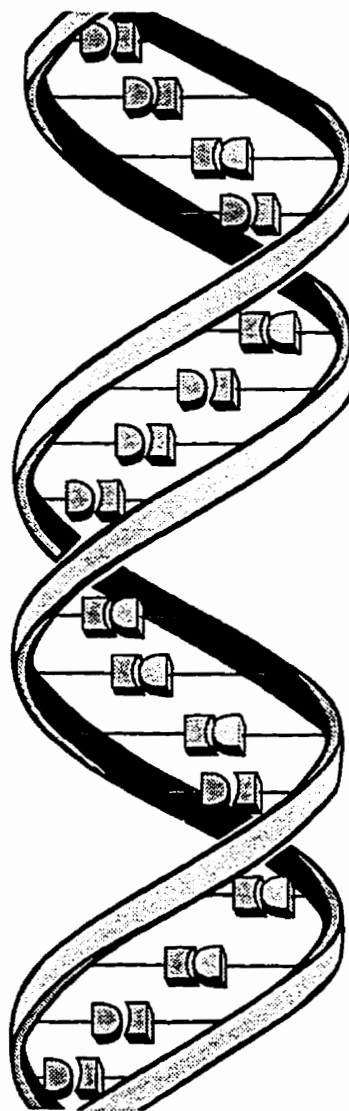
Figure 4.3: The DNA double helix consists of two polynucleotide strands coiled about a common axis [69].

encodes genetic information. When the double helix separates, the sequence of the A-T(U) and G-C pairs serves as the template for the formation of a new complementary strand. The role of RNA in eukaryotic cells is to translate the genetic code to the amino acid sequence of proteins. In some viruses, however, RNA rather than DNA is the carrier of the genetic code.

4.3   The Spectroscopic Characterization of Isolated Uracil, Thymine, and Adenine

Two techniques that approximate isolated conditions are matrix and gas-phase spectroscopy. In matrix spectroscopy, the sample is vaporized and then deposited with an excess of inert gas on a cryogenic window. Although matrix techniques yield spectra that are extremely well-resolved, the vibrational bands exhibit splittings or shifts arising from differences in the local environment in the matrix. Gas-phase spectroscopy, in turn, is hampered by the low vapor pressures and the propensity toward decomposition shown by biological molecules. It is clear that a full characterization of the spectroscopic properties of the isolated nucleic acid (NA) bases requires input from both gas-phase and matrix approaches.

The spectroscopy of the isolated NA bases also may be used to probe the molecular underpinning of point mutations. It has been proposed that mutations occur when minor enol and imino tautomers of the NA bases form nonstandard base pairs [71,72]. Fig. 4.4 illustrates the mechanism for cytosine, which is shown in the postulated imino form. Cytosine usually pairs with guanine, but it is seen that the
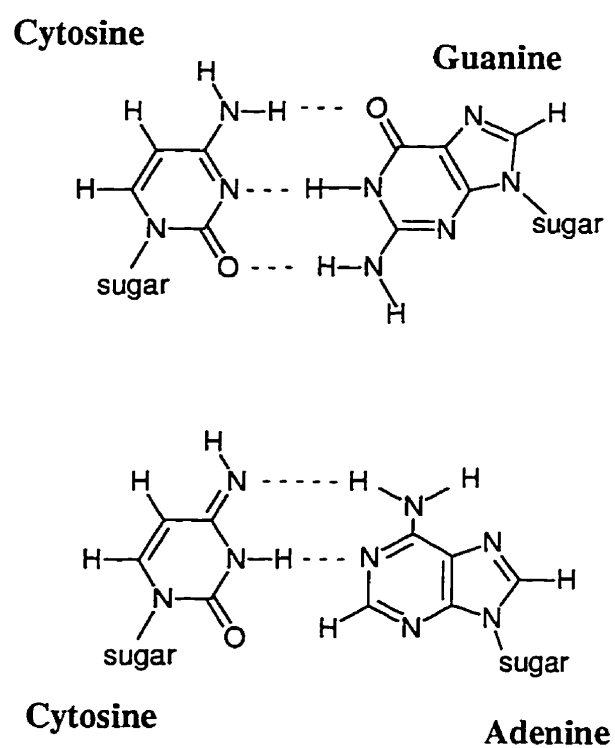
Figure 4.4: The formation of a putative cytosine-adenine mispair. Cytosine usually bonds to guanine, but in this case the minor imino form may bond to adenine instead [69].

minor tautomer can bond to adenine. This nonstandard base pair between cytosine and adenine can fit in the helix; if left uncorrected, it could lead to an error in the genetic code:

$$C \leftrightarrow G \quad \text{(parent molecule)}$$

$$C^* \leftrightarrow A \quad \text{(parent molecule)}$$

$$C \leftrightarrow G \qquad A \leftrightarrow T \quad \text{(daughter molecules)}.$$
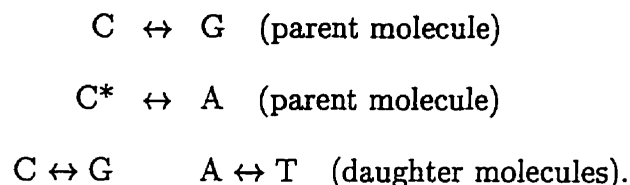
Thus, in one of the daughter molecules, a A-T pair would replace the original G-C pair. The substitution of a purine for another purine (or a pyrimidine for another pyrimidine) is known as a transition mutation. A fundamental question, however, is whether the NA bases do indeed tautomerize to the minor forms. This issue may be studied by analyzing the spectra of the isolated monomers.

Previous investigations in the infrared region include both gas-phase and matrix work. The absorption spectra of gas-phase uracil, methylated uracils, and methylated adenines have been reported in the C=O and NH stretching regions [73]. Recently, Viant *etal.* reported an analysis of a rotationally resolved spectrum of the (ν_6 C2=O,C4=O) stretch in uracil; the spectrum was recorded by exciting the molecules with an infrared diode laser in a supersonic jet expansion [74]. The infrared spectra of uracil [75–81] and deuterated uracil [78], thymine [75,79–83], and adenine [84–87] have also been reported in rare gas matrices.

As for many polyatomic molecules, the thorough assignment of NA infrared spectra requires an interplay between theoretical predictions and experimental results. Some recent theoretical treatments of the infrared spectrum of uracil include

calculations at the Hartree-Fock level using a 6-31G** basis set [80, 88] as well as calculations based on density functional methods [89]. For thymine, similar predictions of the vibrational spectra have been carried out at the SCF level using 6-31G** [80] and 6-31G(d) [83] basis sets. More current work on adenine includes Hartree-Fock calculations with a 6-31G(d,p) basis set [85, 86] and a density functional investigation [87].

4.4 Experiment

Survey spectra of uracil, thymine, and adenine were recorded over the range from 100 to 3700 cm^{-1}, a region that includes most of the fundamental modes of vibration for the NA bases. The major five nucleic acid bases were investigated in separate runs. Approximately 30 g of each compound were placed in a pyrex liner contained in a stainless steel tube. The assembly was sealed with KRS-5 (>350 cm^{-1}) or polyethylene (< 400 cm^{-1}) windows at both ends, and then evacuated. The section of the tube containing the chemical was centred in a ceramic furnace, which was heated at a rate of 10°C per minute up to working temperatures between 200 and 325°C. To prevent diffusion of the sample to the cooler ends of the tube, about 10 − 15 Torr of argon were added to the tube. A buffer gas such as argon was necessary to prevent deposition of the compound on the windows. Indeed, one run was unsuccessful because the buffer gas was not introduced.

A ceramic glower was used to align the tube along the optical axis of the spectrometer. It was also used as a blackbody source in the absorption experiments. An 90° off-axis mirror was used to collimate and reflect the infrared radiation em-

anating from the tube into the external port of a Fourier transform spectrometer (Bruker IFS 120 HR). The regions between the tube and the port as well as between the tube and the glower were purged with dry N_2 in order to minimize atmospheric contamination arising from CO_2 and H_2O.

The beam of infrared radiation, once in the spectrometer, was divided by a Ge coated KBr beamsplitter (400 - 4800 cm^{-1}) or a 3.5 μm Mylar beamsplitter (100 - 720 cm^{-1}). Liquid-nitrogen cooled In:Sb (1850 - 9000 cm^{-1}) and MCT (800-1850 cm^{-1}) detectors as well as liquid helium-cooled Si:B (300 - 1500 cm^{-1}) and bolometer (below 350 cm^{-1}) detectors were used to measure the infrared radiation. To enhance the signal-to-noise ratio, two hundred scans were co-added to yield the final interferogram. The resolution of each spectrum was 1 cm^{-1}. The Fourier transform from the interferogram to the spectrum was carried out by the Bruker Opus 3.0 software package.

Unlike the high-resolution HBO experiment, the bands often were not clearly distinguishable over the background blackbody radiation. Thus, it was necessary to ratio the spectrum to a reference spectrum that was recorded with no sample in the tube. In order to check for decomposition products, mass spectra of the sample were recorded before and after each run in the Lajoie laboratory at the University of Waterloo.

The spectra of the three NA bases were recorded at regular temperature intervals. It was observed that vibrational bands began to appear at temperatures above 200°C for each compound. Spectra were recorded in both emission and in absorption; the emission technique yielded a superior signal-to-noise ratio for most

bands. The superiority of emission over absorption was especially pronounced in the wavenumber region below $1000\,\mathrm{cm}^{-1}$, results which are similar to those obtained for the infrared spectra of polycyclic aromatic compounds [33].

4.5   Results and Discussion

The infrared spectra, illustrated in Figs. 4.6 to 4.9, were measured at 325°C for uracil and adenine, and at 300°C for thymine. Mass spectra of uracil, thymine, and adenine recorded before and after each run confirmed that no appreciable decomposition occurred during the runs. The attempts to record the gas-phase spectra of cytosine and guanine, the two other major NA bases, were unsuccessful because the compounds have low vapor pressures and decompose readily when heated.

Uracil, thymine, and guanine are planar unsymmetrical molecules that belong to the C_s point group, and are depicted in Fig. 4.5. All of the vibrational modes in these molecules are infrared active.

The gas-phase band positions and qualitative intensities are summarized in Tables 4.1 to 4.3. The error in the reported gas-phase values is approximately $\pm$ 2 cm^{-1}. For comparison, the matrix and theoretical values from the literature are also included. The calculated intensities follow the theoretical wavenumbers in parentheses and are in units of km/mol. The assignments of some modes differ among the quoted theoretical work; to remain consistent, the mode descriptions of Ref. [80] for uracil and thymine and Ref. [87] for adenine are listed. The simplified descriptions include only the dominant atomic motions in a normal mode.
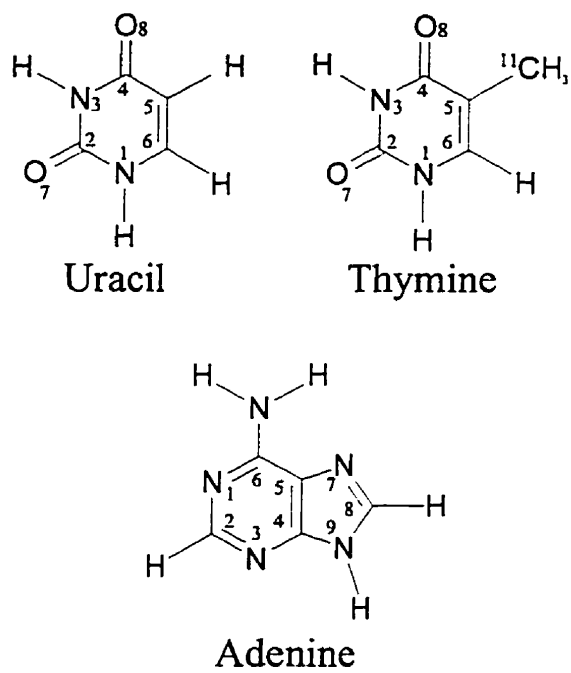
Figure 4.5: Uracil, thymine, and adenine. The atom numbering follows Ref. [80,88] for uracil, Ref. [80] for thymine, and Ref. [87] for adenine.
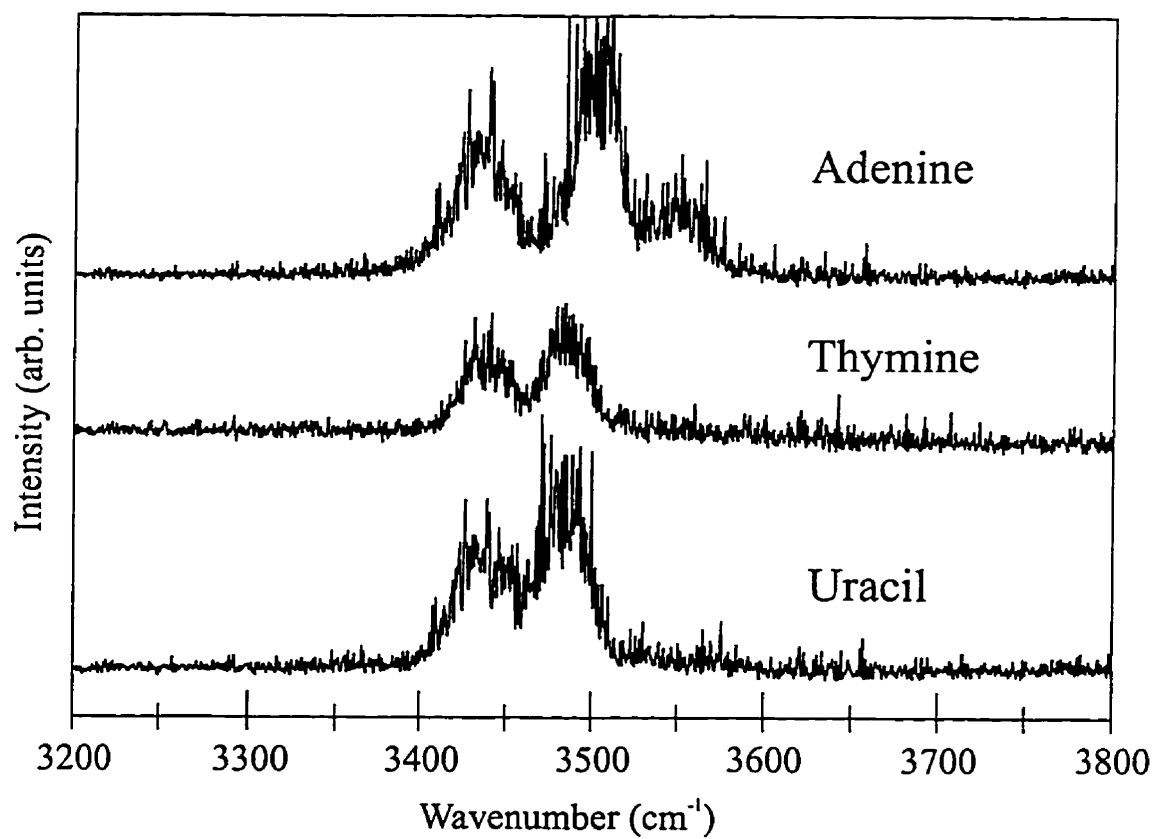
Figure 4.6: The infrared spectra of gas-phase uracil, thymine, and adenine measured with an InSb detector. The temperature was 325°C for uracil and adenine and 300°C for thymine.
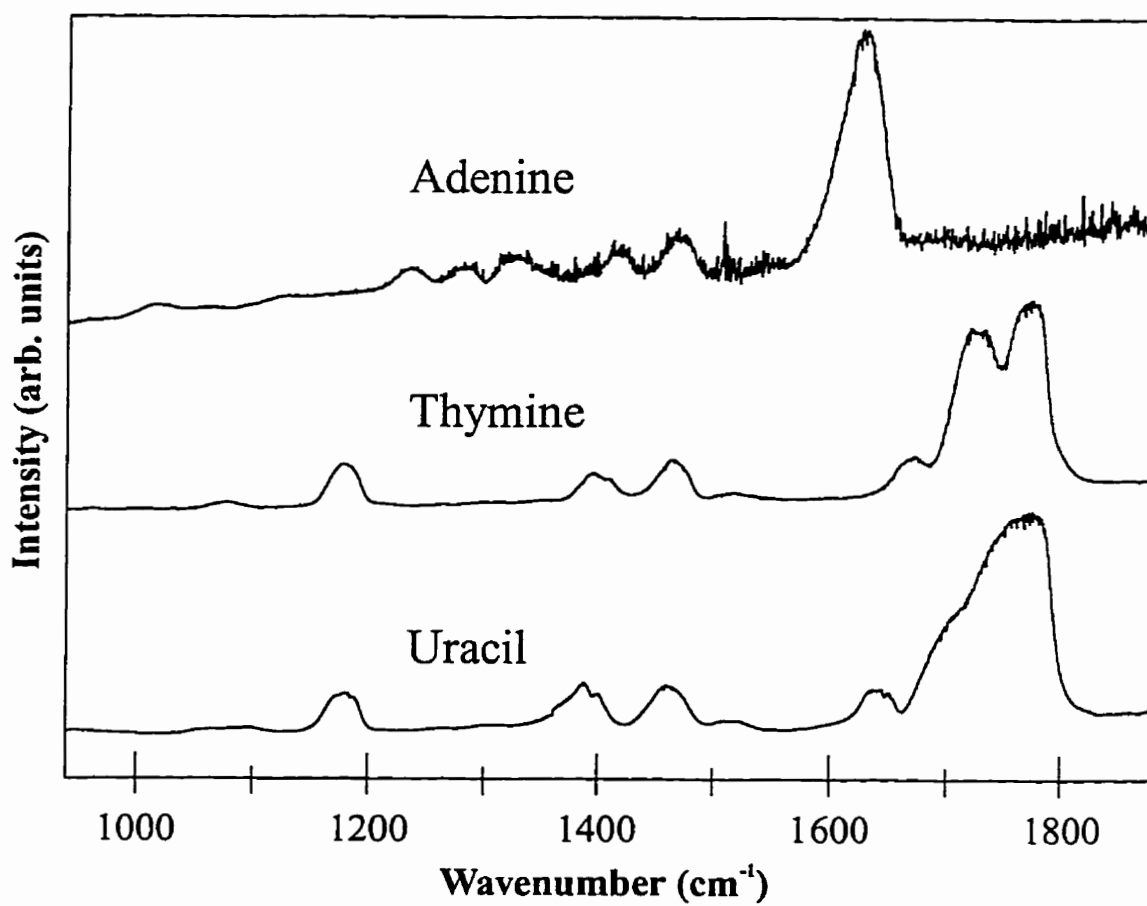
Figure 4.7: The infrared spectra of gas-phase uracil, thymine, and adenine obtained with an MCT detector. The temperature was 325°C for uracil and adenine and 300°C for thymine.
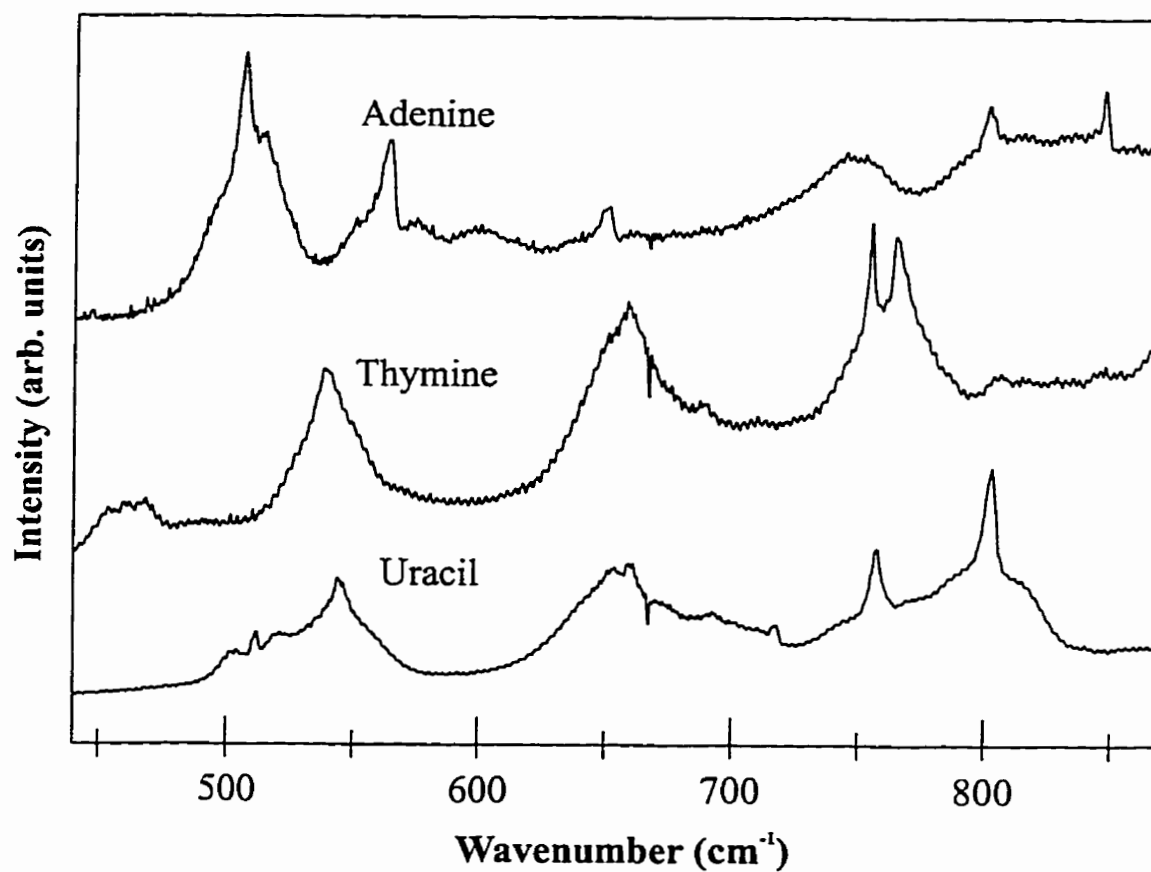
Figure 4.8: The infrared spectra of gas-phase uracil, thymine, and adenine obtained with an Si:B detector. The temperature was 325°C for uracil and adenine and 300°C for thymine.
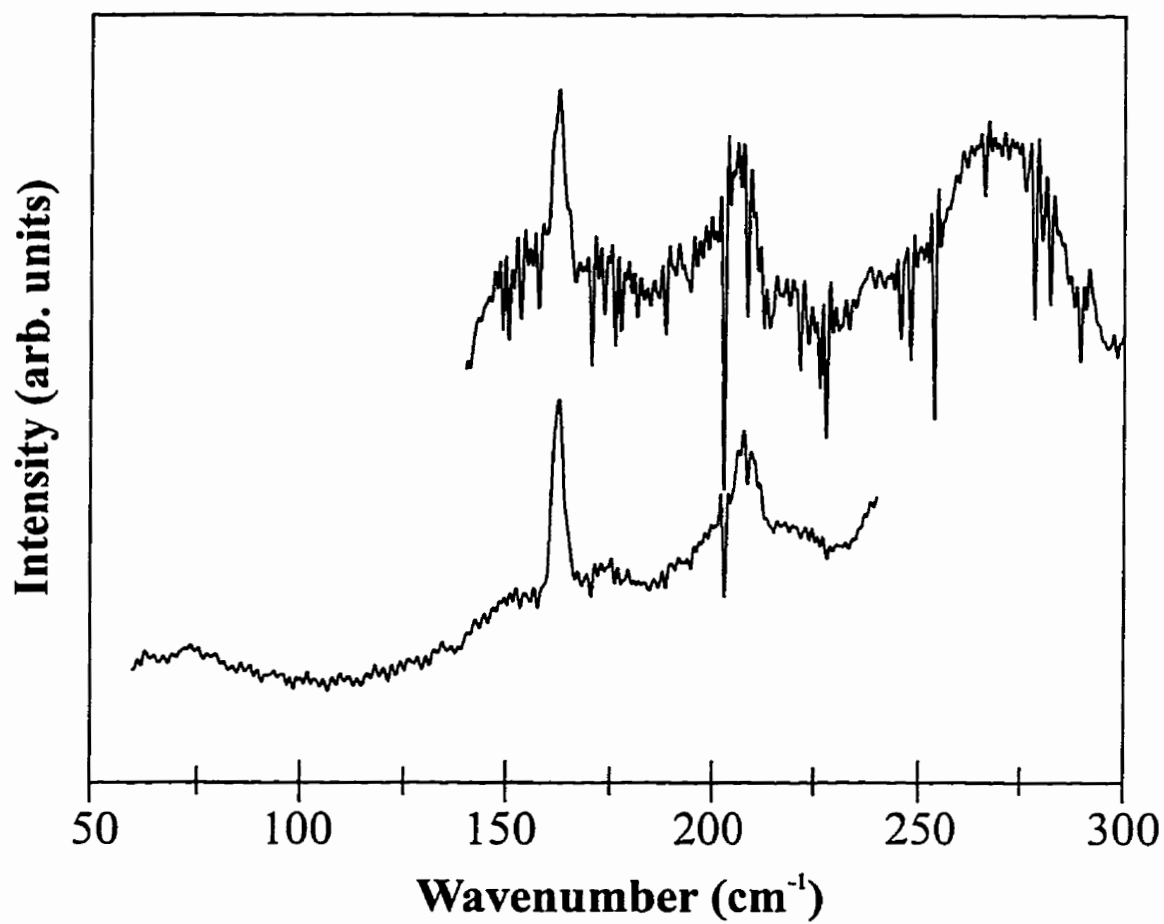
Figure 4.9: The infrared spectra of gas-phase adenine obtained with a bolometer detector using two different filters. The temperature was 325°C.

Table 4.1: Uracil. Comparison of the gas-phase, matrix, and theoretical results. Band positions are in units of cm^{-1}. For the theoretical results, the absolute intensities follow in parentheses, in units of km/mol.

Gas	Matrix		Theory		Approx. Modes
	Ref. [81]	Ref. [80]	Ref. [89] [a]	Ref. [81], [88] [b]	Ref. [80], [88]
3484s	3484.3 ⎱ 3479 ⎰ 3472.8	3485 3480 3474	3582(138)	3511(134)	νN1H
3436s	3434.5	3435	3539(74)	3477(99)	νN3H
3124m			3227(6)	3087(1)	νC5H
			3184(0)	3054(4)	νC6H
1897m					
	1791.5	1792			
	1774.3	1775			
	1770.2	1771			
1756vs	1763.7	1764			
	1762.8				
	1761.4				
	1757.5	1758	1813(705)	1811(459)	νC2O, νC4O
	1741	1742			
	1733.2	1733			
	1731.3				
	1730.3	1730			
	1728.2				
	1717.3	1719			
	1706.4	1706	1768(669)	1795(1218)	νC4O, νC2O
	1705.3				
1703(sh)vs	1703.5				
	1698.4	1699			
		1687			
		1681			
1641s	1644	1644	1678(30)	1662(126)	νC5C6
		1609			
1515m	1517	1517			
	1474.2				
	1471.9	1472			
	1467.6		1521(107)	1482(147)	βN1H, νC6N1
	1465.0	1466			
1461s	1458.5	1459			
		1425			
		1422			
1400s	1399.6 ⎱ 1396.7 ⎰	1399	1424(81)	1401(82)	βN3H, νC2N3
			1405(17)	1399(103)	βN3H, νN3C4
1387s	1388.7 ⎱ 1386.3 ⎰	1389 1387	1357(1.4)	1377(17)	βC6H, βC5H
1371(sh)m		1380			
1356(sh)m	1359.3	1359			

Uracil, cont'd.

Gas	Matrix		Theory		Approximate Mode
	1313.3⎫	1314			
	1306.2⎬	1307			
	1302.8⎭	1303			
	1217.4	1217	1260(14)	1212(17)	νN3C4, βC5H
1187s	1185 ⎫	1192			
	1184.4⎬	1185	1179(69)	1175(115)	βC6H, βN1H
1172s	1183.5⎭	1176			
1082m	1102.4	1102			
	1075.5	1076			
		1069	1083(8)	1057(20)	νC6N1, βC5H
	1068.7	1065			
990(sh)w	987.5	987	994(6)	998(0.06)	γC6H
972(sh)w	981.5	982	960(6)	969(7)	γring
952w	958.3	958	926(1)	947(6)	νring
		944			
802w	804	804	786(66)	814(103)	γC5H, γC4O
		792			
757w	756.5	757	778(2)	776(105)	γC2O
	759.2	759	747(37)	746(4)	νring
717vw	717.4	717	697(22)	723(5)	γC4O, γC5H
692vw					
	662.1	662	663(67)	658(98)	γN3H
660w	659.5 ⎫				
	657.3 ⎭				
	559	559	580(32)	548(5)	βring, βCO
	556	555			
545w	551.2	550	545(5)	530(74)	γN1H
		545			
	536.4	536	529(2)	533(7)	βCO, βring
512w	516.5	516	505(19)	505(24)	βring
		514			
395w		393	388(20)	387(32)	ring deform, γC4O
374vw		391	376(22)	383(31)	βC4O, βC2O
			160(0)	162(1)	ring deform
			137(2)	151(1)	ring deform

Abbreviations: ν, stretch; β, bend; γ, wag; R, ring; sh., shoulder; vs, very strong; s, strong; m, medium; w, weak; vw, very weak.
[a]Density functional, local density approximation.
[b]Hartree-Fock, 6-31G** basis.
Note that the numbers correspond to the atoms.

Table 4.2: Thymine. Comparison of the gas-phase, matrix, and theoretical results. Band positions are in units of cm^{-1}. For the theoretical results, the absolute intensities follow in parentheses, in units of km/mol.

Gas	Matrix		Theory	Approx. Modes
	Ref. [79]	Ref. [80]	Ref. [80][a]	Ref. [80]
3484s	3480	3480	3513(131)	νN1H
3437s	3434	3434	3477(99)	νN3H
3076m	2992		3049(6)	νC6H
2984	2971		2943(23)	νMe
2941	2940		2937(19)	νMe
	2855		2876(31)	νMe
1772vs	1768	1769		
		1759 ⎫		
		1752 ⎬	1805(720)	νC2O
		1747 ⎪		
		1742 ⎭		
		1731 ⎫		
1725vs		1725 ⎪		
	1712	1713 ⎬	1784(949)	νC4O
		1701 ⎭		
	1684	1683	1693(87)	νC5C6
1668s		1668		
1518m		1510		
	1472	1472	1485(163)	βN1H
1463s	1455	1467		
		1455	1461(1)	βMe
	1451	1451 ⎫		
	1437	1437 ⎬	1440(5)	βMe
	1433	1433 ⎭		
		1423		
		1419		
		1414		
1409s	1405	1406	1412(134)	νC2N3, βN1H
1393s	1388	1389	1404(15)	βMe
		1395	1396(10)	βN3H
		1367		
	1357	1357	1360(6)	βC6H
		1346		
		1315		
		1308		
		1297		
	1221	1221	1214(11)	βC6H, νC2N3
		1208		
	1198	1198		
		1190		

Thymine cont'd.

Gas	Matrix		Theory	Approx. Modes
1178s	1183	1184	1166(154)	νC5C11, νC6N1
		1143		
	1140	1139		
		1096		
1078m	1087	1087	1128(28)	νC6N1
1031vw		1046	1056(0.4)	βMe
	1005	1005	1002(3)	βMe
963vw	959	959	948(8)	νN1C2
931vw	936	936		
885w	890	890	934(17)	γC6H
804vw		800	785(7)	βR1
		785		
767w	764	764	778(146)	γC2O
755w	754	754	764(1)	γC4O, γC2O
	726	727	705(4)	νC4C5
689vw	662	662	658(92)	γN3H
658w	659	660		
			593(2)	βC2O, βC4O
541w	545	540 ⎫	536(7)	βR3, βR2
	541	545 ⎭	522(89)	γN1H
462vw		455	446(23)	βR2
		394	387(24)	R1, R2, R3 deform
		391	385(31)	βC2O, βC4O
			291(0.2)	γC5C11
		280	267(3)	βC5C11
			152(0.3)	Me deform
			148(0.5)	Me deform
			106(0.03)	R2 deform

Abbreviations: ν, stretch; β, bend; γ, wag; R, ring; Me, methyl; sh., shoulder; vs, very strong; s, strong; ; m, medium; w, weak; vw, very weak.
[a]Hartree-Fock, 6-31G** basis.
Note that the numbers correspond to the atoms.

Table 4.3: Adenine. Comparison of the gas-phase, matrix, and theoretical results. Band positions are in units of cm^{-1}. For the theoretical results, the absolute intensities follow in parentheses, in units of km/mol.

Gas	Matrix	Theory		Approx. Mode
	Ref. [87]	Ref. [85][a]	Ref. [87][b]	Ref. [87]
3552m	3565 ⎫ 3557 ⎱ 3555 ⎰ 3552 ⎭	3601	3676(53)	νNH2 antisym
3501s	3506 ⎫ 3503 ⎱ 3502 ⎱ 3498 ⎰ 3494 ⎰ 3489 ⎭	3530	3589(80)	νN9H
3434s	3448 ⎫ 3441 ⎱ 3438 ⎭	3471	3540(90)	νNH$_2$sym
3061m	3057	3082	3195(1)	νC8H
	3041	3026	3115(30)	νC2H
1903w	1910 1693 1659 1651 1645			
1625vs	1639 ⎫ 1633 ⎱ 1626 ⎭ 1618	1635	1641(597)	βNH$_2$ sciss νC6N10, νC5C6
	1612	1639	1617(108)	νN3C4
	1599			
		1602	1584(7)	βNH$_2$ scis
	1482	1549	1502(15)	νN7C8
1468s	1474	1485	1487(57)	νC6N1, βC2H
	1421			
1415s	1419	1419	1416(18)	νC4C5, νC4N9
	1389	1404	1400(11)	βN9H, βC2H
	1358			
1346(sh)m	1345		1350(38)	νN9C8
	1334			
1326s	1328	1346	1342(30)	νN1C2
		1330		
1280s	1290	1269	1317(67)	νC2N3
	1246	1228	1250(30)	βC8H
	1240			

Adenine cont'd.

Gas	Matrix	Theory		Approx. Mode
1234s	1229	1213	1228(11)	βNH_2 rock, νC5N7
	1133			
1126w	1127	1120	1129(20)	νC4N9
	1078			
1065(sh)w	1061		1065(17)	νC8N9
1053(sh)w		1050		
	1032			
1018m	1017			
	1005	996	1000(5)	βNH_2 rock
957vw	958	1009	953(2)	γC2H
926vw	927	922	925(15)	βr4
	887	882	882(13)	βR1
	869			
847w	848	904	831(4)	γC8H
801w	802	809	793(14)	R1 deform
748w				
	717	702	713(3)	νN3C4
	698			
	687			
	678			
		694	672(3)	γC6N10
650vw	655	652	658(6)	r4 deform, r5 deform
600vw	610	601	607(1)	r5 deform
	591			
576vw	583 }			
563w	566	557	568(64)	R1,R2 deform, γN9H
		515	528(13)	twist NH_2
		517	521(8)	R3 deform
515w	513	500	514(61)	γN9H
506m	503	505	504(5)	twist NH_2
497(sh)vw				
		298	298(0.5)	R3 deform
270m	276	271	269(22)	βC6N10
244vw	242		244(177)	inv NH_2
	214		205(90)	Rr torsion
208m		215		
162m		168	162(2)	R2 deform
		93		

Abbreviations: ν, stretch; β, bend; γ, wag; R, six-membered ring; r, five-membered ring; sh., shoulder; vs, very strong; s, strong; m, medium; w, weak; vw, very weak.
[a]Hartree-Fock, 6-31G(d,p) basis.
[b]Density functional, local density approximation.
Note that the numbers correspond to the atoms.

For large molecules such as the nucleic acid bases, the rotational levels are closely spaced and only the band envelopes can be observed. Moreover, spectral congestion from the hot bands occurs when the molecule possesses many low-lying vibrational states. In fact, a one-to-one comparison of our results with the previous matrix and theoretical results is not always possible because some of the gas-phase bands contain two or more vibrational modes. To observe most of the vibrational modes, it is necessary to heat the molecules to about 300°C. At such elevated temperatures, rotational broadening causes some of the vibrational modes to overlap. In addition, the gas-phase spectra almost certainly contain combination and overtone transitions of the lower-wavenumber vibrational modes. One example is the band observed at 576 cm^{-1} in the adenine spectrum, which is not predicted to be a fundamental mode [87].

One motivation for these experiments was to investigate whether tautomeric forms were present in the gas-phase. No evidence of the tautomerization of uracil or thymine to the enol form or of adenine to the imino form was observed, which is in agreement with previous infrared matrix experiments. If the enol tautomer were present in either uracil and thymine, an OH stretch would be expected above 3500 cm^{-1}. The imino form of adenine would expect to show a band near 3320 cm^{-1}; such a band was not observed, although it could be obscured by the strong NH stretching modes in the region. The experiments, of course, do not preclude the existence of minor tautomers: they may be present in concentrations below the detection threshold (on the order of 1% of the main form).

Where a direct comparison is possible, the agreement between the gas-phase

and matrix-phase band positions is within 10 cm^{-1}. In addition, the theoretical calculations predict the vibrational band positions to a reasonable accuracy. Both the Hartree-Fock and density functional methods yield comparable results for uracil and adenine, although one approach may lead to better results for a specific vibrational mode.

As illustrated in Figure 4.9, the gas-phase spectrum of adenine exhibits three strong modes at 162, 204, and 270 cm^{-1} and a weak mode at 244 cm^{-1}. The band positions are in good agreement with the density functional calculation, which predicts modes at 162, 205, 244, and 269 cm^{-1} [87]. The qualitative intensities of the gas-phase modes, however, do not match the predicted intensities very well. Of the four modes, the one at 244 cm^{-1} should be the strongest, with a predicted absolute intensity of 177 km/mol. Instead, the mode at 244 cm^{-1} is extremely weak in the gas-phase spectrum. Furthermore, the calculation predicts the mode at 161 cm^{-1} to be very weak, but it is observed to have a moderate intensity.

The wavenumber region below 1000 cm^{-1}, which includes most of the wagging and torsional modes, may serve as a convenient fingerprint region for the NA bases. As can be expected, the spectra of uracil and thymine are very similar at higher wavenumbers because their structures differ only by a methyl group bonded to a ring carbon. The spectra below 1000 cm^{-1}, however, contain a few modes that make the spectra distinguishable, as can be seen in Figure 4.8. It can also be noted that adenine has several clearly-defined modes in the same region. Moreover, the vibrational modes are well-separated in the lower wavenumber region and the overlap of the various modes is minimal compared to the mid-infrared (MCT detector) region.

However, a major source of interference in the far-infrared is the pure rotational spectrum of water. Even trace amounts of water vapor led to strong signal that degraded the signal-to-noise, as can be seen in the upper trace in Fig. 4.9.

The spectra of the isolated bases may help guide the interpretation of results obtained in interacting environments, such as in solvents or in molecular clusters [90]. Selected vibrational bands could be monitored for changes in position and intensity as indicators of the formation of intermolecular bonds. In the uracil and thymine spectra, the bands that are associated with the various motions of the CO groups could prove to be useful marker bands. For instance, the relative intensities of the CO bands in the spectrum of thymine oligomers dissolved in D_2O are affected when base pairing with adenine occurs [91]. In the adenine spectrum, it is probable that the bands associated with the NH_2 modes will be sensitive to the formation of intermolecular bonds.

The experiments reported here have led to the infrared spectra of uracil, thymine, and adenine over the wavenumber region that contains the fundamental modes of vibration of these molecules. Although the low vapor pressures and ease of decomposition present obstacles to gas-phase work, it is possible to obtain spectra by heating the molecules and recording the infrared emission. This work suggests that infrared emission is a sensitive technique for probing the vibrational spectra of biological and organic compounds. Furthermore, the vibrational bands of the isolated molecules may be used as marker bands for studies carried out in interacting environments. In particular, the lower frequency bands, corresponding to the ring torsions and functional group wags, may be suitable for identifying the NA bases

in more complex systems.

Chapter 5

The First Ionization Potentials of Neutral Iridium and Osmium

5.1 Overview

The work described in the previous chapters centred on the vibrational and rotational motion of molecules. At this point, the discussion turns to the investigation of the electronic motion in atoms. Whereas the motivations for the infrared emission projects were varied, the goal of this project was straightforward: the determination of the first ionization potentials of neutral osmium and iridium. Before this work, osmium and iridium were the only stable elements without highly reliable values for the first ionization potentials.

The first ionization potential of an element is defined as the energy that is

required to remove an electron from an isolated neutral atom in the gas-phase [92]:

$$X_{(g)} \rightarrow X_{(g)}^{+} + e^{-}.$$
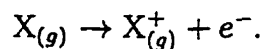
If the valence electron is excited to levels close to the ionization threshold, it is possible to observe Rydberg series that have limits corresponding to the complete removal of the valence electron [93]. A convenient method for obtaining reliable atomic ionization potentials is the extrapolation of long Rydberg series [94]. However, heavy d-block elements such as Os and Ir can yield spectra that are difficult to assign because the atoms can not be described purely by Russell-Sanders (LS) or jj coupling schemes [18].

When the spectra are extremely complex, such as for elements that experience breakdown in (LS) coupling, multiple resonance schemes can help simplify the assignment through the stepwise excitation from one or more well-characterized intermediate levels. This chapter describes the determination of the ionization potentials for neutral osmium and iridium (referred to as Os I and Ir I) using a multiresonance scheme based on the mass-analyzed threshold ionization (MATI) technique [95,96]. The method is detailed in the next sections, but the key idea involves the optical double resonance excitation of the atoms to an energy close to the ionization threshold, and the subsequent ionization with a small applied electric field.

The previous optical values for the ionization potentials of Os I and Ir I were determined by the dubious procedure of fitting the ground term and a low-lying term to a Rydberg expression. For Os I, the ionization potential of 8.7 eV (no

reported uncertainty) obtained by Albertson [97,98] is quoted by Moore [99,100]. A different value, 8.5±0.1 eV, was reported by Van Kleef and Klickenberg [101]. In another study [102], Van Kleef obtained 9.1±0.1 eV for the ionization potential of Ir I, which appears in the tables compiled by Moore [99,100].

More recently, the first ionization potentials of osmium and iridium were measured using a non-optical method. Rauh and Ackerman determined the ionization potentials of several transition metals using electron impact mass spectroscopy [103]. They reported upper limits of 8.28 eV for Os I and 9.02 eV for Ir I, after correction for excited metastable states in the neutral species.

5.2   Experiment

The experimental portion of this project was carried out at the Steacie Institute for Molecular Sciences of the National Research Council of Canada in Ottawa. Neutral osmium and iridium atoms were excited to energy levels close to the ionization threshold with the technique of optical-optical double resonance. As shown in Fig. 5.1, an intermediate level was populated by fixing the frequency of one of the pulsed lasers (pump); transitions from the intermediate state to high-energy states were excited by scanning the frequency of a second pulsed laser (probe). Ionization was induced either by direct photoionization or by the application of an electric field. The ions were then analyzed by collection with a time-of-flight mass spectrometer.

The experimental apparatus consisted of an atomic beam source and a time-of-flight mass spectrometer that were contained in two differentially-pumped cham-
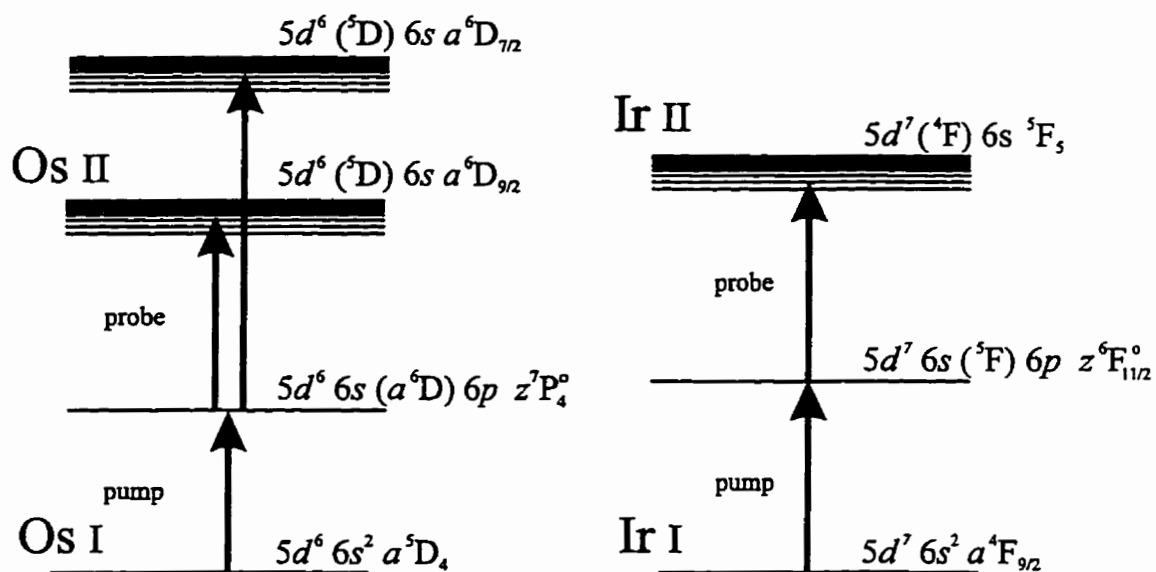
Figure 5.1: Energy-level diagram showing the pumping schemes used to obtain the near-threshold spectra for Os and Ir.

bers [104]. A schematic of the experimental apparatus is shown in Fig. 5.2. The atomic beam was produced in the first chamber with a Smalley-type source [105]. Gaseous iridium atoms were obtained by vaporizing an iridium rod with the third harmonic ($\lambda = 355$ nm) of a Nd:YAG laser (Lumonics, YM200 and YH400). In a separate run, the target was replaced by a rod consisting of osmium powder embedded in an aluminum substrate. In both experiments, the ablated atoms were expanded into vacuum with pulses of helium carrier gas released by a piezoelectric valve [106] operating at 10 Hz (400 to 500 kPa backing pressure). The atomic beam was skimmed (2 mm) before entering the chamber housing the mass spectrometer. Laser excitation of the osmium and iridium atoms was carried out in the second chamber using the frequency-doubled output from two pulsed dye lasers that were pumped by separate Nd:YAG lasers (Lumonics YM1000, $\lambda = 355$ or 532 nm). The dye lasers had a bandwidth of about 0.4 cm^{-1} and were calibrated with an optogalvanic cell using neon atomic transitions.

The intermediate state for osmium, $5d^6 6s(a^6D)6p$ $z^7P_4^\circ$, was populated by exciting the $5d^6 6s^2$ $a^5D_4 \rightarrow 5d^6 6s(a^6D)6p$ $z^7P_4^\circ$ transition at 28331.77 cm^{-1}. A second laser with output ranging from 34900 to 41580 cm^{-1} was used to scan in the vicinity of the ionization threshold from the intermediate state. In this way, Rydberg states converging to $5d^6(^5D)6s$ $a^6D_{9/2}$, the ground state of Os II, were excited; the atoms were subsequently ionized by the application of an electric field pulse. We also attempted to observe Rydberg series converging to the $5d^6$ $(^5D)6s$ $a^6D_{7/2}$ spin-orbit excited level of Os II by pumping the same intermediate level and probing with a second laser with an output ranging from 40820 to 45460 cm^{-1}. Above

124
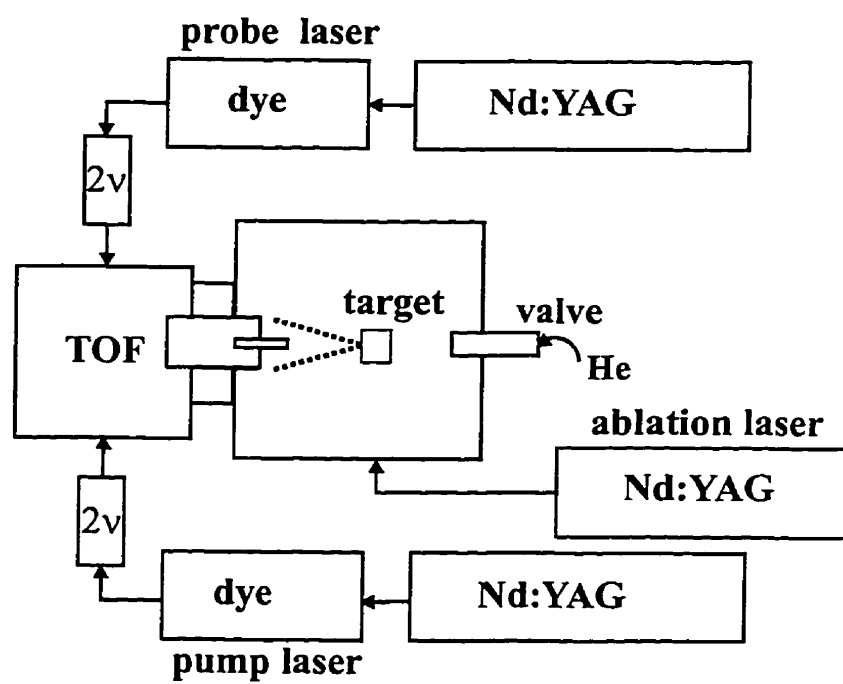
Figure 5.2: Schematic of experimental apparatus (top view).

Table 5.1: Laser set-up for double resonance; A = pump transition, B = probe transition.

Transition		ν (cm^{-1})	dye/doubling
Osmium I			
A	$5d^6 6s^2\ a^5D_4 \rightarrow 5d^6 6s(a^6D)6p\ z^7P^{\circ}_4$	28331.77	LDS 698/KDP
B	$5d^6 6s\,(a^6D)6p\ z^7P^{\circ}_4 \rightarrow 5d^6\,(^5D)6s\ a^6D_{7/2}$	34900-41580	C500/BBO
B	$5d^6 6s\,(a^6D)6p\ z^7P^{\circ}_4 \rightarrow 5d^6(^5D)6s\ a^6D_{9/2}$	40820-45460	C460/BBO
Iridium I			
A	$5d^7 6s^2\ a^4F_{9/2} \rightarrow 5d^7 6s(^5F)6p\ z^6F^{\circ}_{9/2}$	32513.43	R640/KDP
B	$5d^7 6s(^5F)6p\ z^6F^{\circ}_{9/2} \rightarrow\ 5d^7\,(^4F)6s\ ^5F_5$	34900-41580	C500/BBO

threshold, photoionization occurred directly. For iridium, the $5d^7 6s(^5F)6p\ z^6F^{\circ}_{9/2}$ intermediate state at 32513.43 cm^{-1} was populated from the $5d^7 6s^2\ a^4F_{9/2}$ ground state. High-lying states converging to the $5d^7\ (^4F)6s\ ^5F_5$ ground state of Ir II, as well as states above the ionization threshold, were excited from the intermediate state with a laser output ranging from 34900 to 41580 cm^{-1}. The pump and probe transitions and the corresponding laser set-ups are summarized in Table 5.1.

For both runs, the laser excitation was carried out under conditions very close to zero-field by holding both extraction and repeller grids at the same voltage (2600 to 3000 V). After a delay of 5 μs, the potential on the draw-out grid was depressed by approximately 500 V for a period of 26 μs. The ions were detected by dual microchannel plates, and the resulting signal was amplified and digitized.

5.3 Results and Analysis

In mass-analyzed techniques, it is vital to know whether the ion originated from above or below the ionization threshold. In MATI-type experiments, it is possible to discriminate between the two classes of ions because a residual field exists between the draw-out and repeller grids. Though small, it is sufficient to accelerate the ions away from the Rydberg atoms before the extraction pulse is applied. The two types of ions have different flight times and they are designated prompt (photoionized) and delayed (field-ionized).

Fig. 5.3 illustrates the time-of-flight spectra for both the prompt and delayed ions of osmium obtained by the pumping scheme described earlier (see Fig. 5.1). The spectrum of the prompt ions was observed with a total laser excitation of 68071.3 cm^{-1} while that for the delayed ions was collected with an excitation of 68035.6 cm^{-1}. It can be noted that the four major isotopes of osmium ($^{188,189,190,192}Os$) were partially resolved. For iridium, similar mass spectra clearly showing the two isotopes ($^{191,193}Ir$) were obtained.

Fig. 5.4 depicts the spectra obtained for osmium by scanning the probe laser in the near-threshold region while the mass spectrometer was gated for the specific mass-to-charge ratio for either the prompt or delayed ions. In order to minimize the interference from the different isotopes, the mass-spectrometer was gated for the heaviest major isotope for collection of the delayed spectra and the lightest major isotope for the collection of the prompt spectra. Fig. 5.5 depicts the similar spectra for iridium. The point at which the prompt and delayed curves cross, however, is not the true ionization potential. This apparent ionization potential arises because
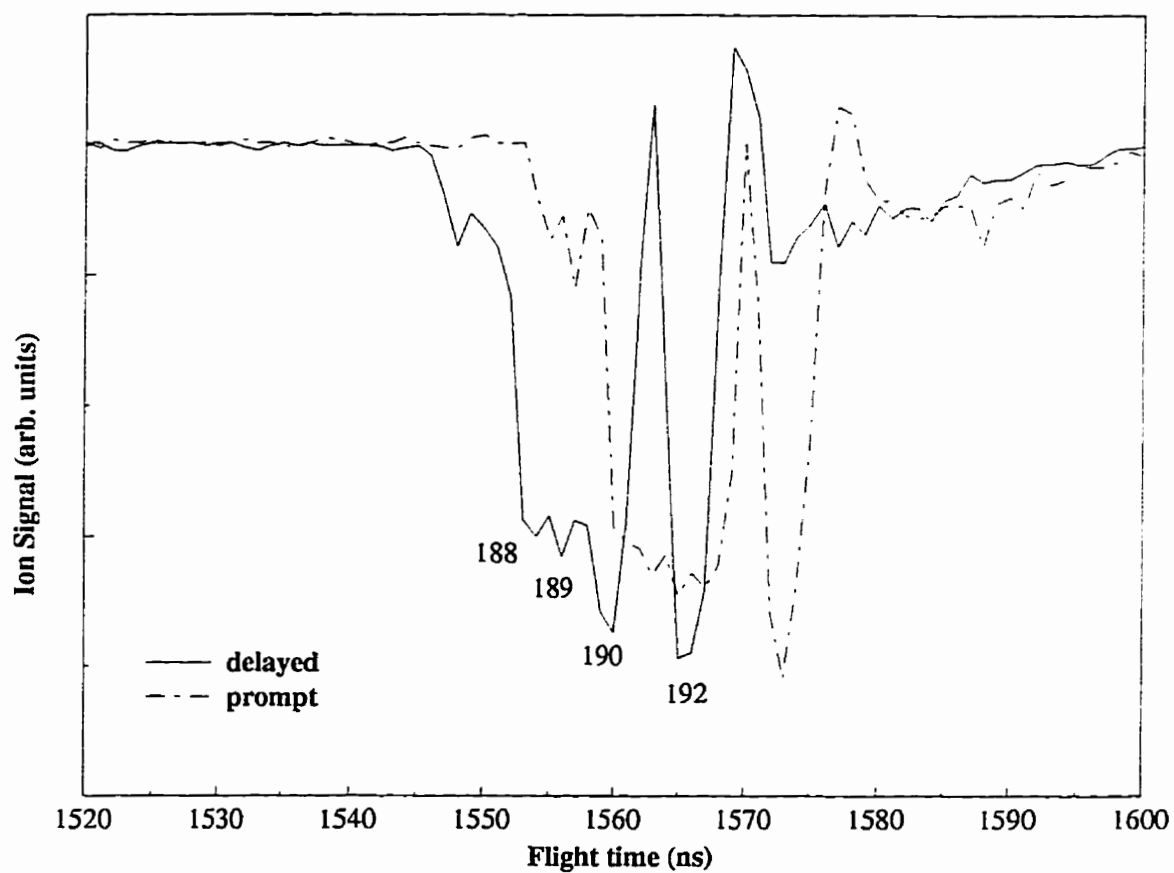
Figure 5.3: Time-of-flight spectra of osmium obtained with the pumping scheme labelled Os in Fig. 5.1. The prompt spectrum (solid line) was obtained with a total laser energy of 68071.3 cm^{-1} while the delayed spectrum (dashed line) was obtained with a total laser energy of 68035.6 cm^{-1}.

a small residual DC field lowers the ionization potential, typically by 14 cm^{-1} for the apparatus described here [107]. This correction is added to the apparent ionization potentials to yield first ionization potentials of 68058±2 cm^{-1} for Os I and and 72324±2 cm^{-1} for Ir I.

A more accurate method for obtaining the ionization potentials is based on the fitting of Rydberg series to the standard expression:

$$\bar{\nu}_n = \bar{\nu}_o - \frac{R_m}{(n-\delta)^2},$$

(5.1)

where $\bar{\nu}_n$ is the wavenumber of the Rydberg levels labelled with successively increasing integral n numbers, $\bar{\nu}_o$ is the wavenumber of the limit, δ is a constant, and R_m is the Rydberg constant for osmium or iridium.

When the n values are the principal quantum numbers, δ is the quantum defect for the series. The δ depends on the orbital angular momentum $l = 0, 1,$ or $2 \ldots$ for the corresponding s, p, and d Rydberg electron. For a given n, the quantum defect is a measure of the radial probability densities or the penetration of the atomic core. In the absence of perturbations, the δ varies smoothly with n until it levels off for very high n, as would be observed in highly excited Rydberg series [94]. Thus, atomic transitions to high-lying energy levels can yield spectra that are simple in appearance because the electron is weakly coupled to the ion core.

In both Os I and Ir I, the outer electron in the intermediate state is a $6p$ electron. Excitation of this state would be expected to yield several s and d series [100]. In order to assign the observed transitions, approximate quantum defects for the Os I and Ir I ns and nd series were calculated from published energy levels [107–109]. The
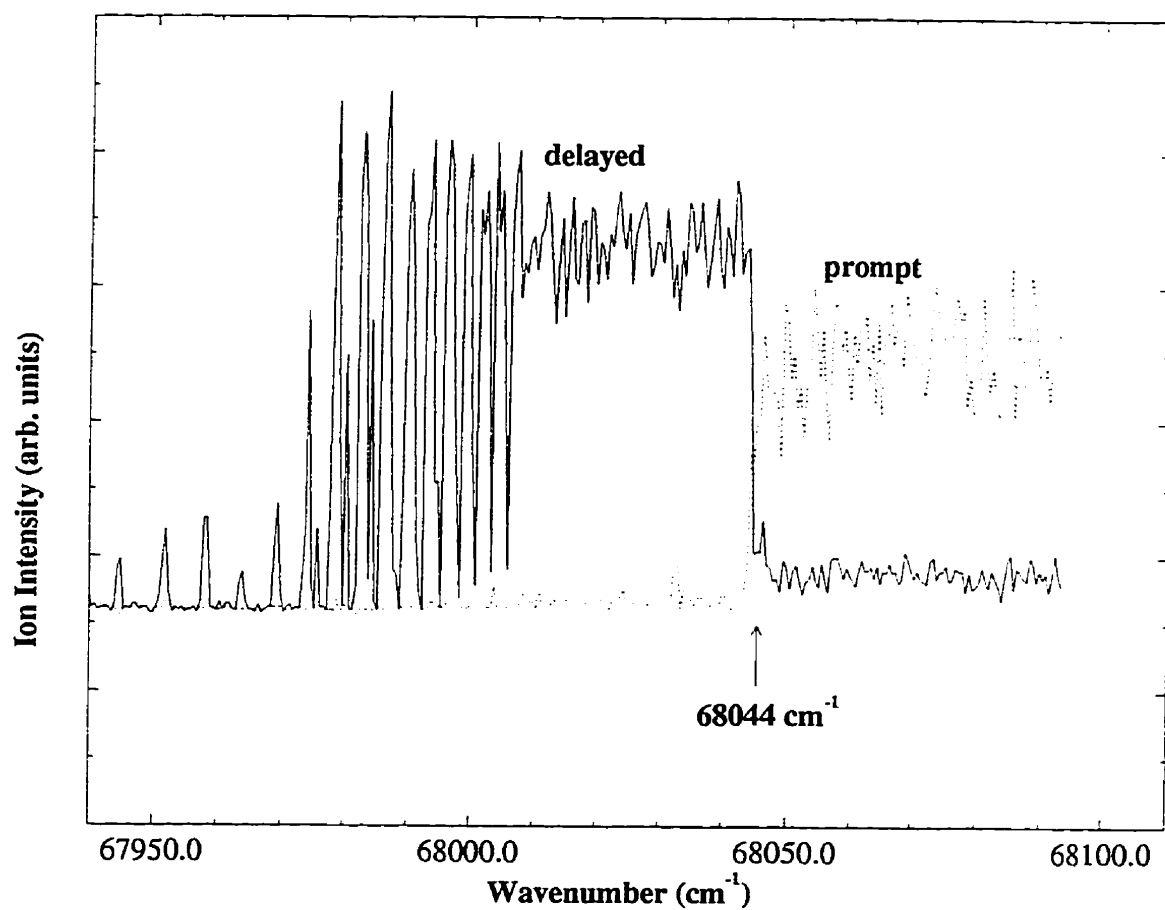
Figure 5.4: Rydberg spectra obtained for osmium with the pumping scheme shown in Fig. 5.1 and by collecting the delayed and prompt Os II ions. The appearance potential is the point at which the two curves cross.
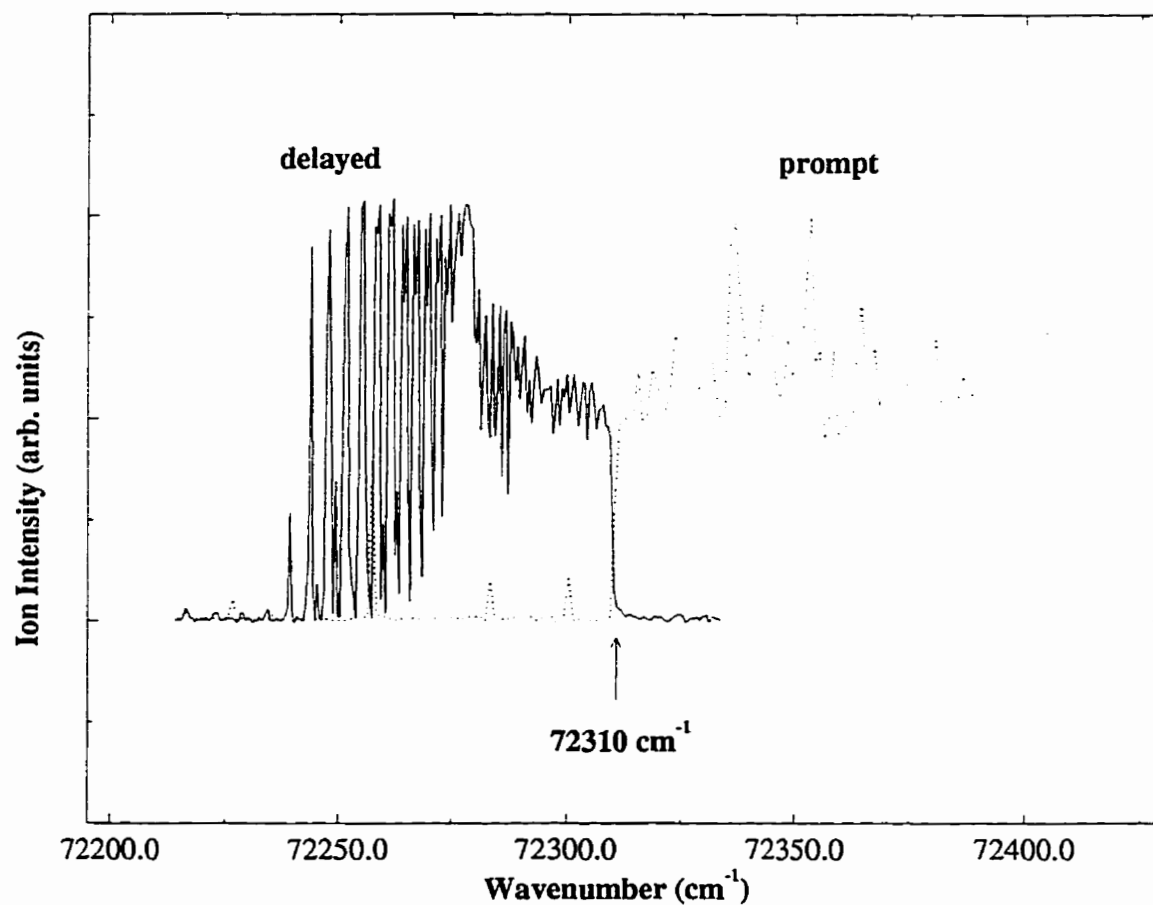
Figure 5.5: Rydberg spectra obtained for iridium with the pumping scheme shown in Fig. 5.1 and by collecting the delayed and prompt Ir II ions. The appearance potential is the point at which the two curves cross.

values obtained were 4.7 for the s series and 3.0 for the d series for both elements. The $\delta(s) > \delta(d)$ because the s electron has a greater penetration of the atomic core. The preliminary quantum defect values and the ionization values obtained from the crossing of the prompt and delayed spectra (Figs. 5.4 and 5.5) were used to identify the principal quantum number and the series for each observed transition. One s and d series was assigned for each atom. Details of the spectra are shown in Figs. 5.6 and 5.7.

For both osmium and iridium, the strong lines exhibit a splitting that may be attributed to the presence of several d series. A successful fit could be carried out only for the strongest d series lines for each atom. In the final step, the transitions and quantum numbers were used in a non-linear least-squares fit to the Rydberg formula with the ionization potential and quantum defect as the variable parameters. The standard deviations that are reported in parentheses correspond to 3σ.

The average ionization limit for Os I was observed to be 68058.9 ± 0.4 cm^{-1} to which an uncertainty of 1.2 cm^{-1} was added to account for error in the laser calibration, resulting in a value of 68058.9 ± 1.6 cm^{-1}. Similarly, the ionization limit for Ir I was found to be 72324.9 ± 1.8 cm^{-1}. The fitting parameters and the results of the fits are summarized in Table 5.2.

In order to corroborate the values for the ionization potentials, attempts were made to record Rydberg series converging to a low-lying state in the singly-ionized atoms. No Rydberg series was detected for Ir II, but for Os II, a series was observed converging to the $5d^6$ (^{5}D)$6s$ a^6D$_{7/2}$ state lying at 3593.15 cm^{-1} above the $5d^6$ (^{5}D)$6s$ a^6D$_{9/2}$ spin-orbit component [100]. Several lines, as indicated in Fig.
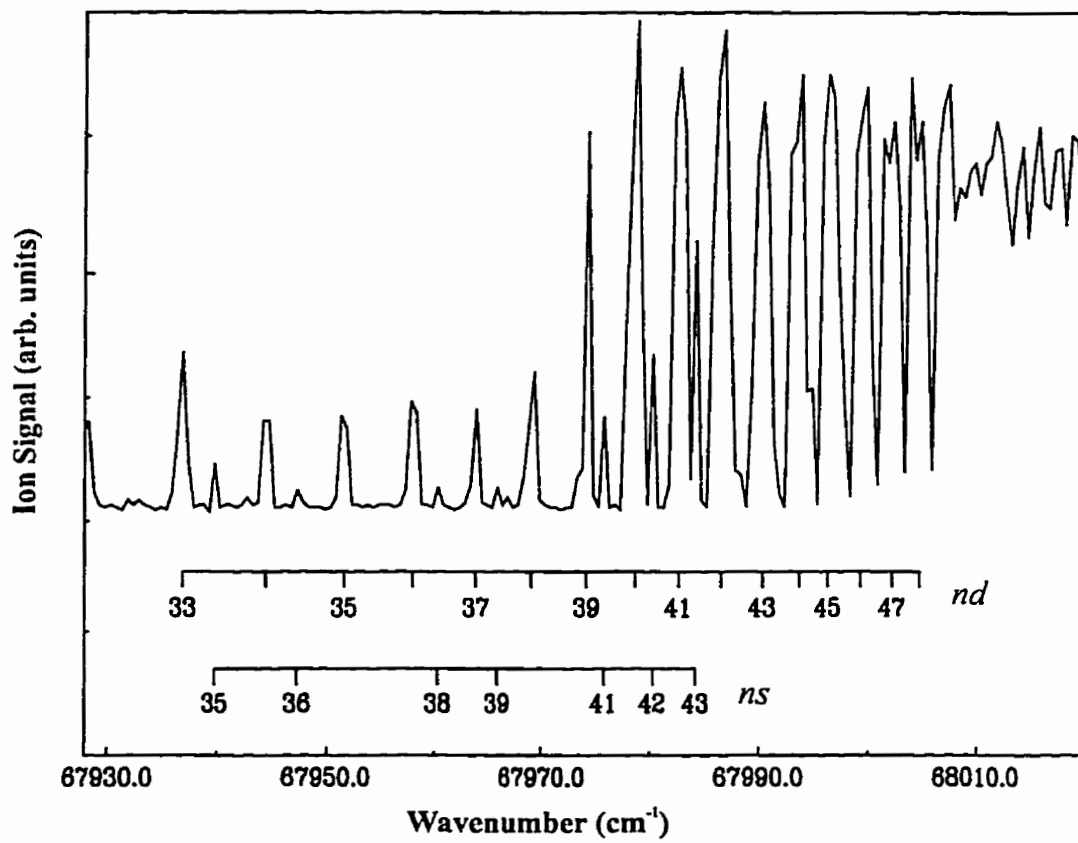
Figure 5.6: High-lying *ns* and *nd* Rydberg series observed by collecting the delayed Os II ions using the pumping scheme labelled in Fig. 5.1
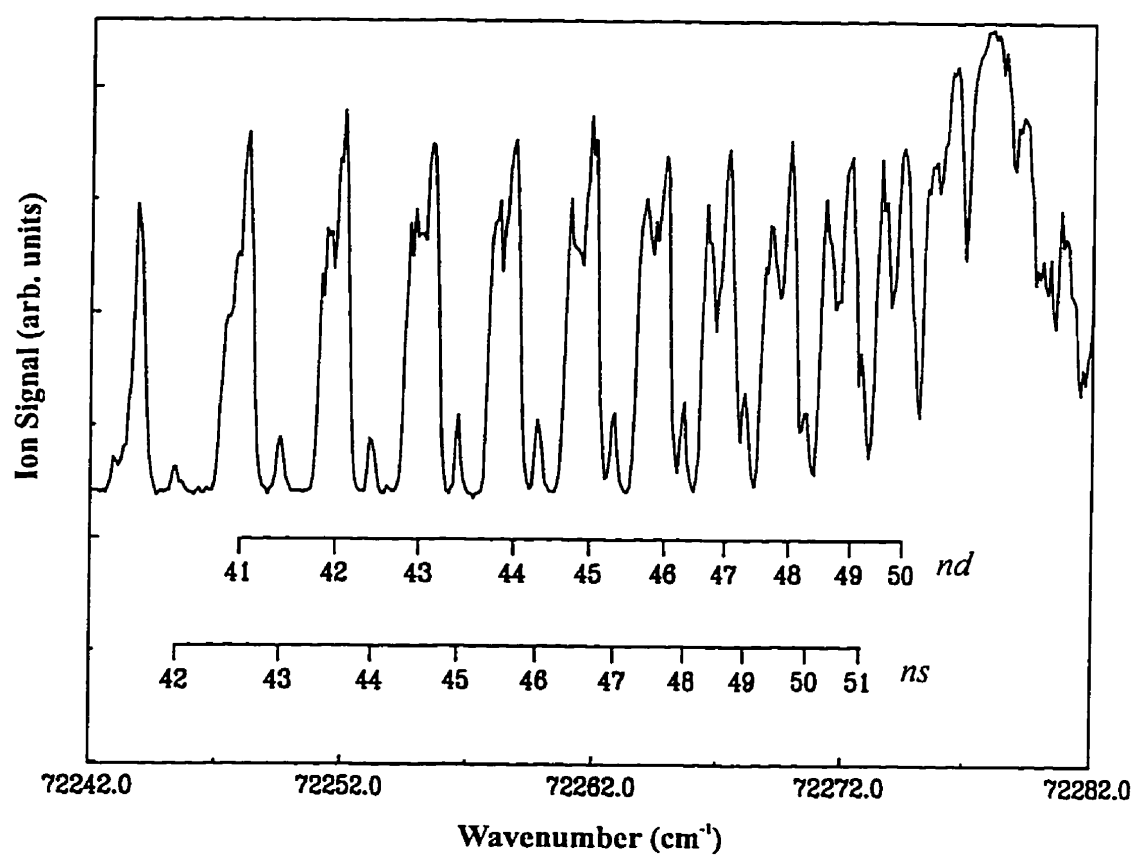
Figure 5.7: High-lying ns and nd Rydberg series observed by collecting the delayed Ir II ions using the pumping scheme labelled in Fig. 5.1

Table 5.2: Convergence limits and quantum defects for Os I,II and Ir I. The 99% confidence limit uncertainties are in parentheses in units of the last decimal place.

Element	convergence level in ion	series type	n range	limit (cm^{-1})	σ	std. error (cm^{-1})
Os	$5d^6(^5\text{D})6s\ a^6\text{D}_{9/2}$	s	30–46	68058.8(3)	4.63(4)	0.15
Os	$5d^6(^5\text{D})6s\ a^6\text{D}_{9/2}$	d	20–48	68058.9(2)	3.01(1)	0.16
Os	$5d^6(^5\text{D})6s\ a^6\text{D}_{7/2}$	d	21–39	71654.5(2)	3.07(1)	0.18
Ir	$5d^7\ (^4\text{F})6s\ ^5\text{F}_5$	s	42–51	72323.6(3)	4.54(9)	0.050
Ir	$5d^7\ (^4\text{F})6s\ ^5\text{F}_5$	d	39–50	72324.1(4)	3.01(10)	0.090

5.8, were assigned tentatively to a nd series and fit to Eq. (5.1). The wavenumber of the limit $\bar{\nu}_o$ was determined to be $71654.5 \pm 1.4 \text{cm}^{-1}$, which places the first ionization potential at $68061.4 \pm 1.4 \text{ cm}^{-1}$. This value is in good agreement with the first ionization potential of Os I. A comparison of the experimental results with the previous literature values is provided in Table 5.3. The quantum defects obtained in the fits are in agreement with those of other row five and six transition elements [104, 107–109, 111].

Table 5.3: Summary of ionization potential values for Os I and Ir I. The 99% confidence limit uncertainties are in parentheses in units of the last decimal place.

Element	IP[1] (cm^{-1})	IP[1] (eV)	Method[2]	Ref.
Os I	68058(2)	8.4381(25)	A	This work
	68058.9(16)	8.43823(20)	B	This work
	70450	8.7(1)	C	Ref. [97–100]
	68560(800)	8.5(1)	C	Ref. [101]
	66783	8.28	D	Ref. [103]
Ir I	72324(2)	8.9670(25)	A	This work
	72323.9(18)	8.96702(22)	B	This work
	73000(800)	9.1(1)	C	Ref. [99, 100, 102]
	72751	9.02	D	Ref. [103]

[1]The conversion between eV and cm^{-1} is 1 eV = 8065.541 cm^{-1} [110]. Note that the literature values were originally reported as eV.

[2]Method A: The intersection of the prompt and delayed spectra.
Method B: Non-linear fit of high-lying Rydberg states.
Method C: Fit to ground state and excited level.
Method D: Electron impact measurements corrected for metastable states in the neutral atoms (upper limits; no reported error).
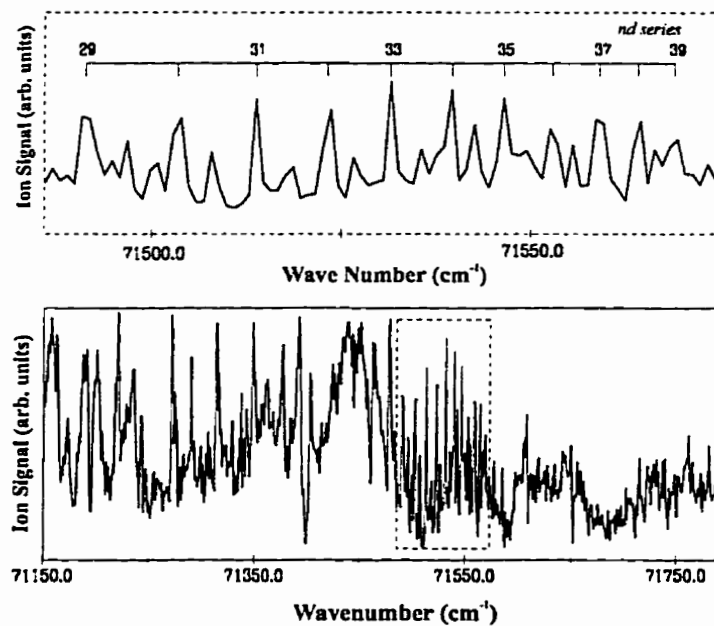
Figure 5.8: Rydberg spectra obtained by collecting the prompt Os II ions obtained by excitation from an intermediate state to the $5d^6$ (^{5}D)$6s$ a^6D$_{7/2}$ state at 3593.15 cm^{-1} in the ion as shown in Fig. 5.1. The upper trace is an expanded view of the region enclosed by dotted lines in the overall spectrum (lower trace).

Final Remarks

Thus far the discussion has been in the passive voice, but at this point, I will break with tradition and conclude on a more personal note. No project is ever neatly tied up (well at least the ones I work on), and I would like to mention some avenues that deserve further exploration.

The first project centred on the molecule HBO. We were trying to record the spectrum of BCl for an undergraduate in our laboratory, and luckily (for me) it turned out to be a triatomic. The project began purely as a spectroscopic investigation, but then I began to appreciate that the chemistry of high-temperature reactions is quite intricate. These experiments have revealed that HBO indeed may be a major intermediate in boron combustion.

Usually, our synthetic approaches in high-temperature experiments are straightforward: a few chemicals are placed in a furnace and then heated to temperatures on the order of 1000°C. The chemistry of the HBO reaction indicates that it may be worthwhile to strengthen the connection between the chemistry and spectroscopy. For example, there is a whole area of high-temperature ceramic chemistry that can be investigated. Emission measurements of high-temperature ceramic processes, such as corrosion, may even have some practical applications in process control. On a more fundamental level, it would be interesting to study the isomerizations of Group 13 elements such as the HBO-BOH or the AlOH-HAlO systems. For the HBO as well as the MATI projects, it was at once both satisfying and somewhat ironic that what begin as detailed spectra can be reduced to a few parameters, or even two numbers, but therein lies the power of spectroscopic approaches.

In the nucleic acid bases project, infrared emission spectroscopy proved to be a sensitive technique even for temperatures below 350°C. The far-infrared proves to be a convenient region for examining the ring motions of large molecules. Furthermore, the tautomeric idea deserves further investigation. The detection of tautomers, if they indeed exist, most probably requires very sensitive techniques. In my ideal experiment, I could use a bright tunable infrared source to probe these molecules in absorption. In addition, it would be interesting to partially resolve the rotational-vibrational structure, as the Saykally group has done for uracil [74].

References

1. E.B. Wilson, Jr., J.C. Decius, and P.C. Cross, *Molecular Vibrations* (McGraw-Hill Book Company, New York, 1955).

2. H. Goldstein, *Classical Mechanics* (Addison-Wesley Publishing Company, Reading, Massachusetts, 1965).

3. H.C. Allen, Jr. and P.C. Cross, *Molecular Vib-Rotors* (John Wiley and Sons, New York, 1963).

4. D. Papoušek and M.R. Aliev, *Molecular Vibrational-Rotational Spectra* (Elsevier, Amsterdam, 1982).

5. P. Gorry, *Basic Molecular Spectroscopy* (Butterworths, London, 1985).

6. K. Nakamoto, *Infrared and Raman Spectra of Inorganic and Coordination Compounds*, fourth ed. (John Wiley and Sons, New York, 1986).

7. J.M. Hollas, *High Resolution Spectroscopy* (Butterworths, New York, 1982).

8. D.M. Bishop, *Group Theory and Chemistry* (Dover, New York, 1973).

9. B.T. Darling and D.M. Dennison, Phys. Rev. **57**, 128 (1936).

10. J.K.G. Watson, Mol. Phys. **15**, 479 (1968).

11. I. Levine, *Molecular Spectroscopy* (John Wiley and Sons, New York, 1975).

12. J.K.G. Watson, Mol. Phys. **19**, 465 (1970).

13. J.J. Sakurai, *Modern Quantum Mechanics* (Addison-Wesley Publishing Company, Redwood City, California, 1985).

14. G. Herzberg, *Infrared and Raman Spectra of Polyatomic Molecules*, Vol. 2 of *Molecular Spectra and Molecular Structure* (Krieger Publishing Company, Florida, 1991).

15. W. Gordy and R.L. Cook, *Microwave Molecular Spectra* (John Wiley and Sons, New York, 1984).

16. H. Kroto, *Molecular Rotation Spectra* (Dover, New York, 1992).

17. I.M. Mills, in *Molecular Spectroscopy: Modern Research*, edited by K. N. Rao and C. W. Matthews (Academic Press, New York, 1972), Chap. Vibration-Rotation Structure in Asymmetric and Symmetric-Top Molecules, p. 115.

18. G. Herzberg, *The Spectra and Stuctures of Simple Free Radicals* (Dover Publications, New York, 1971).

19. D.H. Rank, G. Skorinko, D.P. Eastman, and T.A. Wiggins, J. Opt. Soc. Am. **5**, 421 (1960).

20. T. Oka, J. Chem. Phys. **47**, 5410 (1967).

21. D. Harris and M. Bertolucci, *Symmetry and Spectroscopy* (Dover Publications, New York, 1989).

22. R. Bell, *Introductory Fourier Transform Infrared Spectroscopy* (Academic Press, San Deigo, 1972).

23. D.W. Green and G.T. Reedy, *Applications to Chemical Systems*, Vol. 1 of *Fourier Transform Infrared Spectroscopy* (Acadecmic Press, New York, 1978), p. 1.

24. P. Griffiths and J. de Haseth, *Fourier Transform Infrared Spectroscopy*, Vol. 83 of *Chemical Analysis* (John Wiley and Sons, New York, 1986).

25. A. Thorne, *Spectrophysics* (Chapman and Hall, London, 1988).

26. R.B. Sanderson, in *Molecular Spectroscopy: Modern Research*, edited by K. N. Rao and C. W. Matthews (Academic Press, New York, 1972), Chap. Fourier Spectroscopy, p. 297.

27. P.F. Bernath, Annu. Rev. Phys. Chem. **41**, 91 (1990).

28. P.F. Bernath, Chem. Soc. Review **90**, 111 (1996).

29. J. Wormhoudt, J.A.Conant, W.F. Herget, *Infrared Methods for Gaseous Measurements* (Marcel Dekker, New York, 1985), p. 1.

30. H. Worden, R. Beer, and C.P. Rinsland, J. Geophys. Res. **102**, 1287 (1997).

31. R. Beer, *Remote Sensing by Fourier Transform Spectrometry* (Wiley, New York, 1992).

32. P. Bernath, *Spectra of Atoms and Molecules* (Oxford University Press, New York, 1995).

33. K.Q. Zhang, B. Guo, P. Colarusso, and P.F. Bernath, Science **274**, 582 (1996).

34. D.E. Milligan and M.E. Jacox, in *Molecular Spectroscopy: Modern Research*, edited by K. N. Rao and C. W. Matthews (Academic Press, New York, 1972), p. 259.

35. K. Huber and G. Herzberg, *Constants of Diatomic Molecules* (Van Nostrand Reinhold, New York, 1979).

36. M.E. Jacox, in *Journal of Physical and Chemical Reference Data*, edited by N. I. of Standards and Technology (American Chemical Society and the Americal Institute of Physics, Gaithersburg, 1975), Chap. Vibrational and Electronic Energy Levels of Polyatomic Transient Molecules, p. 35.

37. E.R. Lory and R.F. Porter, J. Am. Chem. Soc. **97**, 3402 (1972).

38. Y. Yamaguchi, B.J. DeLeeuw, G. Vacek, C.A. Richards, and H.F. Schaefer III, J. Chem. Phys. **101**, 3006 (1994).

39. J.S. Pilgrim, D.L. Robbins, and M.A. Duncan, Chem. Phys. Lett. **202**, 203 (1993).

40. N.M. Lakin, J.M. Brown, I.R. Beattie, and P.J. Jones, J. Chem. Phys. **98**, 8704 (1993).

41. J.L. Gole and H.H. Michels, J. Chem. Phys. **103**, 7844 (1995).

42. C.A. Richards, Jr., G. Vacek, B.J. DeLeeuw, Y. Yamaguchi, and H. Schaefer III, J. Chem. Phys. **102**, 1280 (1994).

43. P. Rosmus, Angew. Chem. Int. Ed. Engl. **27**, 1329 (1988).

44. S.H. Bauer, Chem. Rev. **96**, 1907 (1996).

45. B.S. Ault, Chem. Phys. Lett. **157**, 547 (1989).

46. N.L. Garland, C.T. Stanton, H.H. Nelson, and M. Page, J. Chem. Phys. **95**, 2511 (1991).

47. L. Andrews and T. Burkholder, J. Phys. Chem. **95**, 8554 (1991).

48. Y. Kawashima, K. Kawaguchi, and E. Hirota, Chem. Phys. Lett. **131**, 205 (1986).

49. Y. Kawashima, Y. Endo, and E. Hirota, J. Molec. Spectrosc. **133**, 116 (1989).

50. Y. Kawashima, K. Kawaguchi, and E. Hirota, Chem. Phys. Lett. **135**, 441 (1987).

51. K.Q. Zhang, B. Guo, and P.F. Bernath, J. Molec. Spectrosc. **245**, 600 (1996).

52. M. Schneider *et al.*, $^{12}C^{16}O$ *Laser Frequency Tables for the 34.2 to 62.3 THz Region* (National Bureau of Standards, Gaithersburg, 1988).

53. H. Hedderich, K. Walker, and P.F. Bernath, J. Molec. Spectrosc. **149**, 314 (1991).

54. K.J Klabunde, *Chemistry of Free Atoms and Particles* (Academic Press, New York, 1980).

55. E. Pearson and R. McCormick, J. Chem. Phys. **58**, 1619 (1973).

56. R. Sams and A. Maki, J. Mol. Struct. **26**, 107 (1975).

57. P. Turner and I. Mills, Molec. Phys. **46**, 161 (1982).

58. K.-M. Chen *et al.*, J. Phys. Chem. **100**, 488 (1996).

59. J.M. Brown *et al.*, J. Molec. Spectrosc. **55**, 500 (1975).

60. G. Amat and H. Nielson, J. Molec. Spectrosc. **2**, 152 (1958).

61. A. Maki and J. D.R. Lide, J. Chem. Phys. **47**, 3206 (1967).

62. F.C. De Lucia, J. Chem. Phys. **67**, 4262 (1977).

63. T. Nakagawa and Y. Morino, J. Molec. Spectrosc. **31**, 208 (1969).

64. Y. Kawashima, Y. Endo, and E. Hirota, Columbus abstract, WF1, 1989.

65. I. Mills, T. Cvitaš, K. Homann, N. Kallay, and K. Kuchitsu, *Quantities, Units, and Symbols in Physical Chemistry* (Blackwell Scientific Publications, Oxford, 1988).

66. O. Svelto, *Principles of Lasers*, 3rd ed. (Plenum Press, New York, 1989).

67. W. Westerfield, W. Davis, and J. Rodriguez, Rev. Sci. Instrum. **65**, 1523 (1994).

68. W. Davis, S. Calongne, and J. Rodriguez, J. Chem. Phys. **102**, 716 (1995).

69. C.U.M. Smith, *Elements of Molecular Neurobiology* (John Wiley and Sons, Chichester, 1996).

70. L. Stryer, *Biochemistry* (W.H. Freeman, New York, 1988).

71. M.D. Topal and J.R. Fresco, Nature **263**, 285 (1976).

72. M.D. Topal and J.R. Fresco, Nature **263**, 289 (1976).

73. M.J. Nowak, K. Szczepaniak, A. Barski, and D. Shugar, Z. Naturforsch **33**, 876 (1978).

74. M.R. Viant, R.S. Fellers, R.P. McLaughlin, and R.J. Saykally, J. Chem. Phys. **103**, 9502 (1995).

75. YE.D. Radchencko. A.M. Plokhotnichenko, G.G. Sheina, and YU.P. Blagoi, Biophysics **28**, 980 (1983).

76. M. Szczesniak, M.J. Nowak, H. Rostkowska, and K. Szczepaniak, W.B. Person, D. Shugar, J. Am. Chem. Soc. **105**, 5969 (1983).

77. S. Chin, I. Scott, K. Szczepaniak, and W.B. Person, J. Am. Chem. Soc. **106**, 3415 (1984).

78. A.J. Barnes, M.A. Stuckey, and L. Le Gall, Spectrochimica Acta A **40**, 419 (1984).

79. M. Graindourze, J. Smets, TH. Zeegers-Huyskens, and G. Maes, J. Mol. Struct. **222**, 345 (1990).

80. A. Lés, L. Adamowicz, M.J. Nowak, and L. Lapinski, Spectrochimica Acta A **48**, 1385 (1992).

81. A.Yu. Ivanov, A.M. Plokhotnichenko, E.D. Radchenko, G.G. Sheina, Yu.P. Blagoi, J. Mol. Struct. **372**, 91 (1995).

82. M. Nowak, J. Mol. Struct. **193**, 35 (1989).

83. W.B. Person, K. Szczepaniak, M. Szczesniak, and J.E. Del Bene, in *Recent Experimental and Computational Advances in Molecular Spectroscopy*, edited by R. Fausto (Kluwer Academic Publishers, The Netherlands, 1993), p. 141.

84. M.J. Nowak, L. Lapinski, J.S. Kwiatkowski, and J. Leszczyński, Spectrochimica Acta A **47**, 87 (1991).

85. M.J. Nowak, H. Rostkowska, L. Lapinski, J.S. Kwiatkowski, and J. Leszczyński, Spectrochimica Acta A **50**, 1081 (1994).

86. M.J. Nowak, H. Rostkowska, L. Lapinski, J.S. Kwiatkowski, and J. Leszczyński, J. Phys. Chem. **98**, 2813 (1994).

87. M.J. Nowak, L. Lapinski, J.S. Kwiatkowski, and J. Leszczyński, J. Phys. Chem. **100**, 3527 (1996).

88. I.R. Gould, M.A. Vincent, and I.H. Hillier, J. Chem Soc. Perkin Trans. **2**, 69 (1992).

89. D.A. Estrin, L. Paglieri, and G. Corongiu, J. Phys. Chem. **98**, 5653 (1994).

90. Private communication. J.B. Paul and R.J. Saykally have been studying the formation of water-NA base clusters in the gas-phase using laser diode spectroscopy.

91. J. Liquier and E. Taillandier, in *Infrared Spectroscopy of Biomolecules*, edited by H. Mantsch and D. Chapman (Wiley-Liss, New York, 1996), p. 131.

92. B.G. Segal, *Chemistry, Experiment and Theory* (John Wiley and Sons, New York, 1985).

93. G. Herzberg, *Atomic Spectra and Atomic Structure* (Dover, New York, 1944).

94. R. Page and C. Gudeman, J. Opt. Soc. Am. B. **7**, 1761 (1990).

95. L. Zhu and P. Johnson, J. Chem. Phys. **94**, 5769 (1991).

96. P. Johnson and L. Zhu, Int. J. Mass. Spectrosc. Ion. Proc. **131**, 193 (1994).

97. W. Albertson, Phys. Rev. **45**, 304 (1934).

98. W. Albertson, Phys. Rev. **53**, 940 (1938).

99. C.E. Moore, *Ionization Potentials and Ionization Limits Derived from the Analyses of Optical Spectra* (National Bureau of Standards, Washington, D.C., 1970).

100. C.E. Moore, *Atomic Energy Levels, Vol.* III (National Bureau of Standards, Washington, D.C., 1958).

101. Th.A.M. Van Kleef and P.F.A. Klickenberg, Physica **27**, 83 (1961).

102. Th.A.M. Van Kleef, Physica **23**, 843 (1957).

103. E.G. Rauh and R.J. Ackermann, J. Chem. Phys. **70**, 1004 (1979).

104. A.M. James, J.P. Kowalczyk, E. Langlois, M.D. Campbell, A. Ogawa, and B. Simard, J. Chem. Phys. **101**, 4485 (1994).

105. T.G. Dietz, D.E. Powers, M.A. Duncan, and R.E. Smalley, J. Chem. Phys. **74**, 6511 (1991).

106. D. Proch and T. Trickl, Rev. Sci. Instrum. **60**, 713 (1989).

107. M.D. Campbell-Miller and B. Simard, J. Opt. Soc. Am. B. **13**, 2115 (1996).

108. A. Marijnissen, J.J. ter Meulen, P.A. Hackett, and B. Simard, Phy. Rev. A **52**, 2606 (1995).

109. B. Simard, P. Kowalczyk, and A. M. James, Phys. Rev. A. **50**, 846 (1994).

110. E.R. Cohen and B.N. Taylor, Rev. Mod. Phys. **59**, 1121 (1987).

111. T. Ishikawai, Jpn. J. Appl. Phy. **33**, 2056 (1994).

Appendix A

H^{11}BO Line Positions

Table A.1: Rotational-vibrational line positions included in the global fit of H^{11}BO data. The O-C denotes observed-calculated. All units in cm^{-1}.

J'	J''	Obs.	O-C	J'	J''	Obs.	O-C	J'	J''	Obs.	O-C
						(100)—(000)					
1	2	2788.9253	−30.7	16	17	2747.3015	− 3.9	28	29	2711.2672	− 8.8
2	3	2786.2761	2.8	17	18	2744.3897	0.4	29	30	2708.1596	− 6.9
3	4	2783.6063	8.5	18	19	2741.4606	0.2	30	31	2705.0365	− 3.6
4	5	2780.9176	2.7	19	20	2738.5152	2.4	31	32	2701.8978	0.7
5	6	2778.2126	10.2	20	21	2735.5525	− 1.9	32	33	2698.7432	1.2
6	7	2775.4875	− 7.4	21	22	2732.5746	5.6	34	35	2692.3876	2.7
7	8	2772.7471	− 2.2	22	23	2729.5786	− 2.7	35	36	2689.1867	2.3
8	9	2769.9895	5.3	23	24	2726.5676	1.4	36	37	2685.9709	4.7
9	10	2767.2142	10.7	24	25	2723.5396	− 1.1	37	38	2682.7395	2.6
10	11	2764.4205	3.7	25	26	2720.4960	1.3	38	39	2679.4925	− 4.0
11	12	2761.6094	− 3.2	26	27	2717.4361	1.9	39	40	2676.2319	1.6
13	14	2755.9374	− 2.4	27	28	2714.3597	− 2.5	40	41	2672.9565	7.8
14	15	2753.0752	− 7.6								
2	1	2799.3590	− 1.9	20	19	2842.6549	− 3.0	37	36	2877.8681	− 3.5
3	2	2801.9235	17.1	21	20	2844.8819	2.5	38	37	2879.7636	3.4
4	3	2804.4656	− 5.4	22	21	2847.0894	4.2	39	38	2881.6386	5.1
5	4	2806.9927	4.2	23	22	2849.2775	4.2	40	39	2883.4931	− 0.3
6	5	2809.5006	4.8	24	23	2851.4468	9.0	41	40	2885.3277	− 5.3
7	6	2811.9890	− 5.0	24	23	2851.4468	9.0	42	41	2887.1418	−16.4
8	7	2814.4580	−25.7	25	24	2853.5958	4.2	43	42	2888.9377	− 9.2
9	8	2816.9122	− 8.8	26	25	2855.7252	− 3.4	44	43	2890.7124	−13.3
10	9	2819.3474	3.4	27	26	2857.8367	3.0	45	44	2892.4677	−11.2
11	10	2821.7636	11.1	28	27	2859.9279	2.3	46	45	2894.2034	− 4.1
12	11	2824.1588	− 4.7	29	28	2861.9998	2.7	47	46	2895.9173	−14.2

H^{11}BO line positions, cont'd.

J'	J"	Obs.	O-C	J'	J"	Obs.	O-C	J'	J"	Obs.	O-C
13	12	2826.5379	6.6	30	29	2864.0519	0.1	48	47	2897.6145	10.2
14	13	2828.8962	− 3.6	31	30	2866.0849	2.3	50	49	2900.9432	5.9
15	14	2831.2372	2.6	32	31	2868.0975	− 3.4	51	50	2902.5756	−12.1
16	15	2833.5570	−16.0	33	32	2870.0923	9.0	54	53	2907.3595	15.8
17	16	2835.8621	9.2	34	33	2872.0656	3.1	57	56	2911.9576	13.0
18	17	2838.1457	8.3	35	34	2874.0207	12.3	71	70	2930.9840	− 3.0
19	18	2840.4090	− 5.3								

(01^10)—(000) f-e

J'	J"	Obs.	O-C	J'	J"	Obs.	O-C	J'	J"	Obs.	O-C
1	1	753.1165	5.2	13	13	754.1988	− 7.8	23	23	756.4110	9.7
2	2	753.1407	5.6	14	14	754.3683	6.8	24	24	756.6952	0.3
3	3	753.1773	10.5	15	15	754.5475	− 0.2	25	25	756.9895	−22.9
4	4	753.2238	− 7.5	16	16	754.7385	− 8.0	26	26	757.3001	2.5
5	5	753.2843	− 5.5	17	17	754.9428	− 0.9	27	27	757.6198	6.1
6	6	753.3573	1.3	18	18	755.1589	7.1	28	28	757.9496	− 3.2
7	7	753.4412	− 4.2	19	19	755.3857	4.1	29	29	758.2931	11.1
8	8	753.5377	− 2.5	20	20	755.6244	3.3	30	30	758.6439	−13.1
10	10	753.7662	− 6.0	21	21	755.8751	6.3	32	32	759.3857	5.7
11	11	753.8988	− 2.8	22	22	756.1356	− 8.8	33	33	759.7713	− 4.0
12	12	754.0435	0.9								

(01^10)—(000) e-e

J'	J"	Obs.	O-C	J'	J"	Obs.	O-C	J'	J"	Obs.	O-C
1	2	747.8725	20.8	16	17	708.6599	0.1	30	31	672.2475	− 1.9
3	4	742.6400	29.0	17	18	706.0521	8.0	31	32	669.6577	1.6
5	6	737.4058	12.8	18	19	703.4437	0.7	32	33	667.0693	2.9
6	7	734.7886	− 1.1	20	21	698.2313	− 2.0	33	34	664.4817	− 5.2
7	8	732.1733	0.8	21	22	695.6269	− 2.0	34	35	661.8973	1.4
8	9	729.5567	−14.1	22	23	693.0240	− 0.1	35	36	659.3145	5.6
9	10	726.9434	− 1.7	23	24	690.4227	6.1	36	37	656.7329	3.6
10	11	724.3285	−10.1	24	25	687.8219	4.1	37	38	654.1534	3.6
11	12	721.7164	2.8	25	26	685.2229	6.9	39	40	648.9997	− 0.5
12	13	719.1037	3.7	26	27	682.6247	4.5	40	41	646.4263	1.7
13	14	716.4910	− 2.7	27	28	680.0283	3.9	41	42	643.8550	4.4
14	15	713.8804	3.8	28	29	677.4335	5.3	42	43	641.2849	− 2.0
15	16	711.2698	3.0								

J'	J"	Obs.	O-C	J'	J"	Obs.	O-C	J'	J"	Obs.	O-C
1	0	755.7178	−27.5	18	17	800.1271	− 8.0	33	32	839.0004	− 3.2
3	2	760.9541	6.4	19	18	802.7302	−14.5	34	33	841.5765	13.7
4	3	763.5690	− 5.4	20	19	805.3339	− 0.4	35	34	844.1466	− 3.1
5	4	766.1834	−18.5	21	20	807.9349	1.3	36	35	846.7151	− 9.0
6	5	768.8011	5.2	22	21	810.5337	− 3.5	37	36	849.2823	0.0
7	6	771.4177	22.2	23	22	813.1317	0.1	38	37	851.8462	5.1
8	7	774.0300	2.2	24	23	815.7272	− 4.6	39	38	854.4051	−11.0
9	8	776.6455	20.7	25	24	818.3216	− 1.3	40	39	856.9632	− 4.3
10	9	779.2568	3.1	26	25	820.9136	− 4.3	41	40	859.5176	− 4.1
11	10	781.8691	2.5	27	26	823.5039	− 4.2	42	41	862.0678	−13.8
12	11	784.4795	− 7.7	28	27	826.0922	− 4.1	43	42	864.6172	2.0
13	12	787.0907	− 2.2	29	28	828.6780	− 7.5	44	43	867.1622	8.0
14	13	789.7005	− 0.3	30	29	831.2624	− 3.5	45	44	869.7023	− 0.4
16	15	794.9163	− 2.8	31	30	833.8440	− 4.5	46	45	872.2411	14.2
17	16	797.5222	− 7.0								

H^{11}BO line positions, cont'd.

J'	J"	Obs.	O-C	J'	J"	Obs.	O-C	J'	J"	Obs.	O-C
						(001)—(000)					
0	1	1822.9449	9.0	22	23	1761.1310	− 3.2	43	44	1694.9940	− 0.8
2	3	1817.6594	5.7	23	24	1758.1348	0.4	44	45	1691.6818	− 0.8
3	4	1814.9906	0.2	24	25	1755.1224	− 1.0	45	46	1688.3553	− 1.8
4	5	1812.3054	0.7	25	26	1752.0942	− 4.0	46	47	1685.0145	− 3.5
5	6	1809.6029	− 1.3	26	27	1749.0511	0.0	47	48	1681.6601	0.3
6	7	1806.8837	− 1.8	27	28	1745.9929	8.3	48	49	1678.2912	− 0.5
7	8	1804.1478	− 0.9	28	29	1742.9177	0.5	49	50	1674.9081	− 4.5
8	9	1801.3950	− 0.8	29	30	1739.8274	− 4.1	50	51	1671.5124	6.1
9	10	1798.6256	− 0.3	30	31	1736.7234	7.2	51	52	1668.1009	− 4.5
10	11	1795.8394	− 0.2	31	32	1733.6024	0.6	52	53	1664.6773	1.7
11	12	1793.0367	− 0.5	32	33	1730.4677	9.6	53	54	1661.2387	− 4.7
12	13	1790.2176	0.8	33	34	1727.3161	− 0.1	54	55	1657.7873	− 3.8
13	14	1787.3817	− 1.4	34	35	1724.1505	0.9	55	56	1654.3222	− 4.1
14	15	1784.5296	− 1.3	35	36	1720.9698	0.3	56	57	1650.8448	6.5
15	16	1781.6612	− 1.6	36	37	1717.7740	− 1.7	57	58	1647.3526	2.6
16	17	1778.7764	− 3.4	37	38	1714.5639	1.2	58	59	1643.8473	0.9
17	18	1775.8757	− 1.8	38	39	1711.3387	0.3	59	60	1640.3283	− 5.4
18	19	1772.9589	− 0.6	39	40	1708.0985	− 3.3	60	61	1636.7975	2.0
19	20	1770.0262	2.6	40	41	1704.8444	− 0.3	61	62	1633.2528	0.8
20	21	1767.0770	0.4	41	42	1701.5755	0.6	62	63	1629.6954	2.0
21	22	1764.1121	0.6	42	43	1698.2921	1.2				
2	1	1830.7422	− 1.0	19	18	1871.9209	3.8	35	34	1905.8032	5.5
3	2	1833.3069	− 0.2	20	19	1874.1793	− 0.7	36	35	1907.7577	0.6
5	4	1838.3839	1.3	21	20	1876.4195	− 1.5	37	36	1909.6931	0.3
6	5	1840.8956	− 1.4	22	21	1878.6407	− 7.1	38	37	1911.6092	2.2
7	6	1843.3902	0.7	23	22	1880.8443	− 0.6	39	38	1913.5050	− 2.4
8	7	1845.8667	− 0.5	24	23	1883.0279	− 7.8	40	39	1915.3818	− 0.7
9	8	1848.3257	2.2	25	24	1885.1939	− 2.5	41	40	1917.2390	1.3
10	9	1850.7667	2.5	26	25	1887.3408	0.0	42	41	1919.0760	0.5
11	10	1853.1894	− 0.9	27	26	1889.4684	− 2.0	43	42	1920.8942	9.0
12	11	1855.5944	− 0.8	28	27	1891.5770	− 3.2	44	43	1922.6906	− 1.7
13	12	1857.9816	2.2	29	28	1893.6669	− 1.5	45	44	1924.4679	− 4.2
14	13	1860.3496	− 7.0	30	29	1895.7377	− 0.6	46	45	1926.2259	− 0.1
15	14	1862.7008	− 1.1	31	30	1897.7897	4.2	47	46	1927.9638	2.9
16	15	1865.0333	− 0.8	32	31	1899.8218	2.0	48	47	1929.6818	8.9
17	16	1867.3474	− 0.7	33	32	1901.8348	2.4	51	50	1934.7115	− 7.4
18	17	1869.6433	0.5								
						(01^{1}1)—(01^{1}0) e-e					
1	2	1823.8069	− 0.5	22	23	1764.5527	4.4	43	44	1698.2107	− 0.4
2	3	1821.1554	1.2	23	24	1761.5490	1.3	44	45	1694.8858	− 0.1
3	4	1818.4862	0.7	24	25	1758.5294	0.0	45	46	1691.5461	− 2.8
4	5	1815.7996	− 0.9	25	26	1755.4942	1.8	46	47	1688.1931	5.1
5	6	1813.0964	4.5	26	27	1752.4429	2.0	47	48	1684.8231	−11.8
6	7	1810.3751	1.1	27	28	1749.3754	− 2.3	48	49	1681.4416	− 1.3
7	8	1807.6371	2.4	29	30	1743.1946	2.1	49	50	1678.0452	2.0
8	9	1804.8816	− 0.3	30	31	1740.0812	9.2	50	51	1674.6343	1.3
10	11	1799.3202	− 0.5	31	32	1736.9505	− 2.4	51	52	1671.2094	1.8
11	12	1796.5143	0.7	32	33	1733.8058	0.8	52	53	1667.7697	− 5.7
12	13	1793.6915	1.8	33	34	1730.6455	2.0	53	54	1664.3176	2.2

H^{11}BO line positions, cont'd.

J'	J"	Obs.	O-C	J'	J"	Obs.	O-C	J'	J"	Obs.	O-C
13	14	1790.8517	− 0.3	34	35	1727.4697	1.8	54	55	1660.8515	8.0
14	15	1787.9947	− 7.2	35	36	1724.2786	0.7	55	56	1657.3712	9.3
15	16	1785.1225	0.2	36	37	1721.0724	− 0.4	56	57	1653.8761	− 0.2
16	17	1782.2330	0.0	37	38	1717.8511	− 0.8	57	58	1650.3686	2.7
17	18	1779.3269	− 0.9	38	39	1714.6148	− 1.1	58	59	1646.8473	2.1
18	19	1776.4047	0.9	39	40	1711.3639	1.5	59	60	1643.3120	− 4.1
19	20	1773.4660	1.0	40	41	1708.0985	9.1	60	61	1639.7641	− 1.4
20	21	1770.5109	− 0.4	41	42	1704.8161	− 6.4	61	62	1636.2024	− 5.8
21	22	1767.5398	1.3	42	43	1701.5212	1.4	63	64	1629.0409	2.4
2	1	1834.2378	− 4.6	18	17	1873.0851	1.2	33	32	1905.1520	6.1
4	3	1839.3479	0.3	19	18	1875.3561	− 1.8	34	33	1907.1335	− 7.5
5	4	1841.8760	2.3	20	19	1877.6086	− 1.0	36	35	1911.0412	4.3
6	5	1844.3863	4.2	21	20	1879.8426	3.4	37	36	1912.9642	− 2.2
7	6	1846.8779	− 0.8	22	21	1882.0575	6.5	38	37	1914.8674	− 7.3
8	7	1849.3521	1.7	23	22	1884.2523	− 1.4	41	40	1920.4611	14.2
9	8	1851.8079	0.8	24	23	1886.4292	1.3	42	41	1922.2842	8.3
10	9	1854.2461	6.1	25	24	1888.5866	0.3	43	42	1924.0861	− 9.6
11	10	1856.6651	1.1	26	25	1890.7248	− 0.9	44	43	1925.8716	11.9
12	11	1859.0658	− 3.8	27	26	1892.8440	0.3	47	46	1931.0983	− 8.6
13	12	1861.4492	2.8	28	27	1894.9433	− 4.3	48	47	1932.7998	−14.9
14	13	1863.8126	− 6.4	29	28	1897.0233	− 8.5	50	49	1936.1454	11.3
15	14	1866.1587	− 3.7	30	29	1899.0855	2.6	52	51	1939.4060	9.5
16	15	1868.4858	− 5.6	31	30	1901.1272	3.8	53	52	1941.0031	−13.6
17	16	1870.7954	3.5								

$(01^1 1)$—$(01^1 0)$ f-f

J'	J"	Obs.	O-C	J'	J"	Obs.	O-C	J'	J"	Obs.	O-C
1	2	1823.7840	9.9	22	23	1764.3757	− 0.6	42	43	1701.3973	− 0.1
2	3	1821.1197	− 2.8	23	24	1761.3698	− 0.5	43	44	1698.0962	2.3
3	4	1818.4401	1.9	24	25	1758.3479	− 5.4	44	45	1694.7803	− 4.0
4	5	1815.7429	0.3	25	26	1755.3117	0.5	45	46	1691.4516	− 1.5
5	6	1813.0293	4.3	26	27	1752.2594	0.8	46	47	1688.1090	− 0.5
6	7	1810.2978	− 3.6	27	28	1749.1927	8.7	47	48	1684.7517	−10.0
7	8	1807.5505	− 1.8	28	29	1746.1092	1.6	48	49	1681.3828	− 0.3
8	9	1804.7864	− 1.2	29	30	1743.0114	2.6	49	50	1677.9995	0.5
9	10	1802.0043	−13.5	30	31	1739.8983	0.9	50	51	1674.6023	− 5.8
10	11	1799.2090	6.5	31	32	1736.7705	2.2	51	52	1671.1931	1.3
11	12	1796.3934	−11.4	32	33	1733.6276	2.1	52	53	1667.7697	− 2.5
12	13	1793.5644	0.6	34	35	1727.2976	2.1	53	54	1664.3337	− 1.3
13	14	1790.7178	0.3	35	36	1724.1108	5.2	54	55	1660.8847	− 1.4
14	15	1787.8552	2.2	36	37	1720.9087	1.1	55	56	1657.4227	− 1.8
15	16	1784.9768	8.2	37	38	1717.6923	− 1.7	56	57	1653.9490	6.7
16	17	1782.0808	− 0.4	38	39	1714.4621	1.7	58	59	1646.9618	5.9
17	18	1779.1689	− 7.5	39	40	1711.2169	− 1.7	59	60	1643.4498	8.6
18	19	1776.2430	4.1	40	41	1707.9581	1.9	60	61	1639.9246	2.6
19	20	1773.2996	1.2	41	42	1704.6842	− 4.3	62	63	1632.8377	− 9.6
20	21	1770.3406	− 0.9								
2	1	1834.2630	− 7.5	17	16	1871.0603	1.4	34	33	1907.7811	− 2.6
3	2	1836.8426	19.0	18	17	1873.3684	− 8.7	35	34	1909.7712	1.4
4	3	1839.4002	0.0	19	18	1875.6598	− 2.0	36	35	1911.7414	− 1.8
5	4	1841.9424	0.7	20	19	1877.9311	−12.1	37	36	1913.6943	15.5

H^{11}BO line positions, cont'd.

J'	J"	Obs.	O-C	J'	J"	Obs.	O-C	J'	J"	Obs.	O-C
6	5	1844.4666	− 2.2	21	20	1880.1864	2.9	38	37	1915.6251	5.0
7	6	1846.9736	− 1.1	22	21	1882.4214	− 0.6	39	38	1917.5369	− 1.6
8	7	1849.4630	0.8	23	22	1884.6379	− 3.2	41	40	1921.3052	14.5
9	8	1851.9346	1.8	24	23	1886.8362	− 1.9	42	41	1923.1565	−14.2
10	9	1854.3877	− 3.9	26	25	1891.1764	− 0.8	43	42	1924.9943	18.4
11	10	1856.8236	− 2.4	27	26	1893.3179	− 5.3	45	44	1928.6024	− 3.9
12	11	1859.2419	1.0	28	27	1895.4416	1.0	47	46	1932.1348	3.0
13	12	1861.6419	2.2	29	28	1897.5453	− 4.2	48	47	1933.8702	− 5.2
14	13	1864.0237	2.2	30	29	1899.6304	− 5.1	50	49	1937.2848	7.8
15	14	1866.3882	9.1	31	30	1901.6979	7.4	51	50	1938.9598	−11.7
16	15	1868.7330	2.0	32	31	1903.7441	− 2.6	52	51	1940.6183	2.8

(11^{1}0)—(01^{1}0) e-e

J'	J"	Obs.	O-C	J'	J"	Obs.	O-C	J'	J"	Obs.	O-C
3	4	2767.2142	−27.8	14	15	2736.7179	−11.7	25	26	2704.2079	1.0
4	5	2764.5303	0.9	15	16	2733.8443	− 8.7	27	28	2698.0899	16.0
5	6	2761.8277	16.2	16	17	2730.9555	7.5	28	29	2695.0044	− 6.4
6	7	2759.1041	− 5.7	17	18	2728.0478	− 0.3	29	30	2691.9067	3.2
7	8	2756.3671	11.1	18	19	2725.1245	1.0	30	31	2688.7920	− 1.6
8	9	2753.6105	3.3	19	20	2722.1848	0.3	31	32	2685.6623	− 3.2
9	10	2750.8374	1.8	20	21	2719.2288	0.0	32	33	2682.5180	2.0
10	11	2748.0474	0.6	21	22	2716.2572	5.3	33	34	2679.3571	− 6.2
11	12	2745.2414	9.1	22	23	2713.2692	8.2	34	35	2676.1832	6.2
12	13	2742.4163	− 5.3	23	24	2710.2636	− 5.2	35	36	2672.9905	−19.1
13	14	2739.5761	− 2.0								

J'	J"	Obs.	O-C	J'	J"	Obs.	O-C	J'	J"	Obs.	O-C
4	3	2788.0751	−32.8	19	18	2824.0743	− 7.2	35	34	2857.8109	− 2.9
5	4	2790.6058	− 2.1	20	19	2826.3268	2.2	36	35	2859.7568	11.3
6	5	2793.1136	−19.7	21	20	2828.5593	1.8	37	36	2861.6806	0.7
6	5	2793.1136	−19.7	22	21	2830.7734	4.5	38	37	2863.5854	− 4.3
7	6	2795.6089	18.8	23	22	2832.9673	− 4.4	39	38	2865.4713	− 1.7
8	7	2798.0804	− 1.1	24	23	2835.1442	7.0	41	40	2869.1883	45.6
9	8	2800.5343	−13.6	25	24	2837.3001	− 2.0	42	41	2871.0108	5.7
10	9	2802.9729	2.3	26	25	2839.4385	4.8	43	42	2872.8164	− 5.9
11	10	2805.3945	32.0	29	28	2845.7363	1.0	44	43	2874.6044	4.6
12	11	2807.7906	−10.0	30	29	2847.7982	10.8	46	45	2878.1159	−23.9
14	13	2812.5376	6.6	31	30	2849.8377	− 9.8	47	46	2879.8468	12.2
15	14	2814.8814	− 3.7	32	31	2851.8601	− 8.0	48	47	2881.5529	− 0.3
16	15	2817.2087	5.6	33	32	2853.8630	− 7.6	49	48	2883.2407	4.6
17	16	2819.5153	− 5.3	34	33	2855.8477	4.3	50	49	2884.9073	− 3.1
18	17	2821.8056	7.7								

(11^{1}0)—(01^{1}0) f-f

J'	J"	Obs.	O-C	J'	J"	Obs.	O-C	J'	J"	Obs.	O-C
3	4	2767.1683	− 1.2	15	16	2733.6514	1.9	26	27	2700.8290	− 9.9
4	5	2764.4711	15.8	16	17	2730.7476	−10.8	27	28	2697.7507	1.8
6	7	2759.0223	26.6	18	19	2724.8918	−24.3	28	29	2694.6593	38.0
7	8	2756.2690	2.3	19	20	2721.9434	8.8	29	30	2691.5446	− 3.5
8	9	2753.5006	− 2.5	20	21	2718.9753	7.3	30	31	2688.4199	10.0
9	10	2750.7153	− 5.5	21	22	2715.9892	−12.1	31	32	2685.2776	0.0
10	11	2747.9140	1.4	22	23	2712.9905	3.3	32	33	2682.1212	2.5
11	12	2745.0947	− 1.3	23	24	2709.9731	− 8.3	33	34	2678.9491	− 0.7
12	13	2742.2597	6.2	24	25	2706.9431	13.2	34	35	2675.7633	9.4

H¹¹BO line positions, cont'd.

J'	J"	Obs.	O-C	J'	J"	Obs.	O-C	J'	J"	Obs.	O-C
13	14	2739.4066	1.7	25	26	2703.8942	4.4	35	36	2672.5588	−18.0
14	15	2736.5366	− 4.9								
3	2	2785.5681	−11.7	20	19	2826.5657	− 4.8	35	34	2858.2228	14.4
4	3	2788.1261	− 8.1	21	20	2828.8096	− 8.7	36	35	2860.1772	4.5
5	4	2790.6650	−15.5	22	21	2831.0370	10.8	37	36	2862.1103	−22.5
6	5	2793.1882	− 0.6	23	22	2833.2424	1.2	38	37	2864.0280	− 7.2
7	6	2795.6912	− 6.6	24	23	2835.4294	− 2.6	39	38	2865.9242	− 9.8
8	7	2798.1783	10.4	25	24	2837.5982	2.5	40	39	2867.8005	−15.3
9	8	2800.6437	− 8.1	26	25	2839.7460	−11.7	41	40	2869.6615	24.6
10	9	2803.0955	20.1	27	26	2841.8768	− 3.6	42	41	2871.4970	8.1
11	10	2805.5254	12.4	28	27	2843.9876	− 2.9	43	42	2873.3162	24.8
12	11	2807.9379	14.6	29	28	2846.0783	−11.3	44	43	2875.1107	− 5.0
14	13	2812.7057	0.6	30	29	2848.1518	2.1	45	44	2876.8877	−12.3
15	14	2815.0636	11.1	31	30	2850.2041	− 3.2	46	45	2878.6441	−26.4
16	15	2817.4010	3.8	32	31	2852.2386	7.2	47	46	2880.3863	16.5
17	16	2819.7201	− 0.8	33	32	2854.2512	− 6.5	49	48	2883.8016	11.9
18	17	2822.0205	− 4.9	34	33	2856.2466	2.6	50	49	2885.4774	− 8.8
19	18	2824.3030	− 0.1								

(002)—(001)

J'	J"	Obs.	O-C	J'	J"	Obs.	O-C	J'	J"	Obs.	O-C
0	1	1806.7896	17.7	21	22	1748.3184	0.6	41	42	1686.1322	4.2
1	2	1804.1709	− 1.7	22	23	1745.3551	1.4	42	43	1682.8661	− 2.3
2	3	1801.5372	0.0	23	24	1742.3772	15.4	43	44	1679.5864	0.1
3	4	1798.8872	9.2	24	25	1739.3809	1.5	44	45	1676.2934	11.7
4	5	1796.2182	− 0.6	25	26	1736.3703	2.0	45	46	1672.9841	1.1
6	7	1790.8315	1.0	26	27	1733.3441	1.0	46	47	1669.6613	− 1.9
8	9	1785.3766	− 4.8	27	28	1730.3025	1.9	47	48	1666.3254	3.6
9	10	1782.6243	− 5.9	28	29	1727.2456	2.9	48	49	1662.9744	− 2.3
10	11	1779.8551	− 8.6	29	30	1724.1734	5.7	49	50	1659.6112	8.1
11	12	1777.0704	− 1.6	30	31	1721.0855	3.4	50	51	1656.2323	0.2
12	13	1774.2683	− 2.0	31	32	1717.9825	3.6	51	52	1652.8401	− 3.2
13	14	1771.4495	− 6.1	32	33	1714.8645	4.1	52	53	1649.4351	1.0
14	15	1768.6154	1.4	34	35	1708.5807	−21.0	53	54	1646.0157	− 3.2
15	16	1765.7640	− 1.7	35	36	1705.4190	− 7.3	54	55	1642.5844	8.5
16	17	1762.8964	− 2.8	36	37	1702.2419	1.3	55	56	1639.1375	− 1.3
17	18	1760.0126	− 5.2	37	38	1699.0490	− 1.0	56	57	1635.6777	− 7.3
18	19	1757.1138	3.8	38	39	1695.8420	3.7	57	58	1632.2064	3.8
19	20	1754.1976	− 1.0	39	40	1692.6201	5.5	58	59	1628.7200	− 4.9
20	21	1751.2659	− 0.9	40	41	1689.3805	−24.5	59	60	1625.2221	2.9
1	0	1811.9696	1.9	14	13	1843.9341	− 3.4	28	27	1874.9206	3.4
2	1	1814.5338	− 4.4	15	14	1846.2678	0.4	29	28	1876.9930	1.2
3	2	1817.0819	3.3	16	15	1848.5828	− 0.9	30	29	1879.0467	1.6
4	3	1819.6118	3.4	17	16	1850.8794	− 3.1	32	31	1883.0970	5.8
5	4	1822.1231	− 6.6	18	17	1853.1580	− 1.8	33	32	1885.0928	2.5
6	5	1824.6196	11.3	19	18	1855.4179	− 2.9	34	33	1887.0700	5.8
7	6	1827.0950	− 5.0	20	19	1857.6595	− 2.6	36	35	1890.9650	− 0.9
8	7	1829.5544	− 4.1	21	20	1859.8823	− 5.4	37	36	1892.8840	1.7
9	8	1831.9958	− 4.2	22	21	1862.0874	1.1	38	37	1894.7824	− 6.2
10	9	1834.4210	11.7	23	22	1864.2731	1.0	39	38	1896.6626	− 1.9
11	10	1836.8252	− 3.7	24	23	1866.4400	− 1.6	40	39	1898.5229	− 0.5

$H^{11}BO$ line positions, cont'd.

J'	J"	Obs.	O-C	J'	J"	Obs.	O-C	J'	J"	Obs.	O-C
12	11	1839.2131	− 1.7	25	24	1868.5887	2.2	41	40	1900.3630	− 4.0
13	12	1841.5826	− 2.4								

Table A.2: (01^12)—(01^11) rotational-vibrational line positions (Tentative). The O-C denotes observed-calculated. All units in cm^{-1}.

J'	J''	Obs.	O-C	J'	J''	Obs.	O-C	J'	J''	Obs.	O-C
						e—e					
2	3	1804.9740	−25.1	20	21	1754.5175	−1.7	40	41	1692.5218	−5.9
3	4	1802.3130	−8.1	21	22	1751.5633	18.8	41	42	1689.2692	−6.9
4	5	1799.6333	−8.6	22	23	1748.5905	8.7	42	43	1686.0033	−2.2
5	6	1796.9373	−3.9	23	24	1745.6028	5.4	43	44	1682.7216	−15.9
6	7	1794.2244	−0.2	24	25	1742.5955	−40.3	44	45	1679.4285	−7.4
7	8	1791.4944	−1.0	25	26	1739.5817	3.6	45	46	1676.1196	−20.6
8	9	1788.7466	−13.9	26	27	1736.5492	12.4	46	47	1672.7993	−12.4
10	11	1783.2047	−4.7	27	28	1733.5002	8.8	47	48	1669.4652	−7.3
11	12	1780.4087	−4.6	28	29	1730.4368	12.3	48	49	1666.1151	−28.5
12	13	1777.5966	−0.6	29	30	1727.3584	15.4	49	50	1662.7546	−21.5
13	14	1774.7680	0.1	30	31	1724.2634	2.5	50	51	1659.3815	−8.0
14	15	1771.9232	0.5	31	32	1721.1567	21.3	51	52	1655.9960	11.7
15	16	1769.0626	4.8	32	33	1718.0315	3.5	52	53	1652.5959	14.1
16	17	1766.1860	9.5	33	34	1714.8937	5.3	53	54	1649.1817	5.5
17	18	1763.2919	−0.6	36	37	1705.3927	11.0	54	55	1645.7556	5.4
18	19	1760.3837	7.1	37	38	1702.1954	−2.7	55	56	1642.3178	14.9
19	20	1757.4591	8.7	38	39	1698.9839	−15.1	56	57	1638.8689	39.9
2	1	1818.0372	31.7	16	15	1852.2701	12.9	29	28	1880.8795	6.2
3	2	1820.5932	−6.6	17	16	1854.5805	6.0	31	30	1885.0005	−4.4
4	3	1823.1369	5.6	18	17	1856.8736	7.0	32	31	1887.0336	0.4
7	6	1830.6589	0.1	19	18	1859.1482	6.7	33	32	1889.0478	5.2
8	7	1833.1314	1.1	20	19	1861.4048	8.2	34	33	1891.0431	11.0
9	8	1835.5868	8.2	21	20	1863.6413	−6.9	35	34	1893.0177	0.3
10	9	1838.0226	−3.1	22	21	1865.8619	3.7	36	35	1894.9738	−4.5
11	10	1840.4457	35.9	23	22	1868.0640	13.3	37	36	1896.9120	2.8
12	11	1842.8438	3.8	25	24	1872.4082	−11.6	38	37	1898.8304	4.7
13	12	1845.2272	4.8	26	25	1874.5543	−5.2	39	38	1900.7292	2.7
14	13	1847.5926	4.3	27	26	1876.6805	−10.9	40	39	1902.6087	−0.3
15	14	1849.9399	4.0	28	27	1878.7864	−31.8	41	40	1904.4679	−13.2
						f—f					
2	3	1805.0109	−18.2	21	22	1751.7335	−5.7	38	39	1699.1170	−1.8
4	5	1799.6911	−14.2	22	23	1748.7654	9.0	39	40	1695.8847	2.1
5	6	1797.0071	7.2	23	24	1745.7793	3.3	40	41	1692.6369	0.2
6	7	1794.3021	−10.3	24	25	1742.7774	−0.7	42	43	1686.0974	−1.6
7	8	1791.5829	2.0	25	26	1739.7602	2.1	43	44	1682.8067	8.0
8	9	1788.8449	−2.3	26	27	1736.7234	−32.5	44	45	1679.5001	2.6
9	10	1786.0905	−1.0	27	28	1733.6787	11.5	45	46	1676.1791	−1.3
10	11	1783.3198	6.7	28	29	1730.6117	−11.4	46	47	1672.8442	0.2
11	12	1780.5325	17.0	29	30	1727.5322	−2.1	47	48	1669.4943	−6.1
12	13	1777.7250	−6.6	30	31	1724.4352	−12.2	48	49	1666.1305	−8.9
13	14	1774.9036	−1.8	31	32	1721.3246	−3.8	49	50	1662.7546	8.3
14	15	1772.0647	−5.0	32	33	1718.1986	5.0	50	51	1659.3595	−24.4
16	17	1766.3379	−4.1	33	34	1715.0561	2.2	51	52	1655.9571	8.3
17	18	1763.4501	−0.5	34	35	1711.8988	4.4	52	53	1652.5353	−13.0
18	19	1760.5454	−1.4	35	36	1708.7257	−0.1	53	54	1649.1051	20.6
19	20	1757.6256	9.6	36	37	1705.5395	16.4	54	55	1645.6562	4.2
20	21	1754.6872	−1.7								

H^{11}BO line positions, cont'd.

J'	J"	Obs.	O-C	J'	J"	Obs.	O-C	J'	J"	Obs.	O-C
2	1	1818.0061	−16.2	16	15	1852.0070	−36.1	29	28	1880.3273	26.0
3	2	1820.5545	7.2	17	16	1854.3016	− 3.0	30	29	1882.3677	−11.5
4	3	1823.0813	− 7.0	18	17	1856.5749	4.0	31	30	1884.3941	6.0
5	4	1825.5920	− 4.0	19	18	1858.8276	− 8.2	32	31	1886.3991	4.1
6	5	1828.0861	11.6	20	19	1861.0619	−16.3	33	32	1888.3850	7.0
7	6	1830.5591	− 3.3	21	20	1863.2802	4.3	34	33	1890.3512	8.2
8	7	1833.0165	6.0	22	21	1865.4774	2.6	35	34	1892.2963	− 4.6
9	8	1835.4538	− 5.2	23	22	1867.6551	− 5.3	36	35	1894.2240	5.4
10	9	1837.8762	17.7	24	23	1869.8152	1.9	37	36	1896.1303	− 0.4
11	10	1840.2752	−12.3	25	24	1871.9548	− 5.6	39	38	1899.8839	− 8.2
12	11	1842.6599	− 1.9	26	25	1874.0768	2.4	41	40	1903.5606	11.4
13	12	1845.0244	− 9.7	27	26	1876.1777	− 8.5	43	42	1907.1545	4.9
14	13	1847.3719	− 4.0	28	27	1878.2619	6.5	46	45	1912.3909	−36.8
15	14	1849.7000	− 6.6								

Table A.3: $(02^{0,2}0)$—(01^10) line positions for H^{11}BO. The O-C denotes observed-calculated. All units in cm^{-1}.

J'	J''	Obs.	O-C	J'	J''	Obs.	O-C	J'	J''	Obs.	O-C
					(02^00)—(01^10) e—e						
0	1	752.0112	52.9	16	17	709.9343	26.5	29	30	675.8415	6.5
1	2	749.3777	10.4	17	18	707.3036	−7.3	30	31	673.2264	5.5
2	3	746.7481	10.3	18	19	704.6794	18.0	31	32	670.6136	12.7
3	4	744.1101	−71.0	20	21	699.4275	12.8	33	34	665.3891	−2.0
4	5	741.4828	−43.0	21	22	696.8019	1.7	34	35	662.7814	14.4
5	6	738.8573	3.9	22	23	694.1795	13.6	35	36	660.1727	4.6
8	9	730.9658	0.1	23	24	691.5563	9.2	36	37	657.5665	3.5
9	10	728.3331	−25.3	24	25	688.9337	1.7	37	38	654.9609	−7.8
10	11	725.7026	−29.4	25	26	686.3134	6.7	38	39	652.3592	4.0
11	12	723.0770	14.0	26	27	683.6941	10.9	39	40	649.7581	3.1
12	13	720.4458	−2.8	27	28	681.0746	1.0	41	42	644.5615	2.4
13	14	717.8158	−10.0	28	29	678.4571	1.1	42	43	641.9647	−11.0
3	2	762.5219	39.2	17	16	799.1969	22.7	33	32	840.6912	1.2
4	3	765.1451	6.5	19	18	804.4130	12.9	34	33	843.2634	2.5
5	4	767.7735	32.8	21	20	809.6215	−0.6	35	34	845.8333	11.0
6	5	770.3954	2.6	22	21	812.2243	8.2	36	35	848.3988	6.1
7	6	773.0212	20.6	23	22	814.8225	−8.4	37	36	850.9604	−5.6
8	7	775.6419	−3.1	24	23	817.4207	−3.2	38	37	853.5202	−4.0
9	8	778.2668	25.4	25	24	820.0167	1.6	39	38	856.0763	−5.9
10	9	780.8849	−3.4	26	25	822.6104	6.5	40	39	858.6296	−2.9
11	10	783.5058	8.7	27	26	825.2009	3.9	41	40	861.1792	−2.7
12	11	786.1242	7.3	28	27	827.7895	6.2	42	41	863.7275	20.6
13	12	788.7400	−5.7	29	28	830.3754	7.0	43	42	866.2661	−18.5
14	13	791.3565	1.4	30	29	832.9587	7.8	44	43	868.8068	1.1
15	14	793.9723	15.6	31	30	835.5391	7.0	45	44	871.3406	−12.4
16	15	796.5839	4.9								
					(02^20)—(01^10) f—f						
0	1	752.0189	8.5	17	18	709.5761	−10.9	29	30	682.9554	26.4
2	3	746.8233	33.3	18	19	707.2287	−7.1	30	31	680.9055	10.1
6	7	736.5720	19.7	19	20	704.9008	−17.8	31	32	678.8844	−4.9
7	8	734.0418	20.9	21	22	700.3141	−6.6	32	33	676.8950	7.4
9	10	729.0218	14.4	22	23	698.0530	−24.5	33	34	674.9333	3.0
10	11	726.5362	39.1	23	24	695.8191	−10.0	35	36	671.0982	−6.4
12	13	721.6031	7.3	24	25	693.6088	−8.9	36	37	669.2265	2.4
14	15	716.7380	−0.9	25	26	691.4230	−17.8	38	39	665.5696	−4.2
15	16	714.3314	−9.0	26	27	689.2624	−35.9	39	40	663.7833	−28.0
16	17	711.9444	−7.0								
2	1	759.9031	1.3	15	14	795.3680	−7.3	28	27	833.6792	−6.6
3	2	762.5500	−46.6	16	15	798.1964	−18.7	29	28	836.7822	2.2
4	3	765.2166	−15.3	17	16	801.0439	−10.6	30	29	839.9086	−1.5
5	4	767.8954	19.1	19	18	806.7887	−39.0	31	30	843.0597	−6.2
6	5	770.5820	9.7	20	19	809.6917	−31.2	32	31	846.2386	17.6
7	6	773.2792	−16.5	21	20	812.6168	−2.1	33	32	849.4393	8.9
8	7	775.9887	−46.0	22	21	815.5577	−18.7	34	33	852.6658	6.4

H^{11}BO line positions, cont'd.

J'	J"	Obs.	O-C	J'	J"	Obs.	O-C	J'	J"	Obs.	O-C
9	8	778.7195	7.4	23	22	818.5204	−30.0	35	34	855.9209	38.3
10	9	781.4562	−13.9	24	23	821.5063	−26.5	36	35	859.1939	− 1.0
11	10	784.2109	7.3	25	24	824.5141	−26.9	37	36	862.4949	−11.0
12	11	786.9759	−11.4	26	25	827.5465	−11.2	38	37	865.8229	1.7
13	12	789.7586	− 1.6	27	26	830.6010	− 8.2	39	38	869.1760	20.3
14	13	792.5551	− 7.4								

$(02^{2}0)$—$(01^{1}0)$ e—e

J'	J"	Obs.	O-C	J'	J"	Obs.	O-C	J'	J"	Obs.	O-C
0	1	735.0900	− 7.3	15	16	697.2310	0.7	27	28	668.1123	47.0
3	4	727.3154	4.0	16	17	694.7846	15.2	28	29	665.6875	5.0
4	5	724.7466	−10.1	17	18	692.3421	5.5	29	30	663.2649	3.5
5	6	722.1921	− 2.4	18	19	689.9070	15.3	30	31	660.8382	−16.3
6	7	719.6489	− 1.1	19	20	687.4761	19.5	31	32	658.4119	− 4.2
7	8	717.1161	−11.0	20	21	685.0494	24.4	32	33	655.9806	−12.4
8	9	714.5942	−25.0	21	22	682.6247	18.1	33	34	653.5474	− 7.8
9	10	712.0857	−13.3	22	23	680.2032	16.8	34	35	651.1096	−15.2
10	11	709.5874	− 5.0	23	24	677.7831	12.6	35	36	648.6690	−14.6
11	12	707.0976	−11.9	24	25	675.3647	14.1	36	37	646.2239	−23.1
12	13	704.6197	6.5	25	26	672.9463	11.4	37	38	643.7777	− 6.7
14	15	699.6856	− 1.9	26	27	670.5278	9.7	38	39	641.3261	− 7.7

J'	J"	Obs.	O-C	J'	J"	Obs.	O-C	J'	J"	Obs.	O-C
1	0	740.3412	47.8	21	20	794.9276	24.5	36	35	836.1917	−23.0
4	3	748.2991	32.8	22	21	797.7069	12.1	37	36	838.8899	−10.8
7	6	756.3582	− 1.2	23	22	800.4879	28.2	38	37	841.5765	−31.6
8	7	759.0654	−15.3	24	23	803.2626	0.6	39	38	844.2599	0.7
10	9	764.5133	1.7	25	24	806.0388	15.2	40	39	846.9322	6.0
11	10	767.2428	−66.7	26	25	808.8087	2.4	41	40	849.5967	16.9
12	11	769.9900	−38.2	27	26	811.5763	9.6	42	41	852.2491	−10.2
13	12	772.7439	−15.4	28	27	814.3369	− 4.8	43	42	854.8995	24.5
14	13	775.4994	−41.5	29	28	817.0934	− 3.6	44	43	857.5388	28.0
15	14	778.2668	− 6.7	30	29	819.8438	− 2.8	45	44	860.1690	20.9
16	15	781.0368	4.7	31	30	822.5867	−10.7	46	45	862.7920	17.3
17	16	783.8096	2.6	32	31	825.3232	−12.2	47	46	865.4077	16.2
18	17	786.5861	5.2	33	32	828.0519	−17.6	48	47	868.0133	−11.9
19	18	789.3650	7.2	34	33	830.7740	−11.9	49	48	870.6137	−22.6
20	19	792.1459	15.4								

Appendix B

H^{10}BO Line Positions

Table B.1: Rotational-vibrational line positions included in the global fit of H^{10}BO data. The O-C denotes observed - calculated. All units in cm^{-1}.

J'	J''	Obs.	O-C	J'	J''	Obs.	O-C	J'	J''	Obs.	O-C
						(100)					
0	1	2815.0193	36.4	14	15	2775.0610	0.1	27	28	2734.6449	−16.1
1	2	2812.2916	27.5	15	16	2772.0626	− 4.6	28	29	2731.4115	5.1
2	3	2809.5458	36.2	16	17	2769.0455	− 8.4	29	30	2728.1566	−12.0
3	4	2806.7743	−14.6	17	18	2766.0126	17.4	30	31	2724.8915	44.3
4	5	2803.9905	8.1	18	19	2762.9570	1.4	31	32	2721.5989	− 0.5
5	6	2801.1870	31.1	19	20	2759.8837	− 5.9	32	33	2718.2929	− 4.7
6	7	2798.3609	23.6	20	21	2756.7896	−35.8	33	34	2714.9710	4.7
7	8	2795.5158	20.4	21	22	2753.6832	− 5.6	34	35	2711.6305	− 0.2
8	9	2792.6483	−12.6	22	23	2750.5558	− 2.7	35	36	2708.2731	− 2.5
9	10	2789.7645	−15.2	23	24	2747.4112	9.9	36	37	2704.8999	6.5
10	11	2786.8613	−19.5	24	25	2744.2470	7.5	37	38	2701.5079	− 3.6
11	12	2783.9427	15.0	25	26	2741.0646	3.9	40	41	2691.2355	4.3
12	13	2780.9983	−18.0	26	27	2737.8637	− 5.6	42	43	2684.2982	−54.4
13	14	2778.0387	−13.6								
3	2	2825.7248	17.9	19	18	2865.2847	7.5	32	31	2893.4579	− 8.1
4	3	2828.3482	−14.1	20	19	2867.5793	− 0.7	33	32	2895.4746	− 5.8
5	4	2830.9575	15.9	21	20	2869.8534	− 1.4	34	33	2897.4687	−11.4
7	6	2836.1066	− 9.0	22	21	2872.1055	−10.5	35	34	2899.4401	−26.3
8	7	2838.6514	−13.3	23	22	2874.3387	4.4	36	35	2901.3915	−23.1
9	8	2841.1784	9.4	24	23	2876.5491	4.6	37	36	2903.3230	0.2
11	10	2846.1676	25.2	25	24	2878.7365	−12.0	38	37	2905.2310	8.1
12	11	2848.6278	− 0.5	26	25	2880.9044	− 9.0	39	38	2907.1160	4.5
13	12	2851.0697	− 3.0	27	26	2883.0509	− 5.3	41	40	2910.8252	51.0
14	13	2853.4916	2.6	28	27	2885.1743	−18.2	42	41	2912.6406	12.2
15	14	2855.8920	3.1	29	28	2887.2792	0.1	44	43	2916.2117	0.8
16	15	2858.2721	7.7	30	29	2889.3558	−48.7	45	44	2917.9669	25.0
17	16	2860.6306	7.2								

H^{10}BO line positions, cont'd.

J'	J"	Obs.	O-C	J'	J"	Obs.	O-C	J'	J"	Obs.	O-C
						(01^{1}0) *e-e*					
1	2	756.8559	3.7	18	19	710.9747	−3.4	31	32	676.1752	25.3
4	5	748.7381	−13.9	19	20	708.2890	17.2	32	33	673.5111	16.8
5	6	746.0339	−15.1	21	22	702.9154	−10.9	33	34	670.8484	−1.0
6	7	743.3335	13.6	22	23	700.2317	−19.7	34	35	668.1926	27.3
7	8	740.6310	13.1	23	24	697.5537	11.1	35	36	665.5348	12.9
10	11	732.5323	43.2	24	25	694.8713	−20.1	36	37	662.8748	−46.2
11	12	729.8323	28.6	25	26	692.1979	21.2	37	38	660.2279	0.9
13	14	724.4392	32.7	26	27	689.5221	18.3	38	39	657.5793	6.8
14	15	721.7416	5.6	27	28	686.8482	15.6	39	40	654.9310	−8.5
15	16	719.0471	−3.6	28	29	684.1749	−0.9	40	41	652.2872	−4.5
16	17	716.3554	1.7	29	30	681.5034	−21.0	41	42	649.6457	−3.3
17	18	713.6628	−15.8	30	31	678.8374	−6.0	44	45	641.7356	−10.5
4	3	773.1014	20.1	20	19	816.3848	−24.1	31	30	845.9948	5.1
5	4	775.8056	−18.3	21	20	819.0856	−6.6	32	31	848.6740	−8.6
7	6	781.2217	−16.9	22	21	821.7826	−15.7	33	32	851.3542	10.6
8	7	783.9298	−14.8	23	22	824.4803	−3.0	34	33	854.0288	−4.0
9	8	786.6366	−22.8	24	23	827.1759	2.5	35	34	856.7019	−9.8
10	9	789.3470	7.3	25	24	829.8680	−13.1	36	35	859.3729	−11.0
11	10	792.0531	−1.3	26	25	832.5616	3.5	37	36	862.0424	−0.6
12	11	794.7609	10.1	27	26	835.2509	−7.2	38	37	864.7102	18.6
13	12	797.4656	−2.4	28	27	837.9389	−12.2	39	38	867.3696	−17.6
18	17	810.9855	−1.5	29	28	840.6274	6.0	40	39	870.0339	24.2
19	18	813.6864	−6.0								
						(001)					
1	2	1858.7301	−3.6	22	23	1797.5085	2.8	43	44	1729.0952	−8.7
2	3	1855.9863	−16.3	23	24	1794.4087	4.1	44	45	1725.6706	0.0
3	4	1853.2283	6.6	24	25	1791.2945	24.6	45	46	1722.2299	−4.3
4	5	1850.4502	4.8	25	26	1788.1600	3.8	46	47	1718.7756	−0.3
5	6	1847.6544	2.2	26	27	1785.0115	3.2	47	48	1715.3060	−3.0
6	7	1844.8412	−0.1	27	28	1781.8471	4.3	48	49	1711.8235	10.3
7	8	1842.0111	3.0	28	29	1778.6666	4.3	49	50	1708.3235	−8.4
8	9	1839.1636	6.9	29	30	1775.4701	1.9	50	51	1704.8161	41.0
9	10	1836.2978	0.7	30	31	1772.2567	−10.7	51	52	1701.2854	0.3
10	11	1833.4157	2.6	31	32	1769.0302	3.0	52	53	1697.7435	−10.5
11	12	1830.5163	3.9	32	33	1765.7869	5.5	53	54	1694.1919	22.3
12	13	1827.5994	1.5	33	34	1762.5277	3.6	54	55	1690.6196	−12.8
13	14	1824.6661	4.7	34	35	1759.2537	9.5	55	56	1687.0358	−23.0
14	15	1821.7156	6.2	35	36	1755.9621	−5.7	56	57	1683.4394	−22.1
15	16	1818.7474	−0.7	36	37	1752.6572	−1.3	57	58	1679.8314	1.6
16	17	1815.7635	3.5	37	38	1749.3365	−1.7	58	59	1676.2072	−0.9
17	18	1812.7625	3.9	39	40	1742.6488	−10.8	59	60	1672.5730	33.1
18	19	1809.7447	2.7	40	41	1739.2830	−7.6	60	61	1668.9176	−10.2
19	20	1806.7102	1.2	41	42	1735.9027	−0.6	63	64	1657.8871	20.8
20	21	1803.6596	3.4	42	43	1732.5065	−2.9	65	66	1650.4628	−3.5
21	22	1800.5895	−24.4								
1	0	1866.8494	−16.6	12	11	1895.2276	6.4	23	22	1921.3357	−5.7

H^{10}BO line positions, cont'd.

J'	J"	Obs.	O-C	J'	J"	Obs.	O-C	J'	J"	Obs.	O-C
2	1	1869.5196	−24.0	13	12	1897.6972	16.6	24	23	1923.5936	−8.8
3	2	1872.1767	18.0	14	13	1900.1462	8.5	25	24	1925.8325	−5.9
4	3	1874.8093	−3.1	15	14	1902.5773	10.5	26	25	1928.0506	−15.4
5	4	1877.4255	−7.2	16	15	1904.9881	−0.9	27	26	1930.2523	6.9
6	5	1880.0249	3.4	17	16	1907.3821	9.4	28	27	1932.4291	−21.5
7	6	1882.6043	−2.3	18	17	1909.7548	−2.4	30	29	1936.7315	1.7
8	7	1885.1656	−4.9	19	18	1912.1114	16.1	31	30	1938.8518	3.0
9	8	1887.7099	7.3	20	19	1914.4444	−10.1	32	31	1940.9511	−6.6
10	9	1890.2348	10.2								

(01^{1}1) *e-e*

J'	J"	Obs.	O-C	J'	J"	Obs.	O-C	J'	J"	Obs.	O-C
2	3	1860.5873	−8.5	21	22	1805.0926	−1.4	41	42	1740.1479	0.5
3	4	1857.8273	10.6	23	24	1798.8872	−30.8	43	44	1733.3089	13.5
4	5	1855.0461	−2.5	24	25	1795.7635	−5.5	44	45	1729.8646	−1.3
5	6	1852.2493	9.1	25	26	1792.6206	−7.2	45	46	1726.4087	18.0
6	7	1849.4319	−6.6	26	27	1789.4627	5.9	46	47	1722.9368	27.1
7	8	1846.5987	−1.8	27	28	1786.2857	−7.6	47	48	1719.4433	−30.4
8	9	1843.7460	−14.0	28	29	1783.0947	1.9	48	49	1715.9441	1.5
9	10	1840.8775	−7.2	29	30	1779.8867	4.1	49	50	1712.4255	−12.6
10	11	1837.9935	21.0	30	31	1776.6624	4.3	50	51	1708.8949	−0.6
11	12	1835.0871	0.3	31	32	1773.4230	15.6	51	52	1705.3484	−1.1
12	13	1832.1645	−6.7	32	33	1770.1650	0.4	52	53	1701.7882	4.5
13	14	1829.2259	0.0	33	34	1766.8933	7.8	53	54	1698.2107	−18.2
14	15	1826.2689	−2.4	34	35	1763.6045	3.2	54	55	1694.6191	−38.8
15	16	1823.2950	−2.1	35	36	1760.3012	11.8	55	56	1691.0180	−12.0
16	17	1820.3075	34.4	36	37	1756.9808	6.4	56	57	1687.3999	−13.7
17	18	1817.2955	−2.6	37	38	1753.6453	5.9	57	58	1683.7663	−30.3
18	19	1814.2702	−2.3	38	39	1750.2941	4.6	64	65	1657.9587	4.1
19	20	1811.2282	1.5	39	40	1746.9251	−19.8	65	66	1654.2202	35.0
20	21	1808.1692	4.1	40	41	1743.5461	9.8	66	67	1650.4628	10.8

J'	J"	Obs.	O-C	J'	J"	Obs.	O-C	J'	J"	Obs.	O-C
3	2	1876.7740	−21.3	12	11	1899.8012	−3.7	22	21	1923.5626	−13.8
4	3	1879.4059	−36.6	14	13	1904.7088	−5.6	23	22	1925.8325	2.2
5	4	1882.0257	13.1	15	14	1907.1335	−9.5	24	23	1928.0847	39.4
7	6	1887.1966	−14.6	16	15	1909.5404	3.4	26	25	1932.5170	−8.2
8	7	1889.7552	−14.6	18	17	1914.2923	−7.3	27	26	1934.7115	52.0
9	8	1892.2963	−1.0	19	18	1916.6414	11.2	28	27	1936.8755	8.2
10	9	1894.8193	21.6	20	19	1918.9655	−23.9	29	28	1939.0239	11.0
11	10	1897.3210	20.4								

(01^{1}1) *f-f*

J'	J"	Obs.	O-C	J'	J"	Obs.	O-C	J'	J"	Obs.	O-C
1	2	1863.3044	−22.4	20	21	1808.0090	6.6	39	40	1746.8465	−29.4
2	3	1860.5498	−13.3	21	22	1804.9311	4.6	40	41	1743.4795	3.6
3	4	1857.7774	−5.2	22	23	1801.8381	12.5	42	43	1736.6940	−10.9
4	5	1854.9880	8.0	23	24	1798.7279	9.7	44	45	1729.8529	−7.7
5	6	1852.1791	1.8	24	25	1795.6023	13.6	45	46	1726.4087	−30.7
6	7	1849.3521	−11.9	25	26	1792.4599	7.5	46	47	1722.9571	13.2
7	8	1846.5100	−3.2	26	27	1789.3033	18.8	47	48	1719.4839	−19.4
8	9	1843.6499	−2.0	27	28	1786.1290	10.5	48	49	1716.0007	−13.2
9	10	1840.7728	1.1	28	29	1782.9406	17.0	49	50	1712.5047	3.1
10	11	1837.8762	−18.7	29	30	1779.7352	10.7	50	51	1708.9892	−40.0
11	12	1834.9659	−6.1	30	31	1776.5157	17.2	52	53	1701.9289	−12.1

H^{10}BO line positions, cont'd.

J'	J"	Obs.	O-C	J'	J"	Obs.	O-C	J'	J"	Obs.	O-C
12	13	1832.0381	0.8	31	32	1773.2799	15.3	54	55	1694.8123	−12.9
13	14	1829.0897	−28.6	32	33	1770.0262	−12.6	55	56	1691.2383	27.3
14	15	1826.1300	− 3.5	33	34	1766.7616	2.6	56	57	1687.6444	0.3
15	16	1823.1522	8.8	34	35	1763.4808	8.3	57	58	1684.0407	4.4
16	17	1820.1566	8.9	35	36	1760.1857	20.8	58	59	1680.4258	25.4
17	18	1817.1459	23.1	36	37	1756.8741	18.2	61	62	1669.4943	−17.8
18	19	1814.1155	6.7	37	38	1753.5469	8.1	66	67	1651.0378	15.0
19	20	1811.0706	8.8								
3	2	1876.8148	−28.1	11	10	1897.4913	−16.9	24	23	1928.5384	−19.2
4	3	1879.4688	29.7	12	11	1899.9944	− 0.7	25	24	1930.7955	8.6
5	4	1882.0956	− 5.1	14	13	1904.9398	−16.6	26	25	1933.0281	−14.3
6	5	1884.7081	0.6	16	15	1909.8124	− 9.1	27	26	1935.2479	30.1
7	6	1887.3013	− 4.9	17	16	1912.2214	3.9	28	27	1937.4422	14.0
8	7	1889.8779	6.2	18	17	1914.6075	−21.6	29	28	1939.6191	20.4
9	8	1892.4350	7.3	22	21	1923.9705	−31.2	30	29	1941.7724	−12.8
10	9	1894.9738	9.2								

Appendix C

D^{11}BO Line Positions

Table C.1: Rotational-vibrational line positions included in the global fit of D^{11}BO data. The O-C denotes observed-calculated. All units in cm^{-1}.

J'	J''	Obs.	O-C	J'	J''	Obs.	O-C	J'	J''	Obs.	O-C
						(100)—(000)					
0	1	2251.4260	7.0	18	19	2209.6988	6.0	36	37	2161.7910	−4.0
1	2	2249.3020	−8.0	19	20	2207.1835	−1.0	37	38	2158.9738	−1.0
2	3	2247.1561	7.0	20	21	2204.6509	3.0	38	39	2156.1398	−7.0
3	4	2244.9814	−21.0	21	22	2202.1005	10.0	39	40	2153.2910	−4.0
4	5	2242.7884	11.0	22	23	2199.5308	1.0	40	41	2150.4267	1.0
5	6	2240.5676	6.0	23	24	2196.9440	−2.0	41	42	2147.5456	−6.0
6	7	2238.3227	−2.0	24	25	2194.3405	2.0	42	43	2144.6498	−5.0
7	8	2236.0559	2.0	25	26	2191.7197	4.0	43	44	2141.7423	35.0
8	9	2233.7652	−3.0	26	27	2189.0816	5.0	44	45	2138.8125	6.0
9	10	2231.4538	9.0	27	28	2186.4257	−4.0	45	46	2135.8695	−1.0
10	11	2229.1180	−1.0	28	29	2183.7546	2.0	46	47	2132.9096	−22.0
11	12	2226.7618	−1.0	29	30	2181.0656	−4.0	47	48	2129.9385	−3.0
12	13	2224.3838	−7.0	30	31	2178.3600	−12.0	48	49	2126.9502	−4.0
13	14	2221.9871	8.0	31	32	2175.6405	5.0	49	50	2123.9486	15.0
14	15	2219.5679	1.0	32	33	2172.9014	−11.0	50	51	2120.9277	−8.0
15	16	2217.1293	−1.0	33	34	2170.1466	−22.0	51	52	2117.8950	3.0
16	17	2214.6718	4.0	34	35	2167.3810	20.0	52	53	2114.8457	−1.0
17	18	2212.1942	−1.0	35	36	2164.5930	−2.0				
1	0	2255.5923	−35.0	20	19	2290.5379	5.0	37	36	2315.5782	1.0
3	2	2259.6635	−32.0	21	20	2292.1609	−27.0	38	37	2316.8799	−10.0
5	4	2263.6406	14.0	22	21	2293.7703	1.0	39	38	2318.1653	5.0
6	5	2265.5896	5.0	23	22	2295.3590	17.0	40	39	2319.4288	−10.0
7	6	2267.5151	−1.0	24	23	2296.9251	−1.0	41	40	2320.6768	9.0
8	7	2269.4178	2.0	25	24	2298.4747	10.0	42	41	2321.9037	6.0
9	8	2271.2966	−5.0	26	25	2300.0032	0.0	43	42	2323.1114	0.0
10	9	2273.1536	0.0	27	26	2301.5140	4.0	44	43	2324.3006	0.0
11	10	2274.9882	5.0	28	27	2303.0051	1.0	45	44	2325.4699	−9.0
12	11	2276.7981	−16.0	29	28	2304.4774	−1.0	46	45	2326.6232	13.0
13	12	2278.5951	51.0	30	29	2305.9313	3.0	47	46	2327.7518	−22.0

D^{11}BO line positions, cont'd.

J'	J"	Obs.	O-C	J'	J"	Obs.	O-C	J'	J"	Obs.	O-C
14	13	2280.3598	10.0	31	30	2307.3653	− 4.0	48	47	2328.8681	12.0
15	14	2282.1069	4.0	32	31	2308.7818	3.0	49	48	2329.9598	−10.0
16	15	2283.8346	12.0	33	32	2310.1791	7.0	50	49	2331.0383	29.0
17	16	2285.5396	− 1.0	34	33	2311.5567	1.0	51	50	2332.0903	− 5.0
18	17	2287.2268	12.0	35	34	2312.9159	− 1.0	52	51	2333.1257	−12.0

$(01^{1}0)$—(000) e—e

J'	J"	Obs.	O-C	J'	J"	Obs.	O-C	J'	J"	Obs.	O-C
7	8	590.5831	53.2	16	17	571.8982	0.0	25	26	553.3963	5.2
8	9	588.4964	21.4	17	18	569.8359	26.7	27	28	549.3095	− 7.0
9	10	586.4143	16.6	18	19	567.7728	22.4	28	29	547.2653	−58.0
10	11	584.3256	−73.3	19	20	565.7103	3.1	30	31	543.2055	51.2
11	12	582.2550	− 3.0	20	21	563.6547	28.7	31	32	541.1668	−19.6
12	13	580.1775	−21.5	21	22	561.6006	46.8	32	33	539.1380	−18.1
13	14	578.1039	−22.5	23	24	557.4923	12.4	33	34	537.1114	−18.8
15	16	573.9630	−23.3	24	25	555.4389	−33.6				

J'	J"	Obs.	O-C	J'	J"	Obs.	O-C	J'	J"	Obs.	O-C
1	0	609.4166	59.5	13	12	634.7085	−13.6	27	26	664.3967	− 7.5
2	1	611.5065	−50.2	14	13	636.8248	− 8.6	29	28	668.6456	0.3
3	2	613.6079	−58.8	16	15	641.0593	− 9.0	30	29	670.7722	23.6
4	3	615.7093	−82.7	18	17	645.2996	16.2	31	30	672.8955	14.1
5	4	617.8257	29.0	19	18	647.4178	− 1.8	32	31	675.0198	15.3
6	5	619.9322	28.1	20	19	649.5372	−14.2	33	32	677.1442	18.8
7	6	622.0330	−42.4	21	20	651.6583	−16.9	34	33	679.2648	−14.7
8	7	624.1452	−12.7	22	21	653.7820	2.3	35	34	681.3935	35.4
9	8	626.2579	10.2	23	22	655.9033	− 8.3	36	35	683.5123	−10.7
10	9	628.3662	−22.4	24	23	658.0275	5.2	37	36	685.6364	0.5
11	10	630.4836	24.1	25	24	660.1493	− 8.4	38	37	687.7578	−11.7
12	11	632.5960	10.0	26	25	662.2760	23.0	39	38	689.8810	− 0.6

$(01^{1}0)$—(000) f—e

J'	J"	Obs.	O-C	J'	J"	Obs.	O-C	J'	J"	Obs.	O-C
1	1	607.3247	21.3	6	6	607.5497	31.5	11	11	608.0506	8.9
3	3	607.3791	0.5	8	8	607.7145	0.4	12	12	608.1845	7.5
5	5	607.4746	-48.1	10	10	607.9308	39.9	15	15	608.6505	-15.4

(001)—(000)

J'	J"	Obs.	O-C	J'	J"	Obs.	O-C	J'	J"	Obs.	O-C
2	1	1658.7849	−10.0	19	18	1693.3223	6.0	35	34	1723.1055	9.0
3	2	1660.8702	−15.0	20	19	1695.2722	− 1.0	36	35	1724.8610	17.0
4	3	1662.9490	−36.0	21	20	1697.2116	− 2.0	37	36	1726.5987	−24.0
5	4	1665.0305	21.0	22	21	1699.1389	−11.0	38	37	1728.3269	−28.0
6	5	1667.0999	12.0	23	22	1701.0573	6.0	40	39	1731.7484	9.0
8	7	1671.2212	2.0	24	23	1702.9619	1.0	42	41	1735.1145	21.0
9	8	1673.2721	− 1.0	25	24	1704.8546	− 3.0	43	42	1736.7685	−64.0
10	9	1675.3156	− 7.0	26	25	1706.7360	1.0	44	43	1738.4248	5.0
11	10	1677.3531	4.0	27	26	1708.6053	4.0	46	45	1741.6814	−14.0
12	11	1679.3807	− 4.0	28	27	1710.4645	30.0	47	46	1743.2917	− 3.0
13	12	1681.4020	9.0	29	28	1712.3056	− 1.0	48	47	1744.8880	2.0
14	13	1683.4120	− 1.0	30	29	1714.1366	− 7.0	49	48	1746.4711	8.0
15	14	1685.4145	6.0	31	30	1715.9562	− 1.0	50	49	1748.0351	−41.0
16	15	1687.4048	−13.0	33	32	1719.5552	−10.0	51	50	1749.5967	19.0

D^{11}BO line positions, cont'd.

J'	J"	Obs.	O-C	J'	J"	Obs.	O-C	J'	J"	Obs.	O-C
17	16	1689.3868	−16.0	34	33	1721.3371	3.0	52	51	1751.1385	17.0
18	17	1691.3589	−14.0								
0	1	1645.5859	−31.0	16	17	1610.6303	− 1.0	31	32	1575.5763	− 2.0
1	2	1643.4812	3.0	17	18	1608.3603	− 1.0	32	33	1573.1655	7.0
2	3	1641.3618	− 5.0	18	19	1606.0811	4.0	33	34	1570.7442	1.0
3	4	1639.2363	30.0	19	20	1603.7913	1.0	34	35	1568.3136	− 6.0
4	5	1637.0939	− 1.0	20	21	1601.4924	3.0	35	36	1565.8755	1.0
6	7	1632.7824	−21.0	21	22	1599.1834	0.0	36	37	1563.4285	9.0
7	8	1630.6122	−22.0	22	23	1596.8644	− 6.0	37	38	1560.9713	3.0
8	9	1628.4342	1.0	23	24	1594.5366	− 6.0	39	40	1556.0312	2.0
9	10	1626.2438	1.0	24	25	1592.1997	− 1.0	40	41	1553.5480	2.0
10	11	1624.0434	2.0	25	26	1589.8533	2.0	41	42	1551.0556	− 3.0
11	12	1621.8327	2.0	26	27	1587.4970	1.0	42	43	1548.5558	4.0
12	13	1619.6119	− 1.0	27	28	1585.1309	− 5.0	43	44	1546.0455	− 6.0
13	14	1617.3817	2.0	28	29	1582.7565	0.0	44	45	1543.5288	5.0
14	15	1615.1410	1.0	29	30	1580.3726	2.0	45	46	1541.0013	− 5.0
15	16	1612.8904	− 2.0								

$(01^1 1)$—$(01^1 0)$ e—e

J'	J"	Obs.	O-C	J'	J"	Obs.	O-C	J'	J"	Obs.	O-C
2	1	1651.8518	13.0	21	20	1689.2471	− 3.0	39	38	1720.9042	− 2.0
3	2	1653.9188	22.0	22	21	1691.1058	13.0	40	39	1722.5506	− 4.0
4	3	1655.9730	10.0	23	22	1692.9505	2.0	41	40	1724.1859	2.0
5	4	1658.0160	− 6.0	24	23	1694.7838	− 8.0	42	41	1725.8076	− 6.0
6	5	1660.0508	2.0	25	24	1696.6073	− 2.0	43	42	1727.4195	9.0
7	6	1662.0737	− 2.0	26	25	1698.4187	− 2.0	44	43	1729.0173	3.0
8	7	1664.0864	1.0	27	26	1700.2186	− 2.0	45	44	1730.6033	2.0
9	8	1666.0875	− 4.0	28	27	1702.0081	10.0	46	45	1732.1758	−13.0
10	9	1668.0791	5.0	29	28	1703.7843	5.0	47	46	1733.7383	− 4.0
11	10	1670.0582	− 2.0	30	29	1705.5484	− 4.0	48	47	1735.2878	− 3.0
12	11	1672.0281	8.0	31	30	1707.3022	0.0	49	48	1736.8274	22.0
13	12	1673.9854	3.0	32	31	1709.0437	− 2.0	50	49	1738.3487	−12.0
14	13	1675.9322	3.0	33	32	1710.7737	− 1.0	52	51	1741.3632	9.0
15	14	1677.8675	− 2.0	34	33	1712.4913	− 5.0	53	52	1742.8508	10.0
16	15	1679.7926	3.0	35	34	1714.1980	− 2.0	54	53	1744.3239	− 9.0
17	16	1681.7059	1.0	36	35	1715.8923	− 4.0	56	55	1747.2360	−13.0
18	17	1683.6074	− 6.0	37	36	1717.5749	− 2.0	58	57	1750.1022	27.0
19	18	1685.4992	0.0	38	37	1719.2456	− 2.0	59	58	1751.5099	−18.0
20	19	1687.3782	− 8.0								
19	18	2288.8917	2.0								
1	2	1650.3966	−11.0	19	20	1611.5550	11.0	35	36	1574.6813	5.0
3	4	1646.1776	2.0	20	21	1609.3220	− 7.0	36	37	1572.2925	14.0
4	5	1644.0621	16.0	21	22	1607.0823	1.0	37	38	1569.8913	− 2.0
5	6	1641.9400	12.0	22	23	1604.8324	2.0	38	39	1567.4807	−11.0
6	7	1639.8123	3.0	23	24	1602.5706	−19.0	39	40	1565.0634	12.0
8	9	1635.5414	− 5.0	25	26	1598.0241	2.0	40	41	1562.6335	8.0
9	10	1633.3972	− 8.0	26	27	1595.7349	2.0	41	42	1560.1927	− 6.0
10	11	1631.2481	4.0	27	28	1593.4351	− 5.0	42	43	1557.7441	0.0
11	12	1629.0906	− 2.0	28	29	1591.1286	20.0	43	44	1555.2860	8.0
12	13	1626.9269	2.0	29	30	1588.8078	4.0	44	45	1552.8168	3.0
13	14	1624.7578	26.0	30	31	1586.4776	− 6.0	45	46	1550.3373	− 8.0

D^{11}BO line positions, cont'd.

J'	J"	Obs.	O-C	J'	J"	Obs.	O-C	J'	J"	Obs.	O-C
14	15	1622.5743	−16.0	31	32	1584.1324	−65.0	46	47	1547.8489	−12.0
15	16	1620.3862	−24.0	32	33	1581.7897	2.0	47	48	1545.3531	4.0
16	17	1618.1940	10.0	33	34	1579.4303	3.0	48	49	1542.8454	− 2.0
17	18	1615.9891	2.0								

(01^11)—(01^10) f—f

J'	J"	Obs.	O-C	J'	J"	Obs.	O-C	J'	J"	Obs.	O-C
1	2	1650.3734	11.0	18	19	1612.7854	− 8.0	33	34	1577.3019	− 2.0
2	3	1648.2437	12.0	19	20	1610.4862	0.0	34	35	1574.8646	13.0
4	5	1643.9526	7.0	20	21	1608.1777	10.0	35	36	1572.4152	− 7.0
5	6	1641.7909	− 2.0	21	22	1605.8577	2.0	36	37	1569.9589	− 6.0
6	7	1639.6195	− 6.0	22	23	1603.5297	7.0	37	38	1567.4931	−13.0
7	8	1637.4401	11.0	23	24	1601.1920	10.0	38	39	1565.0188	−17.0
8	9	1635.2479	3.0	24	25	1598.8438	2.0	39	40	1562.5365	−16.0
9	10	1633.0464	1.0	25	26	1596.4867	− 2.0	40	41	1560.0475	5.0
10	11	1630.8354	6.0	26	27	1594.1213	6.0	42	43	1555.0408	16.0
11	12	1628.6133	1.0	27	28	1591.7450	− 5.0	43	44	1552.5226	0.0
12	13	1626.3814	− 4.0	28	29	1589.3622	12.0	44	45	1549.9975	− 1.0
13	14	1624.1402	− 1.0	29	30	1586.9661	−12.0	45	46	1547.4642	− 1.0
15	16	1619.6282	2.0	30	31	1584.5631	−14.0	46	47	1544.9211	−15.0
16	17	1617.3574	3.0	31	32	1582.1538	12.0	47	48	1542.3751	25.0
17	18	1615.0789	24.0								

J'	J"	Obs.	O-C	J'	J"	Obs.	O-C	J'	J"	Obs.	O-C
3	2	1660.8702	62.0	20	19	1694.5198	18.0	37	36	1724.9094	− 1.0
4	3	1662.9285	−21.0	21	20	1696.4014	36.0	38	37	1726.5987	67.0
5	4	1664.9872	7.0	22	21	1698.2667	5.0	39	38	1728.2614	−10.0
6	5	1667.0304	−14.0	23	22	1700.1242	9.0	40	39	1729.9211	1.0
7	6	1669.0674	11.0	24	23	1701.9673	−17.0	41	40	1731.5655	−21.0
8	7	1671.0897	− 3.0	25	24	1703.8039	6.0	42	41	1733.2010	−11.0
9	8	1673.1027	− 1.0	26	25	1705.6246	−15.0	43	42	1734.8243	− 4.0
10	9	1675.1048	0.0	27	26	1707.4373	− 1.0	44	43	1736.4370	19.0
11	10	1677.0963	4.0	28	27	1709.2374	2.0	45	44	1738.0333	− 1.0
12	11	1679.0764	4.0	29	28	1711.0254	2.0	46	45	1739.6204	7.0
13	12	1681.0442	−10.0	30	29	1712.8015	− 3.0	47	46	1741.1929	− 8.0
14	13	1683.0036	3.0	31	30	1714.5618	−48.0	48	47	1742.7571	15.0
15	14	1684.9503	0.0	32	31	1716.3175	−24.0	49	48	1744.3065	14.0
16	15	1686.8855	− 7.0	33	32	1718.0621	7.0	51	50	1747.3706	31.0
17	16	1688.8092	−18.0	34	33	1719.7902	− 9.0	52	51	1748.8772	−30.0
18	17	1690.7243	− 2.0	35	34	1721.5103	12.0	53	52	1750.3792	−15.0
19	18	1692.6242	−27.0								

Appendix D

D^{10}BO Line Positions

Table D.1: (100)—(000) rotational-vibrational line positions for D^{10}BO. The O-C denotes observed-calculated. All units in cm^{-1}.

J'	J''	Obs.	O-C	J'	J''	Obs.	O-C	J'	J''	Obs.	O-C
						(100)—(000)					
0	1	2302.8800	−48.0	15	16	2268.7820	− 4.0	30	31	2231.4368	23.0
1	2	2300.7235	− 5.0	16	17	2266.3845	−10.0	31	32	2228.8492	−13.0
2	3	2298.5544	78.0	17	18	2263.9749	7.0	32	33	2226.2573	5.0
3	4	2296.3605	76.0	18	19	2261.5524	38.0	33	34	2223.6534	− 2.0
4	5	2294.1452	24.0	19	20	2259.1087	− 4.0	34	35	2221.0377	−38.0
5	6	2291.9149	−14.0	20	21	2256.6568	9.0	35	36	2218.4204	− 4.0
6	7	2289.6705	−32.0	21	22	2254.1915	22.0	36	37	2215.7939	20.0
7	8	2287.4140	−10.0	22	23	2251.7114	19.0	37	38	2213.1607	55.0
8	9	2285.1403	0.0	23	24	2249.2181	12.0	38	39	2210.5120	8.0
9	10	2282.8484	−13.0	24	25	2246.7115	− 2.0	39	40	2207.8692	90.0
10	11	2280.5396	−39.0	25	26	2244.1930	−12.0	40	41	2205.2060	34.0
11	12	2278.2205	−13.0	26	27	2241.6551	−97.0	41	42	2202.5375	−16.0
12	13	2275.8855	9.0	27	28	2239.1238	1.0	43	44	2197.2031	79.0
13	14	2273.5286	−36.0	28	29	2236.5709	− 5.0	44	45	2194.5275	116.0
14	15	2271.1673	26.0	29	30	2234.0138	56.0				
1	0	2307.1576	11.0	17	16	2338.9452	1.0	32	31	2365.1391	6.0
2	1	2309.2561	−114.0	18	17	2340.7937	− 4.0	33	32	2366.7749	−20.0
3	2	2311.3597	−21.0	19	18	2342.6287	11.0	34	33	2368.4029	− 4.0
4	3	2313.4386	− 8.0	20	19	2344.4455	− 1.0	35	34	2370.0174	− 7.0
5	4	2315.4989	−15.0	21	20	2346.2499	14.0	36	35	2371.6206	−12.0
6	5	2317.5456	10.0	22	21	2348.0346	−16.0	37	36	2373.2173	29.0
7	6	2319.5694	−29.0	23	22	2349.8082	−10.0	38	37	2374.8036	71.0
8	7	2321.5820	−13.0	24	23	2351.5680	3.0	40	39	2377.9410	109.0
9	8	2323.5784	7.0	25	24	2353.3117	0.0	41	40	2379.4898	75.0
10	9	2325.5544	−13.0	26	25	2355.0411	− 5.0	42	41	2381.0304	51.0
11	10	2327.5150	−21.0	27	26	2356.7551	−26.0	43	42	2382.5641	49.0
12	11	2329.4623	1.0	28	27	2358.4570	−30.0	44	43	2384.0945	98.0
13	12	2331.3919	9.0	29	28	2360.1490	0.0	45	44	2385.6086	69.0
14	13	2333.3028	− 7.0	30	29	2361.8222	−27.0	47	46	2388.6217	95.0

D^{10}BO line positions, cont'd.

J'	J"	Obs.	O-C	J'	J"	Obs.	O-C	J'	J"	Obs.	O-C
15	14	2335.2017	17.0	31	30	2363.4874	− 6.0	49	48	2391.6049	118.0
16	15	2337.0795	−10.0								